Determining the Impact Diminished *RBX1* Expression has on Chromosome Stability in Cancer

by

Manisha Bungsy

A Thesis submitted to the Faculty of Graduate Studies of
The University of Manitoba
in partial fulfilment of the requirements of the degree of

MASTER OF SCIENCE

Department of Biochemistry & Medical Genetics
University of Manitoba
Winnipeg

TABLE OF CONTENTS

ABSTRACT

Chromosome instability (CIN) is an aberrant phenotype observed in nearly all cancer types including colorectal cancer and potentially, high-grade serous ovarian cancer (HGSOC). CIN is defined as an increase in the rate at which whole chromosomes, or large parts thereof, are gained or lost. In many cancer types, CIN is associated with cellular transformation, highly aggressive tumors, multi-drug resistance and poor patient outcome. Despite these associations, the molecular mechanisms underlying CIN remain largely unknown. Genomic amplification of Cyclin E1 (*CCNE1*) induces CIN and is a pathogenic event in ~22% of HGSOCs. Cyclin E1 is a cell cycle regulatory protein whose levels are tightly controlled by the SCF complex, an E3 ubiquitin ligase. The SCF complex is comprised of RBX1, SKP1, CUL1 and an FBox protein, and targets proteins like Cyclin E1 for degradation by the 26S proteasome. Remarkably, >80% of HGSOCs exhibit heterozygous loss of *RBX1*, which encodes the catalytic component of the SCF complex. Since RBX1 is a core component of the SCF complex, I hypothesise that its reduced expression is predicted to impair SCF complex function which may lead to the accumulation of oncogenic proteins like Cyclin E1. This suggests that aberrant turnover of oncoproteins such as Cyclin E1 may constitute an alternative pathway for inducing CIN and tumorigenesis. This study employs both transient (siRNA) and stable (CRISPR-Cas9) approaches to determine the impact of reduced *RBX1* expression on CIN and Cyclin E1 levels. Through the CRISPR-Cas9 approach, this study specifically seeks to model early disease development by assessing the potential impact heterozygous loss of *RBX1* may have on Cyclin E1 levels, CIN and cellular transformation in fallopian tube (FT) secretory epithelial cells, a cell of origin for HGSOC. Data gleaned from this study identify *RBX1* as a novel CIN gene, which suggests that reduced *RBX1* expression may contribute to early pathogenic events driving HGSOC development and progression.

ACKNOWLEDGEMENTS

I appreciate the many individuals and organizations who contributed to this research and my graduate experience. Foremost, I would sincerely like to thank my Thesis Supervisor, and Mentor, Dr Kirk McManus. For me, he has not only been the true scientist who asks the right questions and compels me to think critically but also the considerate individual who truly cares for his students and treats all the members of his lab like family. Kirk inspired me to work hard and I am extremely grateful for having received the opportunity to work under his guidance, for his continuous advice, support, encouragement, patience and for believing in my potential.

Next, I would like to thank my Advisory Committee Members, Dr. Mark Nachtigal and Dr. Yvonne Myal for their guidance and motivation. Mark's insights and contribution to my project and overall path as a graduate student have been remarkable, while Yvonne has provided excellent suggestions and has been an inspiring figure for me.

I would like to thank all the past and present members of the lab; Zelda Lichtensztejn, Laura Thompson, Lucile Jeusset, Michaela Palmer, Chloe Lepage, Claire Morden, Nicole Wilson, Mirka Sliwowski, Dr. Raghavendra, Kailee Rutherford, Morgan Hiebert and Ally Farrell. I am extremely grateful for having been part of a lab filled with such diverse, kind and passionate individuals who make the work environment pleasant and conducive to cooperation and growth. You have been a wonderful team to work with, I will always remember your kind actions, words of encouragement whenever I felt low, delicious treats and baked goodies on a regular basis which made me happy instantly (and gain weight!). Collectively, you made me feel at home and been a "surrogate" family to me. Zelda's support has been instrumental to my training in the lab. Our lab is lifeless without you, thank you for all the treats, advice in my challenging situations and overall, for being our lab "mom". Words fall short in thanking you for all your contributions to the lab and myself. Special thanks to Laura, who always went the extra mile to help me from the very beginning, motivated and inspired me throughout my time in the lab. I am also thankful for the BMG Peer Mentorship group, which has been beneficial during my journey. Thanks to Lisa Liang, my first mentor at the BMG Department. I would also like to thank the SafeWalk program at the University for dropping me home safely whenever I requested; and the Mental Health Support Team at the University of Manitoba which helped me cope with the many stresses.

I would equally like to extend my deepest gratitude to everyone who shared my life outside work: Kiran, Arshita, Vikram, little Amogh, Niketa, Kanika- who despite being thousands of miles

away in Australia has been of tremendous support. I am immensely grateful to my mom, and brother, for their unconditional support, my dad for always inspiring me, believing in me and providing emotional, financial and moral support. I shall be eternally thankful for having Clint in my life who rekindled hope, brought so much happiness, light and renewed dreams. During this time, I learnt that it is the darkest phases that help us focus better on the light within, no matter how dim it might appear at times. Overall, I am thankful for all the ones I have worked or shared life with (in Winnipeg or long distance), for they have directly or indirectly helped me meet my challenges along the way, and moulded my personality to become the more resilient person I am today.

I am very grateful for all the funding received that made this research possible. This study was conducted with the financial support from the Department of Biochemistry and Medical Genetics Studentship, operating grants from the Natural Sciences and Engineering Research Council (NSERC), CancerCare Manitoba, the Graduate Enhancement of Tri-Council Stipends (GETS) program (University of Manitoba), and Research Completion Scholarship and the International Graduate Student Entrance Scholarship (IGSES) awarded by the Faculty of Graduate Studies (University of Manitoba).

LIST OF TABLES

LIST OF FIGURES

LIST OF ABBREVIATIONS

%	percentage
~	approximately
<	less than
>	greater than
±	plus or minus
°C	degrees Celsius
µL	microliter(s)
µm	micrometer(s)
µM	micromolar
ρmol	picomolar
β-HCG	beta-human chorionic gonadotropin
2D	two-dimensional
3D	three-dimensional
5-FU	5-fluorouracil
AFP	alpha-fetoprotein
APC	Adenomatous Polyposis Coli
APC	Anaphase Promoting Complex (Cyclosome)
ATM	Ataxia Telangiectasia-mutated
ATR	Ataxia Telangiectasia and Rad3-related
AURKA	Aurora Kinase A
BCA	Bicinchoninic Acid
bp	base pair(s)
BFP	Blue Fluorescent Protein
BRCA1/2	Breast Cancer 1/2
BSA	bovine serum albumin
CA125	Cancer Antigen 125
Cas9	CRISPR-associated Protein 9
CCD	charge-coupled device
CCNE1	Cyclin E1 gene
CDC6	Cell Division Cycle 6
CENPA	Centromeric Protein A
CIMP	CpG island methylator phenotype
CIN	chromosome instability
cm	centimeter
CO_2	carbon dioxide
COPS8	COP9 Signalosome Subunit 8
CPTS	copper phthalocyanine 3,4’,4’’,4’’’-tetrasulfonic acid tetrasodium salt
CRC	colorectal cancer
CRISPR	clustered regularly interspaced short palindromic repeat
CT	computerized tomography
C-terminal	carboxy-terminal
CUL1	Cullin 1
CUL3	Cullin 3
CUL4A	Cullin 4A

DDB1	Damage Specific DNA Binding Protein 1
DDB2	Damage Specific DNA Binding Protein 2
DAPI	4’,6-diamidino-2-phenylindole
DMEM	Dulbecco’s modified Eagle medium
DNA	deoxyribonucleic acid
DSB(s)	double strand break(s)
E1	E1 ubiquitin-activating enzyme
E2	E2 ubiquitin-conjugating enzyme
E3	E3 ubiquitin-protein ligase
ECL	enhanced chemiluminescence
EDTA	ethylenediaminetetraacetic acid
EMI1	Early Mitotic Inhibitor 1
FAP	familial adenomatous polyposis
FBS	fetal bovine serum
FIGO	International Federation of Gynecology and Obstetrics
FOLFIRI	folinic acid, 5-fluorouracil and irinotecan
FOLFOX	folinic acid, 5-fluorouracil and oxaliplatin
FT	fallopian tube
FTSECs	fallopian tube secretory epithelial cells
GFP	green fluorescent protein
h	hour(s)
HBSS	Hank’s balanced salt solution
HGSOC	High-Grade Serous Ovarian Cancer
HNPCC	hereditary nonpolyposis colorectal cancer
HRP	horseradish peroxidase
HRR	homologous recombination repair
IARC	International Agency for Research on Cancer
IHC	immunohistochemistry
Indels	insertions or deletions
ITH	intratumoral heterogeneity
KCl	potassium chloride
kDa	kilodalton(s)
KEAP1	Kelch Like ECH Associated Protein 1
KLHL8	Kelch Like Family Member 8
KS	Kolmogorov-Smirnov
LB	Luria-Bertani
min	minute(s)
mL	milliliter(s)
MLH1	MutL Homolog 1
mM	millimolar
MN	micronucleus
MNF	micronucleus formation
MRI	magnetic resonance imaging
mRNA	messenger RNA
MSH2	MutS Homolog 2
MSH6	MutS Homolog 6

MSI	microsatellite instability
MYC	MYC Proto-Oncogene, BHLH Transcription Factor
NA	nuclear area
ng	nanogram(s)
NER	nucleotide excision repair
NHEJ	non-homologous end-joining
nm	nanometer(s)
nM	nanomolar
NMD	Nonsense-mediated mRNA decay
NTgRNA	Non-targeting guide RNA
OSE	ovarian surface epithelial
P-value	Probability value
PALB2	partner and localiser of BRCA2
PAM	protospacer adjacent motif
PARP	poly(ADP-ribose) polymerase
PBS	phosphate buffered saline
PET	positron-emission tomography
PMS2	PMS1 Homolog 2, Mismatch Repair System Component
PVDF	polyvinylidene difluoride
RAD51	RAD51 Recombinase
RAS	Ras Proto-Oncogene, GTPase
RBX1	Ring-Box1
RING	Really Interesting New Gene
RIPA	radioimmunoprecipitation assay
RNA	ribonucleic acid
ROS	Reactive oxygen species
Rpm	revolutions per minute
RT	room temperature
RTCA	real-time cellular analysis
SCF	SKP1-CUL1-F-box Protein
SD	standard deviation
SDS	sodium dodecyl sulfate
SFM	serum-free media
shRNA	short hairpin ribonucleic acid
siRNA	short interfering ribonucleic acid
SKP1	S-phase Kinase Associated Protein 1
SKP2	S-Phase Kinase Associated Protein 2
SL	synthetic lethal
STICs	serous tubal intraepithelial carcinomas
TBS	tris buffered saline
TBST	tris buffered saline with tween-20
TCGA	The Cancer Genome Atlas
TGFBR2	Transforming Growth Factor Beta Receptor 2
TIFF	tagged image format
TNM	tumor size, lymph node involvement, and metastasis
TP53	Tumor Protein P53

tRNA	transfer ribonucleic acid
UICC	Union Internationale Contre le Cancer

CHAPTER 1: INTRODUCTION

Cancer is one of the leading causes of morbidity and mortality throughout the world[1]. The recent statistics by the International Agency for Research on Cancer (IARC) report the worldwide occurrence of 18.1 million new cancer cases and 9.6 million deaths in 2018[2,3]. In addition, IARC estimates that 1 in 5 men will develop cancer during their lifetime, whereas 1 in 6 women will develop the disease[2,3]. They also estimate that 1 in 8 men and 1 in 11 women will ultimately succumb to cancer. According to the IARC, cancer incidence is predicted to increase across the world, with the yearly number of new cancer patients diagnosed increasing from ~18.1 million in 2018 to ~29.4 in 2040[2,3]. This dramatic increase in cancer incidence reflects many factors including population growth and lifestyle changes that have led to a longer life expectancy, which in turn provides additional time for cancers to occur. Most importantly, ageing, which is considered as one of the most important risk factors for developing cancers, also contributes to the dramatic increase in cancer incidence. Cancer is already the first or second leading cause of death in individuals below the age of 70 in at least half of the countries in the world[2]. For example, cancer is the leading cause of death in Canada[4]. In addition, it is predicted that 50% of Canadians will develop cancer during their lifetime, and ~25% of Canadians will succumb to cancer[4]. According to current trends, more than 200,000 Canadians are expected to be newly diagnosed with cancer and more than 80,000 Canadians will die from cancer in 2019 alone[4]. Despite advances in research, the morbidity and mortality rates associated with cancer continue to rise every year, highlighting the urgent need for obtaining a better understanding of the underlying causes and mechanisms driving cancer development and progression. The main goal of my thesis is to elucidate some of the early events that are suspected to contribute to tumorigenesis, particularly in two cancer contexts, colorectal cancer (CRC) and high-grade serous ovarian cancer (HGSOC).

1.1. Overview of Colorectal Cancer (CRC)

According to the 2019 Canadian Cancer Society Statistics, CRC is predicted to be the third most commonly diagnosed cancer in Canada, accounting for approximately 12% of all new cancer cases[4]. The report also predicts about 26,300 new diagnoses of CRC in 2019[4]. In addition, males have a higher lifetime probability (1 in 14) of developing CRC as compared to females (1 in 18)[4]. CRC also accounts for ~12% of all cancer-related deaths, ranking second and third in men and women, respectively[4]. Also, the lifetime probability of dying from CRC is 1 in 32 for Canadian males and 1 in 37 for Canadian females. However, an overall decline in CRC has been observed since 2011, with males having a more rapid decline (-2.3%) relative to females (-1.7%). This reduced incidence rate in CRC can be attributed to many factors, including reduced modifiable risk factors (e.g. reduction in smoking), improved screening, early surgical removal of intestinal polyps and a better molecular understanding of the disease that led to improved treatment options. However, the decline is mostly limited to older adults because CRC incidence rates are increasing in younger generation below the age of 50 in Canada[4,5]. It is also important to note that despite effective screening modalities, ~50% of individuals with early stage (I or II) disease ultimately develop metastatic disease[6]. Also, ~50% of all CRC patients are diagnosed at advanced stages (III or IV)[7], of which ~20% already present with metastatic disease[8]. Unfortunately, individuals with metastatic disease have very poor survival outcomes, with less than 15% surviving 5 years or more, relative to individuals with stage I or II disease, whose 5 year survival rates are 70-90%[9,10]. Therefore, it is imperative to understand the underlying mechanisms leading to the pathogenesis and progression of CRC in order to improve treatment options and minimise the morbidity and mortality rates associated with the disease.

1.1.1. Pathogenesis, Diagnosis, Staging and Current Treatments of CRC

The sites of origin of primary CRCs include the colon and rectum. Based on the precise location within the colon, CRCs can be further categorized into proximal (forming within the cecum, ascending colon, transverse colon and splenic fixture), distal (originating from the descending and sigmoid colon) and rectal (arising from the rectosigmoid junction or rectum)[11]. In addition, the proximal segment differs considerably from the distal segment in terms of embryological origins, differential exposure to the microbiome, physical and functional features. Therefore, it is not surprising to find that tumors from these different locations of the colon often harbour distinct genetic and epigenetic differences, reflecting the unique molecular features underlying their etiology[12,13]. Most CRCs are adenocarcinomas[14] and the stepwise pathway from low- and high-grade dysplasia to metaplasia and ultimately invasive carcinoma is arguably best understood in CRC[15]. Also, the progression from a precursor lesion to complex, heterogeneous malignant carcinoma is estimated to occur over at least 10 years through diverse aberrant molecular mechanisms[14].

The main techniques employed in the diagnosis of CRC are flexible sigmoidoscopy and colonoscopy, with the latter being considered as the typical diagnostic tool for identifying and removing pre-cancerous lesions and/or polyps in CRC[16]. At the time of diagnosis, staging is done to implement the most suitable prognostic and therapeutic measures. The TNM (Tumor, Node, Metastasis) staging system provides information about the size of the tumor, the number of lymph nodes involved and the extent of metastasis[17]. Once these criteria are evaluated, a Union Internationale Contre le Cancer (UICC) stage (Stages 0 – IV) CRC is determined [17,18]. Stage 0 CRC (carcinoma *in situ*) refers to the cancer being limited to the innermost lining of the colon or rectum; stage I CRC refers to a cancer that has invaded into the submucosa of the colon or rectum;

stage II CRC occurs when the cancer has grown further into serosa without any lymph node involvement nor metastasis. Stage III CRC involves nearby lymph nodes but no metastasis, whereas stage IV cancers involve spread to distant organs like the lungs or liver[18].

CRC treatment options are typically tailored to the stage of the disease. In general, early stage CRC patients (stages 0-II) undergo surgical resection of the primary tumor, along with a marginal section of tissue adjacent to the tumor. Stages II – IV CRC patients are generally treated with surgery, followed by adjuvant chemotherapy[19,20]. The standard chemotherapy currently employed for CRC includes combinatorial regimens, such as FOLFOX (Folinic acid, 5-Fluorouracil and Oxaliplatin) or FOLFIRI (Folinic acid, 5-Fluorouracil and Irinotecan)[20,21]. Folinic acid enhances the anti-tumorigenic properties of 5-Fluorouracil[22], a pyrimidine analog employed to interfere with DNA replication and transcription[23]. Oxaliplatin is a platinum-containing compound that causes single-strand and double-strand breaks by cross-linking DNA[24] and Irinotecan is a topoisomerase inhibitor that induces DNA damage and inhibits transcription[25]. Unfortunately, these chemotherapeutics not only affect the highly proliferative cancer cells, but also impact normally dividing cells, which can lead to unwanted side-effects including hair loss, diarrhea and nausea. Therefore, a better understanding of the underlying aberrant pathways driving cancer progression is essential to develop more effective and personalized treatment options. Additionally, the emergence of drug resistance following extensive chemotherapeutic regimens is an overall concern that frequently occurs in patients with metastatic CRC that can ultimately induce more aggressive disease[26-28]. Thus, elucidating the molecular pathways underlying chemoresistance may enable us to develop new therapies to better combat drug-resistant, aggressive forms of CRC.

1.1.2. The Molecular Pathology of CRC

CRC is considered a highly heterogeneous disease that arises from a precursor lesion or polyp, which has the potential of transforming into a malignant tumor through a variety of aberrant molecular mechanisms[14]. Disease heterogeneity can be exacerbated by various factors contributing to the etiology and pathogenesis, such as the anatomic location of the tumor (proximal or transverse), genetic inheritance and epigenetic factors. Genetic predisposition to CRC accounts for ~15% of cases including Lynch Syndrome (hereditary non-polyposis colon cancer [HNPCC]) and familial adenomatous polyposis (FAP)[29,30]. On the other hand, sporadic or *de novo* CRCs account for ~85% of all CRC cases. *De novo* CRCs generally develop from the accrual of genetic aberrations that impair genome stability and include activation of proto-oncogenes to oncogenes (e.g. *KRAS*), inactivation of tumor suppressor genes (e.g. *TP53* and *APC*) and defects in DNA repair genes (e.g. *MLH1*).

Loss of genome stability (genome instability) is considered a pathogenic event that occurs virtually in all cancer types, but is arguably best understood in CRC context[31-34]. In general, genome instability can be subdivided into three main categories: 1) CpG island methylator phenotype (CIMP), which involves epigenetic gene silencing induced through DNA hyper-methylation of CpG islands within gene promoters including DNA repair and tumor suppressor genes[35,36]; 2) microsatellite instability (MSI), which arises from defects in DNA mismatch repair genes (*MLH1*, *MSH2*, *MSH6* and *PMS2*) and results in the accumulation of background mutations especially within microsatellite DNA (highly repetitive DNA sequences consisting of 1-6 base pairs)[37,38]; and, 3) chromosome instability (CIN), which is defined as an increase in the rate at which whole chromosomes, or large parts thereof, are gained or lost [30,39,40]. CIN (detailed in

Section 1.4, Page 15) is the primary focus of this thesis as it is the predominant type of genome instability impacting virtually all cancers, including CRCs[40-43].

1.2. Overview of High-Grade Serous Ovarian Cancer (HGSOC)

Ovarian cancer is the 8th most common cancer affecting Canadian women and the 5th leading cause of death among women in Canada, accounting for 4.9% of all cancer-related deaths. One in every 75 women has a lifetime probability of developing ovarian cancer[4]. Recent Canadian Cancer Society Statistics estimate that ~3,000 cases of ovarian cancer will be diagnosed in 2019[4]. Amongst the different subtypes of ovarian cancer, High-Grade Serous Ovarian Cancer (HGSOC) is the most prevalent, accounting for ~70% of all ovarian cancer cases with ~2,100 new cases estimated to be diagnosed in 2019 in Canada. Unfortunately, HGSOC is the most lethal gynecological cancer in Canadian women[4]. Despite advancements in research, there is still a lack of screening modalities and consequently, most women are diagnosed at late stages (III or IV) when treatment options are limited. Accordingly, the 5-year survival rates for HGSOC have remained dismal over many decades, with a rate of 39% and 17% for stage III and IV, respectively[44]. Another major hurdle in treating HGSOC is chemoresistance. Most women (~85%) who are diagnosed at late stages have disease recurrence even after responding to first-line therapy[45]. Much of the underlying mechanisms driving chemoresistance in HGSOC remain unidentified. In addition, the molecular pathogenesis of HGSOC is also poorly understood. These factors highlight the urgent need to better understand the early pathogenic events driving HGSOC development, progression and multidrug resistance. Only after elucidating the pathways contributing to disease development, will it be possible to develop suitable therapeutic strategies that exploit those aberrant origins to improve the lives and outcomes of women living with

HGSOC. My thesis aims to gain an understanding of the potential molecular mechanisms driving early events leading to HGSOC by employing disease-relevant *in vitro* models to determine if and how they may impact disease development and progression.

1.2.1. Pathogenesis, Diagnosis, Staging and Current Treatments of HGSOC

For many decades, the true cell of origin for HGSOC was largely misunderstood and many investigators still debate the matter. However, over the last few years, advanced DNA sequencing studies have provided insight into the precursor cell for HGSOC. Earlier studies suggested that HGSOC could source from the transformation events in the ovarian surface epithelial cells (OSE) resulting in the formation of cortical inclusion cysts in the ovaries[46,47]. Most of the hypotheses that supported OSE cells as the predominant cell of origin for HGSOC stemmed from the "incessant menstruation" theory proposed by Fathalla *et al.*, wherein the number of lifetime ovulations was suggested as a major risk factor for ovarian cancer[48]. Briefly, the cyclic exposure of the ovarian surface to increased inflammatory factors, followed by the repair of the lining post- menstruation, subject the OSE cells to high levels of genotoxic stresses[49,50]. Other studies that further support the OSE as the site of origin evinced from superovulation experiments in mice, which resulted in increased DNA damage and release of inflammatory immune mediators[51]. Additional evidence gleaned from hyper ovulating hens developing ovarian cancer that strengthened the link between inflammation and neoplastic transformation in OSE cells[52]. However, no definitive conclusion for the precise source of HGSOC could be derived from the above studies. Moreover, the presence of a precursor lesion in the ovary leading to HGSOC has not been decisively shown[53,54], nor do the majority of HGSOCs recapitulate the morphological features of the OSE[53,55]. In fact, recent molecular phenotyping studies have generated substantial evidence mapping the source of most HGSOC cases (at least 60%)[56] to the fallopian tube and not to the ovaries, and typically from the

fimbrial region of the distal segment[57-60]. Many of these studies show that precursor lesions, called serous tubal intraepithelial carcinomas (STICs) are derived from the fallopian tube secretory epithelial cells (FTSECs). It is estimated that it takes ~7 years for STICs to mature and implant into the ovary, where they likely undergo a rapid transition into a malignant tumor[60]. This observation resulted in a paradigm shift that radically improved our understanding of the etiological origin of HGSOCs and prompted researchers to re-evaluate previous research models and generate novel models that better reproduce the biology associated with early disease origins, to dramatically improve our fundamental understanding of the aberrant events contributing to HGSOC pathogenesis.

One of the principle factors responsible for the high mortality rate associated with HGSOC is the lack of effective screening tests for early diagnosis, when the tumor is confined to a localised region[61]. As a result, only a small minority of HGSOC cases (~13%) are diagnosed at stage I or II, while the majority are diagnosed in stage III or IV, when the disease has already begun to spread[62]. As expected, HGSOC patients diagnosed at early stages have a better prognosis and a 10-year survival rate of 55%[62-65]; however, patients with advanced stage disease have a 10-year survival chance of only 15%[62]. Another factor that further delays the detection of HGSOC is the late onset of symptoms or non-specificity of symptoms associated with a localised disease that includes frequent abdominal distension or bloating, weight loss, reduced appetite, early satiety, fatigue, pelvic/abdominal pain, increased urinary urgency or frequency or urgency[61,66,67]. As the disease progresses, symptoms may be accompanied by the production of ascites (abdominal fluid) causing increased bloating and discomfort and respiratory symptoms (e.g. dyspnoea and cough) may also arise from the built-up intrabdominal pressure[68]. Over the past few decades, various studies and clinical trials have been undertaken to devise screening strategies that could detect

early-stage HGSOC. Initial investigations of HGSOC employ a multimodal approach involving the measurement of the serum cancer antigen (CA125), in combination with a complete physical examination of the patient (including breast, pelvic, rectovaginal examination), and radiographic imaging (transvaginal ultrasound and/or abdominal ultrasonography, CT, MRI and/or PET scans)[61]. In addition to CA125, women under the age of 40 are also tested for the levels of beta-human chorionic gonadotropin (β-HCG) and alpha-fetoprotein (AFP) to exclude the possibility of germ cell ovarian cancer. Results from radiographic imaging will aid in the staging by revealing details about size, location and vascularity of ovarian or pelvic masses[68]. However, to further establish the stage of the disease, laparotomy or laparoscopic surgery is performed where the tumor mass along with any lymph nodes and ascitic fluid present are removed.

The 2014 International Federation of Gynecology and Obstetrics (FIGO) staging system is currently employed to determine the stage of the disease based on the extent of dissemination at the time of diagnosis[69]. Moreover, the staging system was recently updated to take into account the Müllerian origin of the majority of ovarian cancers and grouping them into a single system for assessment[69]. Briefly, stage I refers to the disease that is still restricted to the fallopian tubes or ovaries. Stage II involves the spread of cancer to other pelvic organs such as the uterus. Stage III refers to the malignant spread past the pelvic region to tissues within the abdominal cavity and/or to the peritoneal lymph nodes. Stage IV involves distant metastatic spreads beyond the peritoneal cavity and with the involvement of inguinal and extra-abdominal lymph nodes. Stage IV patients also often present with obstructed bowel as a result of metastatic growth forming fibrous connections between loops of the colon. The bowel obstruction impairs digestion, resulting in extreme weight loss and muscle wasting, frequent infections and ultimately leads to death[70].

Treatment for HGSOC patients depends on the stage identified at the time of diagnosis. Since

most of the HGSOC patients are diagnosed in stage III or IV, with signs of metastasis[62], cytoreductive surgery or debulking is currently employed. In some cases, depending on the extent of spread, chemotherapy is given first to shrink the primary tumor, followed by surgery. This approach is applied in patients deemed fit for surgical intervention, based on their age and physical ability to endure surgery. Cytoreductive surgery for ovarian cancer is generally performed by gynecological oncologists, and is shown to improve treatment and survival outcomes[71,72]. Surgical debulking primarily aims to achieve complete removal of all metastasized masses within the peritoneum[61]; however, the surgical method employed may also depend on other factors, such as disease stage and patient preferences. For instance, advanced stage treatment commonly involves *en bloc* resection of the bulk cancerous tissues, with the complete removal of ovaries, uterus, oviducts, sigmoid colon, omentum and lining of the abdominal cavity along with resection of the affected surrounding lymph nodes (pelvic and para-aortic lymph nodes)[61,73]. Additionally, young women who wish to conceive and have limited disease dissemination may decide to undergo unilateral salpingo-oophorectomy of the implicated segments only, instead of bilateral oophorectomy. A surgical cytoreduction outcome is deemed successful when there is no sign of cancer (termed R0 resection). An optimal surgical cytoreduction is one which results in <1 cm of residual disease (R1), whereas a suboptimal is one with ≥1 cm of residual cancer (R2)[61]. The extent of success achieved with the cytoreduction surgery is an important indicator of patient prognosis and survival outcome[68]. For example, some complete resection surgery led to relapse-free long-term survival in patients when combined with adjuvant chemotherapy[68] and in general, complete resection results in the greatest survival outcome, followed by optimal and finally, suboptimal surgery[74-76].

After the debulking surgery, nearly all HGSOC patients undertake adjuvant platinum-based chemotherapy[61]. Currently, most combinatorial treatments consist of 6 to 9 cycles of carboplatin and paclitaxel[77]. Carboplatin is a platinum-containing agent which forms DNA adducts and interferes with DNA replication[78], whereas paclitaxel is a taxane-based drug that binds to microtubules and induces a mitotic cell-cycle arrest that ultimately leads to cell death[79]. The majority of HGSOC patients show sensitivity to first-line chemotherapy; however, >80% of women experience disease recurrence within 18 months, accompanied by drug resistance[45,77]. As a maintenance therapy for recurrent disease in HGSOC, second-line combinatorial chemotherapeutics are employed. These may include pegylated liposomal doxorubicin (Caelyx), poly (ADP-ribose) polymerase inhibitors (PARP) (particularly for patients with *BRCA* mutations) and anti-angiogenic drugs such as bevacizumab. Some clinical trials have reported an improved patient response and progression-free survival with the addition of bevacizumab to the regimen in advanced-stage patients with relapse[80,81]. However, a recently completed Phase III clinical trial reported that addition of bevacizumab did not improve overall survival, questioning its efficacy[82]. Overall, mortality rates associated with recurrent HGSOC have seen no decline[44], which highlights that there remains a large gap in understanding the pathogenic mechanisms driving disease development, progression and chemoresistance.

1.2.2. Molecular Pathology of HGSOC

One of the major breakthroughs in elucidating the underlying genetic alterations in HGSOC emerged from a project by The Cancer Genome Atlas (TCGA) network in 2011[83]. Through whole exome sequencing experiments, the group revealed the highly unstable genome inherent in HGSOC[83]. The most common molecular aberration identified was in *TP53*, which occurred in upwards of 96% of all patients[83]. Moreover, *TP53* is also somatically mutated in precursor lesions

(i.e. STICs), which suggests that *TP53* mutations may be one the earliest genetic alterations necessary for the initiation of HGSOC[83,84]. Among the different types of *TP53* alterations, the most commonly occurring ones (~70%) are missense mutations that result in a protein with a substituted amino acid[85]. Additional *TP53* alterations also induce the formation of truncated p53 protein and include splicing, nonsense and frameshift mutations, which occur at 5%, 8% and 12%, respectively[85].

Other frequently recurring mutations in over half of HGSOC patients include mutations in key genes such as *BRCA1*, *BRCA2* and other genes (e.g. *PTEN*, *ATM*, *ATR* and *RAD51C*) encoding proteins in the HRR pathways[83,86,87]. Germline mutations in *BRCA* genes confer a substantial risk of developing ovarian cancer, with mutant *BRCA1* carrying a higher risk (20-50%) than mutant *BRCA2* (10-20%)[88-91]. Important insights into the role of *BRCA* mutations in the pathogenesis of HGSOC initially stemmed from HGSOC precursor lesions identified in fallopian tubes removed from *BRCA* mutation carriers undergoing bilateral salpingo-oophorectomy for prophylactic reasons[88]. This discovery resulted in the development of a protocol for Sectioning and Extensively Examining the Fimbriated (SEE-FIM protocol) end of the fallopian tube[88]. Importantly, the SEE-FIM protocol has also revealed STIC lesions in sporadic cases of HGSOC[92]. Overall, the mutations in the genes encoding functions in the DNA repair pathways and the appearance of precursor lesions in the samples from prophylactic surgery implicate HRR pathway defects as a major contributor to HGSOC pathogenesis. Additional alterations suspected to drive HGSOC include amplifications of the gene loci of key oncoproteins such as MYC (*MYC*) and Cyclin E1 (*CCNE1*; detailed in Section 1.3 below), each occurring in at least 20% of HGSOC cases[83].

1.3. Genomic Amplification of Cyclin E1 Induces CIN and is a Driver of Oncogenesis

HGSOCs present with a great degree of cellular heterogeneity that stems from the highly unstable genome inherent within the disease[93]. A deficient HRR pathway partially contributes to the overall genomic instability and CIN in ~50% of HGSOC patients[83]; however, mechanisms underlying genomic instability in the remaining cases stay largely unknown. *CCNE1* is a well-established CIN gene and its amplification at the level of the genome is believed to be an early driver of oncogenesis in HGSOC[94,95]. Under normal conditions, Cyclin E1 functions as an important cell cycle regulatory protein that is required for the G1 to S phase transition[96]. It also regulates vital cellular processes including DNA replication and centrosome duplication[97]. Hence, dysregulated Cyclin E1 expression is predicted to adversely impact central processes such as centrosome duplication and DNA replication that are both essential for maintaining chromosome stability. Besides HGSOC, genomic amplification of *CCNE1* is proposed to contribute to many additional cancers, including breast cancer, liver cancer and non-small cell lung cancer[98-103]. Importantly, genomic amplification of *CCNE1* is also associated with primary chemoresistance and overall poor survival in HGSOC[103,104]. In addition, as *CCNE1* amplifications are mutually exclusive from *BRCA* mutations, they are unlikely to be treated with PARP inhibitors, which effectively limits treatment options for *CCNE1* amplified HGSOC tumors. Therefore, it is important to identify drug targets that can therapeutically exploit HGSOCs harboring *CCNE1* amplifications[104,105]. Furthermore, independent of the genomic upregulation, there are other less intuitive pathways that may additionally result in elevated levels of CIN-associated proteins/oncoproteins like Cyclin E1 and contribute to disease development, progression and chemoresistance. Thus, identifying the molecular mechanisms underlying CIN will potentially enable us to better understand and address the current challenges in HGSOC.

1.4. Chromosome Instability (CIN)

As indicated above, CIN is defined as an increase in the rate at which whole chromosomes, or large parts thereof are gained or lost, and as a result, is synonymous with cell-to-cell heterogeneity[30,39,40]. Theoretically, numerical CIN induces aneuploidy and manifests as copy number changes for contiguous gene sets. On the other hand, structural CIN involves aberrations such as deletions, amplifications, inversions and transclocations[106,107], which may vary in size and impact specific genes to entire chromosomal arm(s). CIN, including numerical and/or structural, arises from errors in multiple cellular pathways such as kinetochore-microtubule attachment[108,109], centrosome duplication[98,110-112], mitotic spindle assembly[43], sister chromatid cohesion[113], cytokinesis[114] and DNA damage repair[115,116]. CIN is believed to occur early in tumorigenesis, where it influences the frequency at which genes implicated in oncogenic processes (proto-oncogenes, tumor suppressors, DNA repair, metastasis, drug resistance, apoptosis) are gained, lost, or mutated[117,118-120]. Accordingly, CIN influences oncogenic pathways leading to cellular transformation, tumor evolution and metastasis[120].

Beyond oncogenesis, cancers exhibiting extensive CIN present with a high degree of intratumoral heterogeneity (ITH)[121], suggesting that CIN drives the emergence of ITH. Conceptually, ITH results in increased clonal diversity within a tumor, and as a result of CIN, the diversity can further exacerbate over time, as the fittest clones with the greatest survival advantages persist, whilst those with detrimental survival characteristics (i.e. lethal) are lost from the population. Intuitively, increased heterogeneity in a population of cells would confer a genetic advantage by allowing a subset of cells to more rapidly adapt and respond to specific selection pressures important for metastasis and chemoresistance. In the context of HGSOC, ascites, which are produced in ~33% of the patients at diagnosis, commonly contain metastatic multicellular

aggregates that make up a complex, oncogenesis-prone environment[122]. Several studies have shown that tumor cells tend to detach as a group rather than single cells and that detachment of cellular aggregates provides better survival benefits for growth, metastasis and adaptation in a new microenvironment[122,123]. Penner-Goeke *et al.*[93] showed that cells isolated from serial samples of ascites exhibit CIN, suggesting that CIN could be a source of cellular heterogeneity within ascites. Moreover, the multicellular aggregates in ascites exhibit high level of heterogeneity[122], and it can be predicted that inherent CIN within the cells in ascites may render the cellular populations more heterogeneous, where the cells carrying genetic advantages (e.g. for proliferation, metastasis and adaptation in a novel millieu) may persist. Furthermore, Schwarz *et al.* revealed that ITH present within a tumor prior to treatment correlates with poor survival: upon treatment, the clones with the most survival benefits likely undergo clonal expansion, resulting in accelerated recurrence[124]. Thus, through the induction of ITH, CIN may render a tumor more aggressive by promoting cell survival, growth and acquisition of multi-drug resistance[121,125,126] and therefore, CIN is frequently associated with poor patient prognosis[127]. Despite these associations, the mutated genes and aberrant pathways giving rise to CIN are only poorly understood[118]. Therefore, studies aimed at identifying novel CIN genes and their roles in the pathogenesis of cancer are urgently needed.

1.4.1. Methods to Evaluate CIN

In order to assess whether *RBX1* is a putative CIN gene, cytogenetic experiments need to be performed to evaluate CIN. Traditional approaches include diminishing the expression of a gene of interest either transiently or stably, followed by the generation of mitotic chromosome spreads to evaluate changes in chromosome numbers or structure. Mitotic chromosome spread analysis is labor-intensive but is by far, one of the most reliable methods to detect both numerical and structural CIN. However, this technique can only be applied to actively dividing cell populations and will not detect cells that replicate without undergoing cell division (i.e., cells undergoing endoreduplication). Therefore, employing single cell quantitative imaging microscopy (scQuantIM) to evaluate CIN would complement the karyotypic analyses. CIN-associated phenotypes include changes in nuclear areas (NAs) and micronucleus formation (MNF). Recall that a micronucleus is an extra nuclear body found outside the primary nucleus. MNF commonly occurs due to chromosome segregation errors or defects in DNA repair. As a result, micronuclei may contain whole mis-segregated chromosomes or chromosomal fragments. In general, changes in NAs typically reflect large-scale changes in chromosome content[128] whereas MNF is suggestive of small-scale changes in DNA content or structural CIN[129,130]. Hence, employing scQuantIM along with karyotypic analyses constitute an ideal methodology to assess CIN in *RBX1*-depleted cells and obtain critical insights about its role in maintaining chromosome stability. Also, to accurately validate CIN, it is essential to conduct clonal cell CIN assays. Since CIN is the increased rate of gains and/or losses of entire chromosomes or chromosomal fragments, it is imperative to assess changes in aneuploidy over time, which mandates evaluating CIN at regular intervals[131]. Accordingly, dynamic changes in CIN phenotypes would be indicative of the prevalence of CIN within the clonal cell populations whereas little or no change in phenotypes associated with CIN

would reflect CIN-negative populations. Therefore, performing CIN assays at regular timepoints in clonal populations of *RBX1*-deficient cells would be an ideal start to validate *RBX1* as a CIN gene. Such CIN studies are central to understanding the role of *RBX1* in tumorigenesis and cancer progression.

1.5. Members of the SKP1-CUL1-FBOX (SCF) Complex as Candidate CIN Genes

The SCF complex (Figure 1.0) is an E3 ubiquitin ligase comprised of four proteins, namely RING-Box1 (RBX1), S-phase Kinase associated Protein 1 (SKP1), Cullin1 (CUL1) and an F-box protein. The SCF complex functions to polyubiquitinate target proteins for subsequent degradation via the 26S proteasome[132]. Within the SCF complex, the F-box protein confers substrate specificity to the E3 ubiquitin ligase complex. It is noteworthy that 69 F-Box proteins are encoded in the mammalian genome[133,134], forming a versatile repertoire of SCF complexes for regulating a wide variety of structurally and functionally different protein substrates. The SKP1 component acts as an adaptor molecule[135]. Bound to the CUL1 scaffolding protein, RBX1 protein facilitates ligase activity by recruiting the E2 ubiquitin-conjugating enzyme and transferring the ubiquitin moiety from E2 onto the protein substrates[136]. Protein substrates commonly regulated by the SCF complex include cell cycle regulatory proteins like Cyclin E1, transcription factors, apoptotic proteins, signal transduction factors, DNA repair proteins, oncoproteins and tumor suppressor proteins[134,137-141]. In addition, many substrates regulated by the SCF complex including Cyclin E1[98], PLK4[142] and CDC6[143] are implicated in critical pathways associated with CIN such as centrosome duplication, DNA repair and DNA synthesis. Thus, aberrant SCF complex formation and/or function is predicted to adversely impact numerous proteins and pathways to may impact disease pathogenesis. Recently, the McManus laboratory (Dr. Laura Thompson) screened 164 candidate CIN genes and identified *SKP1* as a putative CIN gene[128]. Her subsequent work revealed that *SKP1* silencing induced increases in CIN phenotypes including increases in nuclear areas (NAs) (suggestive of increases in DNA content), micronucleus (extra nuclear body found outside the primary nucleus; hallmark of CIN[129]) formation, and aberrant chromosome numbers.

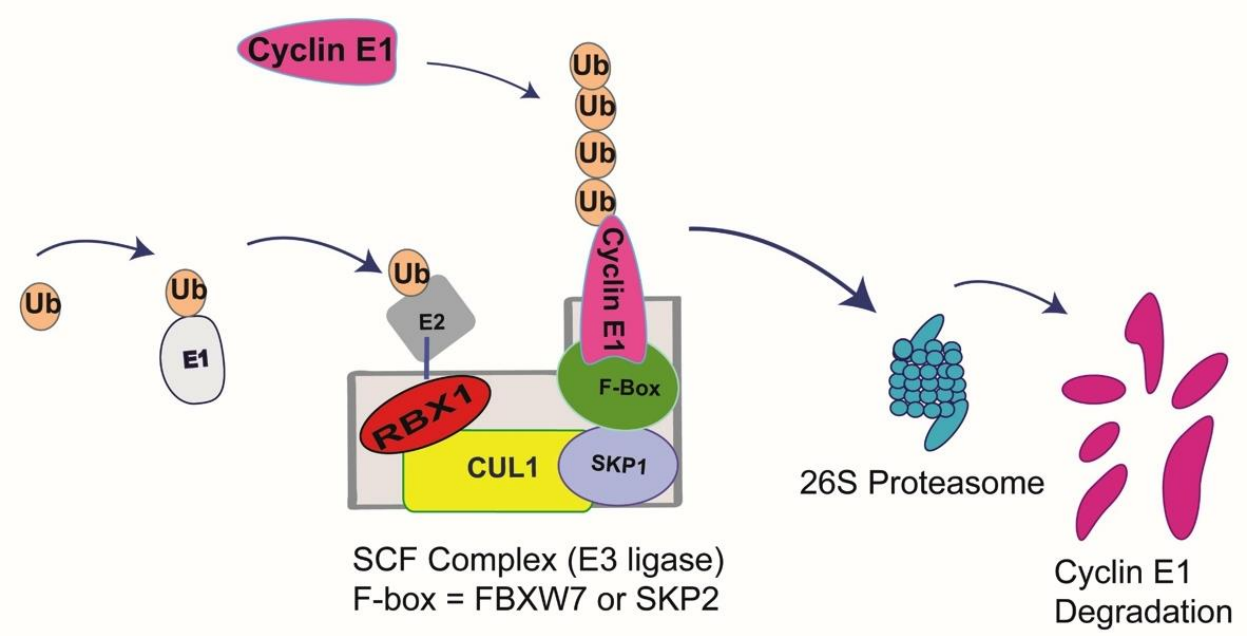

Figure 1.0. Regulation of Cyclin E1 levels by the SCF complex.
Schematic depiction of the SCF complex, the poly-ubiquitination and proteolytic degradation of Cyclin E1 via the 26S proteasome. The SCF complex is comprised of RBX1, CUL1, SKP1 and a F-Box protein (e.g. FBXW7 or SKP2). (Figure created by Manisha Bungsy).

Further, western blot analyses and semi-quantitative imaging microscopy showed that *SKP1* silencing was associated with aberrant increases in Cyclin E1 protein levels (genomic amplification known to induce CIN). Subsequent, indirect immunofluorescence determined that *SKP1* silencing corresponded with increases in centrosome defects, emphasizing the potential importance of the SCF complex in maintaining chromosome stability under normal conditions. Collectively, these data show that reduced *SKP1* results in aberrant SCF function and contributes to CIN, which further suggest that reduced expression of the remaining SCF complex members, such as *RBX1* may also induce CIN phenotypes, potentially through a similar Cyclin E1-based mechanism to promote cancer development. Therefore, obtaining a better understanding of the different components of the SCF complex is imperative as the misregulation of any of the components could lead to impairment in multiple cellular pathways and ultimately result in disease development. In particular, mutations in *RBX1* could have a tremendous impact on cellular health as it is central to the catalytic activity of the complex.

1.5.1. RING-Box1 (RBX1)

RBX1, also known as *Hrt1* (yeast homolog) or *ROC1* (regulator of cullins 1), is evolutionarily conserved from yeast to plants to mammals[144]. *RBX1* is widely expressed across normal human tissues, including heart, muscle, kidney, liver and placenta and exhibits both nuclear and cytoplasmic localization within a cell[144]. Human *RBX1* localises to 22q13 and is comprised of 4 introns and 5 exons[145]. Studies in model organisms have shown that orthologues of *RBX1* are essential genes in mice, yeast and flies, as homozygous loss is associated with lethality[141,145-148]. Collectively, these studies suggest human *RBX1* is an essential gene for which partial loss (e.g. heterozygous loss) may be a pathogenic event. It is also important to note that there is another closely related member to *RBX1*, *RBX2*/*ROC2* (also called Sensitive to Apoptosis Gene [SAG])[149].

However, both RBX proteins have been reported to be functionally distinct and likely regulate different sets of protein substrates[145]. Moreover, the most pertinent difference between the two RBX members is that the expression of *RBX1* is constitutive whereas that of *RBX2* is stress-inducible[144,150,151], which implies that it is expressed only in response to external stimuli such as nitric oxide[152], heat shock[153] and hypoxia[154]. In addition, RBX1 has been shown to interact with all 7 cullins, whereas RBX2 binds predominantly to Cullin 5, which further suggests that RBX1 may be impacting the regulation of a broader range of pathways as compared to RBX2[146,151,155]. Thus, this renders *RBX1* an ideal candidate gene to pursue for further investigation, particularly in the context of CIN-associated pathways, which so far remain unexplored despite being virtually inherent in all cancers.

Human RBX1 is comprised of 108 amino acids with a molecular mass of ~12 kDa[145]. The amino terminus of RBX1 binds to Cul1, whereas the carboxy terminus contains a functional RING-H2 finger domain that is essential for its ligase activity[151,156]. The RING-H2 subunit contains cysteine and histidine residues that form a specific motif for the binding of two zinc atoms per molecule in a unique 3D structure, referred to as the 'cross-brace' structure[144]. Although RBX1 complexes with additional SCF members or components of SCF-like E3 ubiquitin ligases, a recent study revealed that RBX1 can polyubiquitinate proteins independent of the SCF complex[157]. Nevertheless, activation of the SCF complex requires the attachment of a small ubiquitin-like molecule, NEDD8, on a lysine residue on CUL1 (Lys 734 for human CUL1) via a process called neddylation. Interestingly, RBX1 not only catalyzes the ubiquitination of protein substrates but also catalyzes neddylation[158,159]. In addition, RBX1 has also been shown to be involved in stabilizing the interaction between cullins and the enzyme E2[148] as well as promoting nuclear localization of CUL1[158]. All these findings highlight the importance of RBX1 as the functional

unit of the SCF complex, suggesting that altered expression and function of *RBX1* may likely underlie many pathophysiological pathways that rely on E3 ligases for maintaining genome stability and overall normal functioning of the cell.

1.5.2. Alterations of *RBX1* in Cancer

RBX1 is somatically altered (mutated, deleted and amplified) in numerous cancer types and importantly, heterozygous loss of *RBX1* occurs at a much higher frequency in many cancers, including HGSOC (~83%) and colorectal cancer (~25 %) (Table 1.0 and Figure 1.1). Recently, Lin *et al.* have reported frequent loss of heterozygosity of the locus harbouring *RBX1* (22q13) in metastatic breast and thyroid cancers[160]. Importantly, TCGA data show that individuals with reduced mRNA expression of *RBX1* correlate with worse patient survival outcomes than those with high *RBX1* expression levels. Interestingly, these observations are statistically significant in ovarian cancer, and although not significant, do exhibit a similar trend in CRC (Figure 1.2). Collectively, these data suggest that *RBX1* copy number losses may constitute a key pathogenic event in the development and progression of cancer. Since RBX1 is a core SCF complex component, its reduced expression is predicted to impair SCF complex function, and lead to the accumulation oncogenic substrates such as Cyclin E1, which is expected to induce CIN. Accordingly, this thesis seeks to determine the impact reduced *RBX1* expression has on CIN.

Table 1.0. Frequency of *RBX1* Heterozygous Deletions in Six Cancer Types[83,161-166].

Cancer Type	New Cases in Canada Annually[4]	New Cases in U.S. Annually[167]	New Cases in North America Annually	Heterozygous Loss (%)	North Americans with Heterozygous *RBX1* Loss[A]
Breast	27,200	271,270	298,470	33.4	99,688
Colorectal	26,300	145,600	171,900	25.5	43,834
Lung	29,415	228,150	257,565	41.7	107,404
Ovarian	3,000	22,530	25,530	83.2	21,240
Prostate	22,900	174,650	197,550	10.5	20,742
Stomach	4,100	27,510	31,610	53.6	16,942

[A]Calculated by percentage heterozygous loss for each cancer type multiplied by the total number of new cases in North America in 2019.

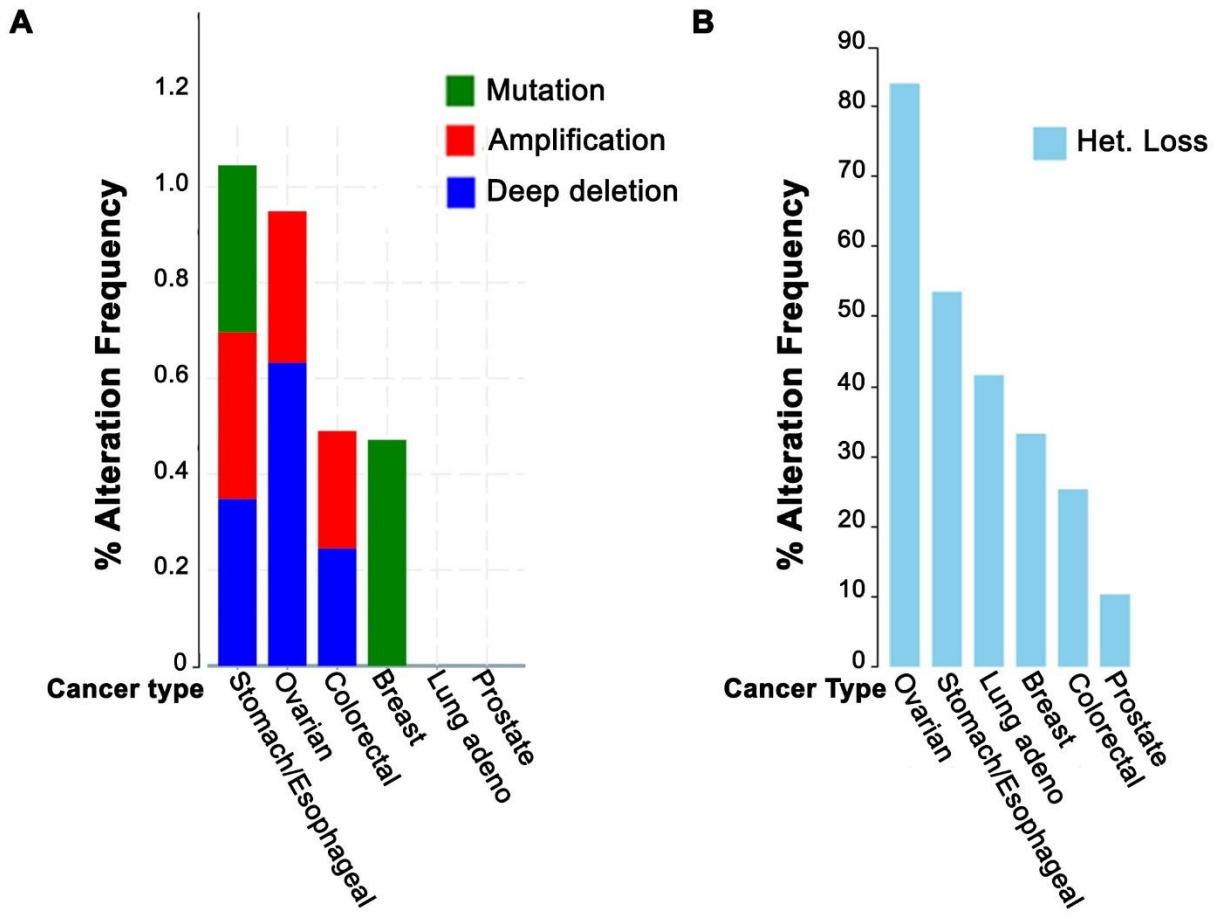

Figure 1.1. Frequency of *RBX1* alterations in select cancer types.
A) Column graph presenting frequency of *RBX1* alterations (mutations, deletions and amplifications) in six common cancer types. ***B)*** Column graph depicting heterozygous loss of *RBX1* (Het. Loss) in six cancer types. (Data obtained from The Cancer Genome Atlas (TCGA) data sets on cBioPortal[83,161-166,168]). Note that the frequency of heterozygous loss is ~83% and ~25% for ovarian and colorectal cancer, respectively.

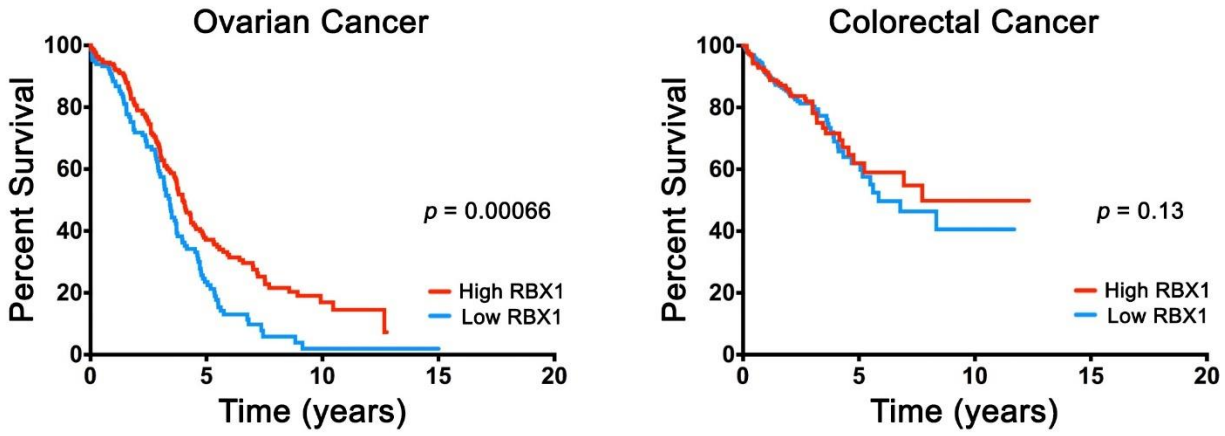

Figure 1.2. Diminished *RBX1* expression is associated with worse overall survival in colorectal and ovarian cancers.

A) Kaplan-Meier (KM) curves reveal that ovarian (left) and CRC (right) cancer patients harboring low *RBX1* expression (mRNA) generally correlate with worse patient survival relative to those with high *RBX1* expression[83,161]. Log-rank tests identifies a statistically significantly worse outcome for ovarian cancer, and only a similar trend for CRC (not statistically significant).

1.5.3. Role of *RBX1* in DNA Damage Repair

DNA damage poses a considerable threat to genome integrity. DNA insults may occur as a result of endogenous processes (e.g. cellular metabolic activities or replication errors), or exogenous DNA damage caused by UV light, environmental mutagens and ionizing radiation. Many complexes work in an orchestrated manner to rapidly recognize and repair DNA damage that occurs frequently within the cell. Arguably, the most detrimental lesions to the genome are DNA double strand breaks (DSBs) that are repaired through one of two pathways; 1) 'error-prone' non-homologous end-joining (NHEJ); and 2) 'error free' homologous recombination repair (HRR). Although NHEJ is the predominant DSB repair pathway in mammals and can occur throughout G1, S and G2 phases of the cell cycle, HRR dominates during G2 and S phases[169]. In addition, protein ubiquitylation plays a critical role in the DNA damage response, where it regulates protein stability, localization and activity. Interestingly, RBX1 complexes with other proteins to mediate key ubiquitination events during the DNA DSB repair process. For example, during HRR, KEAP1-CUL3-RBX1 E3 ligase molecule plays an important role in the ubiquitination of the amino terminal of PALB2[170]. PALB2 acts as a molecular adaptor between the BRCA proteins where it forms a complex with BRCA1, BRCA2, and RAD51 to mediate the repair of DNA double strand breaks[171-173]. Importantly, the interaction between BRCA1 and PALB2 is dependent on the ubiquitination on PALB2. In addition to HRR, RBX1 participates in nucleotide excision repair (NER) pathway, as part of the DDB1-DDB2-RBX1-CUL4A/4B complex. During NER, UV-induced DNA damage lesions are removed by a process involving ubiquitylation of histone H2A by the E3 ligase complex containing RBX1[174,175]. Thus, presumably, reduced *RBX1* expression may also adversely impact NER and potentially induce genome

instability. Therefore, studies aimed at investigating the impact of loss of *RBX1* expression on genome stability or CIN will help shed light on the role of *RBX1* in genome maintenance.

CHAPTER 2: RATIONALE, HYPOTHESIS AND RESEARCH AIMS

2.1 Rationale

Preliminary data from the McManus laboratory revealed *SKP1* (SCF complex member) as a putative CIN gene[128] (See Section 1.5, Page 18). Additional experiments performed in CRC cells showed that reduced *SKP1* expression induced increases in CIN phenotypes, abnormal increases in Cyclin E1 protein levels as well as centrosome defects (Unpublished Data by Dr. Laura Thompson). These findings underline the potential importance of the SCF complex in maintaining chromosome stability under normal conditions. Collectively, these data indicate that diminished *SKP1* underlies aberrant SCF function and contributes to CIN and suggest that diminished expression of the remaining SCF complex members (*i.e. RBX1*) may result in similar CIN phenotypes, possibly through a similar Cyclin E1-based mechanism, and contribute to oncogenesis.

Increased Cyclin E1 levels stemming from genomic amplification has been found to induce CIN and contribute to the pathogenesis of many cancers, including HGSOC[94,98-103]. We predict that, independent of the genomic status, elevated levels of Cyclin E1 could also result from its impaired turnover, likely due to reduced *RBX1* expression and aberrant SCF function. Recall that RBX1 is central to the catalytic function of the SCF complex and thus, even a partial loss is predicted to have detrimental effects which could include CIN. Besides, the strikingly high frequency of heterozygous *RBX1* loss in HGSOC (>80% of patient samples) further suggests that *RBX1* may indeed have a fundamental role in driving early disease development and progression. Therefore, evaluating the long-term impact of $RBX1^{+/-}$ on CIN and cellular transformation would help to model early disease development in HGSOC. Developing a better understanding of the early pathogenic mechanisms underlying CIN and oncogenesis in HGSOC is critical in order to

devise better treatment strategies, improve patient outcomes and reduce the disease burden prevailing in HGSOC which is the most common and lethal gynaecological cancer.

2.2 Hypothesis

I hypothesise that diminished *RBX1* expression underlies increases in Cyclin E1 levels that will induce CIN and contribute to cellular transformation.

2.3 Research Aims

Aim 1: To evaluate the impact transient RBX1 silencing has on Cyclin E1 levels and CIN.

Aim 2: To assess the impact heterozygous loss of *RBX1* (*RBX1*$^{+/-)}$ has on Cyclin E1 levels, CIN and cellular transformation in fallopian tube secretory epithelial cells (FTSECs).

CHAPTER 3: MATERIALS & METHODS

3.1. Reagents

Appendix A contains a list of the solutions and the reagents used throughout this study. All reagents were purchased from Corning, Fisher Scientific, Fisherbrand, Froggabio, Gibco, Invitrogen, New England Biology labs, Sarstedt, Sigma-Aldrich, and VWR.

3.2. Cell Culture

For reference purposes, the common properties of the human cell lines utilised in this study are summarized in Table 3.1. HCT116 cells (human epithelial colorectal cancer cell line) and OVCAR3 (HGSOC cell line) were purchased from American Type Culture Collection (Rockville, MD). FT194 and FT246 cells (human immortalized secretory epithelial fallopian tube cell lines) were generously provided by Dr. R. Drapkin (Dana Farber Cancer Institute, MA). The cell lines were characterised based on viability, doubling times, cellular morphology and spectral karyotyping[176]. HCT116 cells were cultured in modified McCoy's 5A (HyClone, Logan, UT) supplemented with 10% fetal bovine serum (FBS) (Sigma-Aldrich). OVCAR3 cells were grown in Roswell Park Memorial Institute-1640 (RPMI-1640) medium supplemented with 10% FBS and 0.01 mg/mL insulin (Gibco). FT194 and FT246 cells were grown in Dulbecco's Modified Eagle's Medium (DMEM)/Ham's F12 1:1 (HyClone, Logan, UT) supplemented with 2% serum substitute Ultroser G (Pall France, St-Germain-en-Laye Cedex, France).

Table 3.1. Common Properties of the Cell Lines Employed in this Study

	HCT116	OVCAR3	FT194	FT246
Species	*Homo sapiens*	*Homo sapiens*	*Homo sapiens*	*Homo sapiens*
Tissue	Colon	Fallopian Tube	Fallopian Tube	Fallopian Tube
Cell Type/Disease	Epithelial, Transformed, Malignant, Colorectal Cancer	Secretory Epithelial, Transformed, Malignant, Ovarian Cancer	Secretory Epithelial, Immortalized (TERT, SV40 Tag), Non-transformed, Non-malignant	Secretory Epithelial, Immortalized (TERT, p53shRNA +CDK4-R24C), Non-transformed, Non-malignant
Sex	Male	Female	Female	Female
Culture Medium	McCoy's 5A with 10% Fetal Bovine Serum	RPMI-1640 + 10% FBS + 0.01 mg/mL Insulin	DMEM/Ham's F12 50/50, with 2% Ultroser G	DMEM/Ham's F12 50/50, with 2% Ultroser G
Doubling Time	~22 h	~48 h	~24 h	~40 h
Karyotype	45, XY, Stable	46, XX, Unstable	46, XX, Stable	46, XX, Stable
Source	American Type Culture Collection	American Type Culture Collection	Drapkin Laboratory	Drapkin Laboratory

3.2.1. Cell Passaging

Cells were grown in 10 cm tissue culture dishes (Sarstedt) at subconfluent levels at 37°C in a humidified incubator supplied with 5% CO_2. To maintain cell viability, cells were passaged twice weekly in a biological safety cabinet. Briefly, culture medium was aspirated, the cells were rinsed with sterile phosphate buffered saline (1×PBS) (Appendix A) and 1.5 mL of trypsin (0.05% + 0.53 mM EDTA) (Gibco; Life Technologies) was added. Cells were incubated (3 min at room temperature for HCT116; 5-8 min at 37°C for OVCAR3, FT194 and FT246) and monitored using an inverted ID03 microscope (Zeiss) with a 10× objective (Zeiss) to ensure all cells had detached from the culture plate. 3 mL of complete medium was added to inactivate the trypsin. Additionally, 4 mL of 1× PBS was pipetted to wash the cells off the plate. Cells were transferred to a 15 mL conical (Sarstedt) and centrifuged (1400×g, 21°C for 5 min, Sorvall Legend XFR; ThermoScientific). The supernatant was aspirated, the cell pellet was resuspended in sterile 3-6 mL of 1× PBS, and seeded at 30-40% confluency into a 10 cm dish containing 10 mL of complete media.

3.2.2. Cell Counting and Seeding Protocol

Table 3.2 summarizes the different cell seeding densities adapted for the various experiments performed during this study. Cells were harvested as described above (Section 3.2.1). Following centrifugation and supernatant aspiration, the cell pellet was resuspended in ~5 mL of 1× PBS and transferred to a 50 mL conical tube (Sarstedt) by filtering through a 40 µm strainer (Falcon) to eliminate cell aggregates and ensure a single cell suspension. A 40 µL aliquot of the cell suspension was mixed with an equal volume of 0.2% trypan blue stain (Gibco) in a 0.5 mL microcentrifuge tube. A 10 µL aliquot of the mixture was dispensed in duplicate in a cell counter slide compartment (Cedex Smart Slide, Roche). Images of cells within both compartments were acquired using the

Cedex XS (Roche) cell counter. Viable cells were distinguished from the dead cells through standard dye exclusion by the image analysis software of the cell counter and an average concentration of viable cells/mL of PBS solution was obtained. This value was employed to calculate the appropriate volumes of cell suspension to be diluted in complete media, such that the required cell seeding densities can be applied in the corresponding vessels for various experiments performed in this study (Table 3.2). Cell seeding densities were optimized to maintain cells in the growth phase and at equivalent confluence across all conditions at the end of the experiment.

Table 3.2. Cell Seeding Densities for Various Experiments

Experimental Approach[A]	Plate Format	Cell Line	Days[B]	Cells ($\times 10^3$) (Exp)[C]	Cells ($\times 10^3$) (Control)[D]
WB	6-well plate	**HCT116**	4	120	40-70
		FT194	4	85	40-70
		FT246	6	95	50-75
NA, MNF	96-well plate	**HCT116**	4	1	1
		FT194	4	1	1
		FT246	6	2	2
MCS	6-well plate	**HCT116**	4	60	15
		FT194	4	30	20
		FT246	6	30	20

[A]Abbreviations of experiments/analyses performed: WB (western blot), NA (nuclear area), MNF (micronucleus formation), and MCS (mitotic chromosome spread).
[B]Days = Experiment time course (post-transfection).
[C]Cell numbers (in thousands) seeded in experimental wells (*e.g. RBX1* silencing).
[D]Cell numbers (in thousands) seeded in control wells (*e.g.* Untreated and Non-targeting).

3.3. siRNA-based Approach for Gene Knock-Down

In general, forward transfection (i.e., cells seeded prior to transfection) was performed. siRNA and transfection reagent conditions were optimized based on cell viability as well as silencing efficiency which was determined by western blot analyses (Section 3.4). Prior to siRNA transfection, cells were processed and counted as described above (Sections 3.2.1 and 3.2.2). Appropriate cell densities for each cell type (HCT116, FT194 and FT246) and condition were seeded into each well of a 6-well tissue culture plate (Falcon; Corning) either without a coverslip to harvest proteins for western blot analyses, or containing 70% Ethanol-sterilized (Appendix A) coverslips (18 x 18; Fisherbrand) for microscopy-based karyotypic analyses, or 96-well optical bottom plates with polymer base (Thermo Fisher Scientific) for quantitative imaging microscopy (Table 3.2). Cells were allowed to attach to the bottom of the plate and grow for 24 h before transfecting them by RNAiMAX (Invitrogen) lipid-based transfection approach as detailed below.

A set of four individual ON-TARGETplus siRNA duplexes (2 nmol) targeting unique coding regions for *RBX1* and Non-targeting control siRNA (that does not target any coding region in the human genome) were purchased from Dharmacon (Reference Number: LU-004087-00-0002). All four siRNA duplexes were resuspended in 1× siRNA buffer (Appendix A) to make a stock concentration of 20 µM. To ensure complete resuspension, the four tubes were vortexed at room temperature for 30 min (Vortex Genie 2, VWR). A working concentration of 10 µM was prepared for each individual siRNA by diluting the 20 µM stock solutions with 1× siRNA buffer in a 1:1 ratio. Furthermore, a 10 µM siRNA pool was prepared by combining equivalent volumes of all four distinct 10 µM siRNA duplexes. Small aliquots (e.g. 10 µL) of siRNA were made and stored at -80ºC in order to minimise freeze-thaw cycles.

To silence *RBX1*, cells were seeded in appropriate numbers (Table 3.2) 24 h prior to transfection. The volumes of siRNA, RNAiMAX and serum free media (SFM) employed across different cell lines for silencing in a 6-well plate are summarized in Table 3.3. For experiments requiring different seeding densities, the siRNA, RNAiMAX and SFM volumes were adjusted based on the number of cells seeded in each well. In general, to silence *RBX1* in HCT116 in a 6-well plate, 1 µL of 10 µM siRNA was added to 249 µL SFM in a 1.5 mL microcentrifuge tube and 6 µL of RNAiMAX was added to 244 µL SFM in another tube. The individual solutions were mixed gently. Next, the RNAiMAX solution was added to the tube containing siRNA solution, the tube was inverted gently to mix and incubated at room temperature (RT) for 20-25 min to allow for lipid complex formation. After incubation, the lipid complexes were gently delivered to the cells dropwise. Plates were rocked gently and returned to the incubator for the duration of the experiment (Table 3.2), at which point they were treated accordingly, depending on the experimental approach to follow (protein extraction, fixation, *etc.*). Silencing efficiency was validated by western blot analyses as described in Section 3.4.

Table 3.3. siRNA and RNAiMAX Volumes Employed for Transfection in 6-well Plates

Cell Line	Cells ($\times 10^3$) /Well	Volume of 10 µM siRNA (µL)	Volume of SFM (µL)	Volume of RNAiMAX (µL)	Volume of SFM (µL)	Total Transfection Volume (µL) /Well
HCT116	120	1.0	249.0	6.0	244	500
FT194	85	0.5	249.5	4.0	246	500
FT246	95	0.5	249.5	4.0	246	500

3.4. Western Blot Analyses

Western blot analyses were performed to validate silencing efficiency and to screen for *RBX1*-edited FT246 clones based on diminished RBX1 protein expression levels. Additionally, western blot analyses were employed to evaluate changes in Cyclin E1 levels, post *RBX1*-silencing or CRISPR-Cas9 mediated gene knockout.

Cells were seeded (Table 3.2), transfected with si*RBX1* or control, and cultured in 6-well tissue culture plates (Falcon; Corning) as described above (Table 3.3). Before protein extraction, cell culture medium was aspirated, and cells were washed with cold 1× PBS three times. In a cold room (4°C), ~200 mL of lysis buffer (Appendix A) was added to each well and incubated for 5 min. Cell scrapers (VWR) were used to collect protein lysates from each condition, which were subsequently transferred to labelled individual 1.5 mL microcentrifuge tubes. Using the Sonifer Cell Disrupter (Branson Sonic Power Co.), samples were sonicated in two rounds for 3 s each with a duty cycle of 50% and an output control setting of 6. Samples were centrifuged (Biofuge Fresco; Thermo Scientific) at 13,000 rpm at 4ºC for 2 min to pellet insoluble cell debris. The supernatant containing soluble protein extract was transferred into a sterile 1.5 mL microcentrifuge tube and stored at -20ºC for short-term storage (< 2 weeks) or at -80ºC for long-term storage (> 2 weeks).

Protein quantification was performed using a Pierce Bicinchoninic Acid (BCA) Assay kit (Thermo Scientific) as described in manufacturer's manual. The concentration of each protein lysate was calculated by comparing its absorbance (at 562nm) value to that of a standard curve plotted from a series of 9 Bovine Serum Albumin (BSA) protein standards. The Cytation 3 Cell Imaging Multi-Mode Reader (BioTek) was utilised to measure absorbance values for the unknown samples as well as the protein standards.

Following protein quantification, standard western blotting was performed by employing polyacrylamide gel electrophoresis. For each condition, samples containing 20 µg of protein were mixed with 6× sodium dodecyl sulphate/dithiothreitol (SDS/DTT) sample loading buffer (β-mercaptoethanol) and radioimmunoprecipitation assay (RIPA) buffer (Appendix A) to a maximum volume of 30 µL. Samples were incubated in a Thermomixer R (Eppendorf) at 95°C for 10 min with 1 min intermittent orbital shaking at 700 rpm to denature proteins. Following denaturation, samples were cooled to RT and were loaded into pre-rinsed wells of gels (BioRad, 4-20% mini-Protean TGX) along with BLUelf Prestained Protein Ladder (Froggabio). Samples were electrophoresed in a gel apparatus (BioRad, Miniprotean) containing 1× Running Buffer (Appendix A) under constant voltage (140 V) using a PowerPac HC (BioRad) power supply for 65 min at 4°C. Polyvinylidene difluoride (PVDF) membranes (Millipore) of 0.2 µm pore size were activated with a flash rinse of methanol (VWR) and washed three times with Milli-Q water. Following gel electrophoresis, proteins were transferred onto the PVDF membranes at a constant voltage (14 V) at RT for 45 min in a TransBlot SD Semi-Dry Transfer Cell (Bio-Rad) containing 1× Transfer Buffer (Appendix A).

To confirm effective protein transfer, PVDF membranes were stained with copper phthalocyanine 3,4’,4’’,4’’’-tetrasulfonic acid tetrasodium salt (CPTS) (Appendix A) at RT for 10 min. Membranes were destained by gentle washing in 1× Tris-buffered saline solution containing 0.1% Tween 20 (1× TBST) (Appendix A) for 5 min. The membranes were blocked with 5% non-fat milk in 1× TBST (Appendix A) at RT for 1 h with gentle shaking. Following blocking, membranes were probed with appropriate primary antibodies (Table 3.4) diluted in ~5 mL of 5% non-fat milk, by incubating overnight at 4°C on an

Table 3.4. List of Antibodies Employed in this Study

Primary Antibodies			
Protein of Interest[A]	**Species**	**Catalog Number**	**Dilution**
α-Tubulin*	Mouse	Abcam; ab7291	1:4,000
CCNE1	Rabbit	Abcam; ab133266	1:5,000
Cyclophilin B*	Rabbit	Abcam; ab16045	1:50,000
RBX1	Rabbit	Abcam; ab133565	1:30,000
Secondary Antibodies			
Anti-Rabbit HRP	Goat	Jackson ImmunoResearch; 111-035-114	1:15,000
Anti-Mouse HRP	Goat	Jackson ImmunoResearch; 115-035-146	1:10,000

[A]The protein targeted by the antibody. Note: Proteins marked with an asterisk represent western blot loading controls. HRP = horse radish peroxidase.

orbital shaker. The next day, primary antibody solution was removed, and membranes were washed three times with 1× TBST (Appendix A) for 10 min each with gentle agitation. Membranes were incubated at RT for 1 h under gentle shaking in secondary antibody (Table 3.4) conjugated to horse radish peroxidase (HRP) diluted in ~5 mL of 5% non-fat milk. Following incubation, membranes were washed with 1× TBST as detailed above, and incubated in ~1 mL of chemiluminescent substrate SuperSignal West Dura Extended Duration Substrate (Thermo Scientific) at RT for 5 min. After removing excess substrate, the membranes were placed into a plastic clear sheet protector and protein bands were visualized using the MyECL imager (Thermo Scientific). Membranes were imaged with varying exposure times for optimal signal intensity. Images were acquired and exported as TIFF files, while figures were assembled in Photoshop CS6 (Adobe) and analysed using Image J software.

3.5. Single Cell Quantitative Imaging Microscopy

Single cell quantitative imaging microscopy (scQuantIM) was employed to evaluate changes in NA and MNF (Sections 3.5.1 and 3.5.2) and to analyse MCS (Section 3.6).

3.5.1. Cell Fixation and DNA labelling for NA and MNF Analyses

Following silencing in the 96-well plates (Section 3.3), cell culture medium within each well was aspirated and cells were fixed with 100 µL of freshly prepared 4% paraformaldehyde (Appendix A) for 10 min at RT. Cells were washed three times in 1× PBS (Appendix A) and counterstained with 100 µL of Hoechst 33342 (300 ng/mL) (Appendix A). 96-well plates were kept at 4°C protected from light overnight before performing microscopy to ensure uniform Hoechst labeling.

3.5.2. Image Acquisition and Analysis

Images were acquired from the 96-well plates using a Cytation 3 Cell Imaging Multi-Mode Reader (Bio-Tek) microscope equipped with a charge-coupled device camera (Sony) and an Olympus 20× objective (0.45 numerical aperture). Gen5 software (Bio-Tek) was used to control exposure times, which were optimized for the Hoechst channel (Semrock DAPI filter). In addition, primary nuclear size (ranging from 10 μm to 100 μm in diameter) as well as Hoechst intensity thresholds were applied to exclude partial nuclei, cellular debris, apoptotic and mitotic nuclei. For MNF analysis, the Gen5 Spot Counting module was employed to detect micronuclei situated outside the primary nucleus[177]. A size threshold was applied to detect micronuclei ranging between 1 μm and 6 μm in diameter. Additional Hoechst intensity thresholds were employed to exclude cellular debris, mitotic chromosomes and apoptotic bodies. The defined thresholds were optimized for every experiment and maintained across all conditions within the experiment. A minimum of 500 nuclei per condition were analysed for MNF and NA analysis. All data were imported to Prism v6.0 (GraphPad), where statistical analyses (Section 3.9) were performed and graphs were generated. Graphs were imported into Photoshop CS6 where figure panels were assembled.

3.6. Mitotic Chromosome Spread Generation and Enumeration

To generate mitotic chromosome spreads, cells were seeded onto ethanol-sterilized coverslips in 6-well tissue culture plates, silenced (Table 3.2), and allowed to grow for 4 days (for HCT116 and FT194) or 6 days (for FT246) as described above. Cells were mitotically enriched using KaryoMAX colcemid (Gibco) (Appendix A) at a dilution of 10 μL/mL in complete media for 2 h (HCT116), 2.5 h (FT194), or 3.5 h (FT246), prior to harvesting. Following colcemid treatment, the medium was aspirated, and the cells were treated with 2 mL of 75 mM potassium

chloride (KCl) hypotonic solution (Appendix A) at RT for 16 min (HCT116), 3 min (FT194) or 10 min (FT246). Cells were fixed with a freshly prepared 3:1 mixture of methanol:acetic acid (Appendix A) in three 10 min intervals. Fixative was removed and coverslips were air-dried and mounted onto glass microscope slides with 10 µL DAPI Mounting Media (Appendix A). Slides were stored protected from light at 4°C for at least 24 h before microscopy was performed.

Mitotic chromosome spreads were imaged using an AxioImager Z1 microscope equipped with a 63× (1.4 numerical aperture) oil-immersion, plan apochromat lens and a Zeiss HRm CCD camera. Images from a minimum of 100 spreads per condition were acquired as TIFFs, which were imported into FIJI software for manual chromosome counts and phenotypic evaluation. In general, deviations from the modal chromosome number for each cell line employed (Table 3.1) were classified as losses (< 45 for HCT116 and < 46 for FT194 and FT246), small-scale gains (46-59 for HCT116 and 47-59 for FT194 and FT246) and large-scale gains (> 59). Chromosome enumeration data were imported into Prism v6.0 (GraphPad) where statistical analyses (Section 3.9) were performed and graphs were generated. All figure panels were assembled using Photoshop CS6.

3.7. CRISPR/Cas9 Approach for Generating *RBX1*$^{+/-}$ FT Cells

To generate clonal populations of heterozygous *RBX1*-knockout (*RBX1*$^{+/-}$) FT cells, a CRISPR-Cas9 gene editing approach was employed. Lentiviral CRISPR plasmids expressing Blue Fluorescent Protein (BFP) reporter gene and guide strands targeting either the coding sequence of *RBX1* (gRNA) (Table 3.5) or control guides (non-targeting or NTgRNA) were purchased from Sigma and subsequently packaged to produce lentiviruses (Sections 3.7.1 and 3.7.2). The FT246 cells were transduced with lentiviral particles (Section 3.7.2) and successfully transduced cells

Table 3.5. gRNA Sequences Employed in this Study and *RBX1* Target Sites

sgRNA	Sequence	Target Site
sg*RBX1*-1	5’ CCTGGGATATTGTGGTTGATAAC 3’	Exon 2
sg*RBX1*-2	5’ CATCTGCAGGAACCACATTATGG 3’	Exon 2

expressing the gRNA along BFP were sorted by Fluorescence Activated Cell Sorting (FACS) (Section 3.7.4). Cells were expanded and transiently transfected with a Cas9 expression plasmid that co-expresses Green Fluorescent Protein (GFP) (Section 3.7.3). Successfully transfected cells expressing both GFP (transient Cas9 expression) and BFP (constitutive sgRNA expression) were FACS sorted and clonally expanded (Section 3.7.5). As per standard protocol, a minimum of two clones were isolated, characterized and employed in all subsequent work.

3.7.1. Lentiviral gRNA Plasmid Preparations

To amplify the plasmids, glycerol stocks containing gRNA were inoculated into 5 mL Luria-Bertani broth (LB) (Appendix A) solutions supplemented with 60 µg/mL carbenicillin (Appendix A) (Sigma Aldrich). Broth cultures were incubated overnight at 37°C with intermittent agitation. Following overnight incubation, plasmid DNA was extracted and purified using a QIAprep Spin Miniprep kit (Qiagen) according to the manufacturer's instructions. DNA concentrations and purities were determined using a Nano-Drop spectrophotometer (ThermoScientific). Prior to producing lentiviruses, plasmid DNA was concentrated to 1 µg/µL using a centrifugal evaporator and stored at -20 °C.

3.7.2. Lentiviral Production and Transduction

All lentiviral manipulations were done in a certified Class 2-regulated (Class 2-R) biological safety cabinet specific for virus handling in ON6041A, at CancerCare Manitoba. HEK293T cells were used to package and produce lentivirus particles. Approximately 4.5×10^6 cells were seeded into a 10 cm plate (BD BioCoat cellware, collagen Type I) and allowed to grow for 24 h at 37°C in DMEM supplemented with 10% tetracycline-free FBS (Appendix A). Cells were transfected the next day according to manufacturer's instructions in the Lenti-X HTX Packaging system manual (Clontech). More specifically, 7 µl of vector DNA (i.e. plasmid carrying

gRNA [1 µg/µl]), was added to a mixture of containing 36 µl of Lenti-X HTX Packaging Mix 2 (Clontech) and 557 µl of Xfect reaction buffer (Clontech) in a 2 mL microcentrifuge tube. In another 2 mL microcentrifuge tube, 592.5 µL of Xfect reaction buffer was added and mixed with 7.5 µL of Xfect polymer (Clontech). The two tubes were vortexed at medium speed for 10 s to mix the contents and allowed to incubate at RT for 10 min to allow nanoparticle formation. Next, the culture medium was removed from the plate containing the HEK293T cells and the cells were transfected by adding 1.2 mL of the above mixture. After rocking gently to mix the cells with the transfection mixture, the plates were incubated at 37°C overnight. The following day, medium was removed and fresh pre-warmed DMEM medium supplemented with 10% tetracycline-free FBS was added to the cells, which were subsequently grown for 2 additional days at 37°C before harvesting lentiviral particles.

To confirm the presence of lentiviral particles, a detection kit (Lenti-X GoStix, Clontech) was used as per manufacturer's guidelines. The medium containing lentiviruses was filtered through a low protein binding 0.2 µm filter (Millipore, Billerica, MA) to remove cellular debris and the filtered medium was transferred to a sterile 50 mL conical and cooled to 4°C. To enhance lentiviral concentrations, a Lenti-X concentrator kit (Clontech) was employed, whereby the lentiviral solution was mixed with 3 mL of Lenti-X concentrator and incubated at 4°C for 24 h. After incubation, lentivirus particles were harvested by centrifugation at 1,500× g at 4°C for 45 min. Next, the supernatant was aspirated and disposed of according to biosafety measures for handling lentiviral content. The pellet containing lentiviruses was resuspended in 1 mL sterile ice-cold PBS, aliquoted in 500 µL microcentrifuge tubes and stored at -80°C.

Before performing lentiviral transduction, lentiviral titers were determined to identify the lentivirus concentration which would result in the highest transduction efficiency. Briefly, 50,000

FT246 cells/well were seeded into a 24-well plate (Costar, Corning, NY) 24 h prior to transduction. On the day of transduction, a two-fold serial dilution of virus-to-serum free medium ratio ranging from 1:2 to 1:16 was made. After removing the medium and rinsing the wells with 1× PBS, 100 µl of transduction mixture was added to the appropriate wells. The cells were incubated for 4 h at 37°C. Following 4 h incubation, 400 µl of pre-warmed complete medium was added to each well and the cells were incubated overnight at 37°C. The following day, the medium was removed and discarded according to biosafety standards. Next, cells were rinsed with 1× PBS, complete medium was added, and the cells were grown for 48 h prior to sorting by FACS. (Section 3.7.4.). The concentration of virus resulting in the highest transduction efficiency was determined by FACS and employed for subsequent transduction in FT246 cells as described above. To increase the probability of an editing event, both single guide (targeting a single coding region of *RBX1*) and dual guide strands (simultaneously targeting two distinct coding regions of *RBX1*) were employed. After transduction, the cells were expanded until a confluent 10 cm dish was obtained for each condition. The cells were sorted by FACS (Section 3.7.4.) to enrich for BFP-positive cells, which were collected, further expanded and frozen down for subsequent experiments. One of two distinct *SKP1*-targeting sgRNAs.

3.7.3. Transient Cas9 Transfection

After expanding the BFP-positive FT246 cells constitutively expressing either the gRNA targeting *RBX1* or a control gRNA (NTgRNA), cells were transfected with Cas9 expression plasmid that also expressed GFP. Lipid-based transfection (Effectene [Qiagen]) was performed as per manufacturer's recommendations. Briefly, ~2.0× 10^6 cells were seeded into a 10 cm plate and allowed to grow in complete medium for 24 h at 37 °C prior to transfection. On the day of transfection, 2 µg of Cas9 plasmid DNA was mixed with 300 µL of Buffer EC and 16 µL of

Enhancer reagent in a 1.5 mL microcentrifuge tube. The mixture was vortexed for 1 s and incubated at RT for 5 min. After incubation, 60 μL of Effectene was added, mixed by pipetting and incubated at RT for 10 min. Finally, 3 mL of complete medium was added to the transfection reagent, mixed carefully and added to the plates dropwise. The medium containing the transfection mixture was removed after an initial incubation of 10 h at 37°C and after replenishing the medium, the cells were incubated for an additional 14-20 h at 37°C before FACS (Section 3.7.4.).

3.7.4. Fluorescence-Activated Cell Sorting

Cells were harvested for FACS, 24-30 h post-transfection as described in Sections 3.2.1 and 3.2.2. After performing a cell count, cells were centrifuged and resuspended in 300-500 μL of appropriate sorting buffer (Appendix A). For gating purposes and differentiating between live and dead cells, propidium iodide (PI) was included in the sort buffer. After resuspension, samples were maintained on ice and protected from light until sorting. All FACs analyses were performed by Dr. Monroe Chan using a MoFlo XDP cell sorter (Beckman Coulter) in the Regenerative Medicine Flow Cytometry Facility at the University of Manitoba.

FACS was performed to isolate cells successfully transfected with the Cas9 expression plasmid construct which co-expresses GFP. Since the cells already constitutively express BFP, a dual sort was performed for isolating BFP and GFP positive FT246 cells. Parental (untransduced, BFP- and GFP-negative) and untransfected (BFP-positive, GFP-negative) FT246 cells were used as controls to define appropriate gating parameters. After establishing appropriate gates, all live FT246 cells (i.e., PI-negative) expressing the dual fluorescent markers (BFP and GFP) were bulk sorted into complete collection media (Appendix A). Following sorting, the cells were transferred to 5 mL tubes, centrifuged, resuspended in ~200 μL of 1× PBS and seeded in one well of a 6-well plate for each condition. Bulk sorted cells were further expanded, passaged to larger vessels until

appropriate numbers could be frozen and stored for subsequent experiments.

3.7.5. Clonal Population Generation and Screening for *RBX1*$^{+/-}$ FT Clones

To generate clonal populations of CRISPR-mediated *RBX1*-edited FT246 cells, a limiting dilution of the bulk sorted cells was performed. Briefly, cells were seeded into a 96-well plate to achieve a density of 1 cell per well. Plates were observed every 3-4 days for one month where wells containing a single colony were followed (any well having more than one colony was omitted). As the clones derived from a single cell grew and reached 70-80 % confluency, they were passaged into 24-well plates. As the clones reached confluency in the 24-well plates, they were split to make a duplicate 24-well plate. Protein extraction was performed for each clone from one of the 24-well plates while the replica plate was maintained for expanding and freezing down the clones for subsequent analysis. After protein extraction, clones were screened for successful *RBX1* editing by western blots (Section 3.4). The clones harboring potential *RBX1*-edited allele were chosen and expanded further for validation via DNA sequencing.

3.7.6. DNA Extraction, Polymerase Chain Reaction and Agarose Gel Electrophoresis

To perform DNA sequencing, DNA was extracted from candidate FT246 clones harboring potential *RBX1*-edits. Briefly, a DNeasy Blood & Tissue Kit (Qiagen) was employed according to manufacturer's protocol for DNA extraction, and DNA was eluted in ~200 μL Molecular Biology Grade Water (HyClone). A Nano-Drop spectrophotometer (Thermo Scientific) was used to determine DNA concentration and purity for each sample, which were stored at -20°C.

Polymerase chain reaction (PCR) was employed to amplify the potentially edited genomic locus surrounding the gRNA recognition site, (i.e., exon 2 of *RBX1*). Primers were designed for exon 2 using Primer Tree with forward and reverse sequences shown in Table 3.6. To enable subsequent subcloning (Section 3.7.8.) using the same primer set, a 15-base pair (bp) extension

Table 3.6. Primers Sequences Employed in this Study

Primer	Sequence[A]	TM (°C)
Forward	5’ GGTACCCGGGGATCGTGGCCAAAGAGATGATAACTGC 3’	**61.2**
Reverse	5’ CGACTCTAGAGGATCTTCTGAGAGCTGGGTATGCCT 3’	**62.6**

[A] Primers comprise of 5’ complementary sequence to pUC19 cloning vector (in red) and 3’sequence homologous to *RBX1* (black).
[B] Melting temperatures of primers for the RBX1-coding region only.

corresponding to cloning site within the pUC19 vector was added to 5' region of each primer. To ensure robust and accurate PCR amplification, a Q5 High-Fidelity DNA Polymerase (New England BioLabs) was employed. The PCR reaction mixture was prepared according to manufacturer's instructions for the DNA polymerase as detailed in Table 3.7. Next, PCR was performed at a denaturing temperature of 98°C for 40 s, followed by an annealing temperature of 64.5°C for 30s, elongation at 72°C for 30 s for 30 cycles and a final extension at 72°C for 2 min in a T100 thermocycler (BioRad), as shown in Table 3.8. PCR products were maintained at 4°C prior to performing gel electrophoresis.

To visualize PCR fragments and sizes, agarose gel electrophoresis was performed using a 1.0% agarose gel (Appendix A). To visualize PCR amplified products, 5 μL of SYBR Safe DNA Gel Stain (Thermo Scientific) was added to the agarose solution and mixed by shaking gently before casting. The gel was poured into a gel casting apparatus and allowed to set. Next, the gel was placed in an electrophoresis tank filled with 1× TAE buffer (Appendix A). 5 μL of O'GeneRuler 1 kb Plus DNA Ladder (Thermo Scientific) was loaded into one well of the gel and 5 μL of each PCR product was mixed with 1 μL of 6× DNA loading dye (Thermo Scientific) and loaded in the remaining wells. Gel electrophoresis was performed for ~30 min at 100 V and bands were visualized and imaged using ultraviolet light on a MyECL imager (Thermo Scientific).

Table 3.7. Setup 50 μL PCR Reaction Mix for Q5 High-Fidelity Polymerase Chain Reaction

Component	Volume (μL)	Final Concentration
5× Q5 Reaction Buffer	10	1×
10 mM dNTPs	1	200 μM
10 μM Forward Primer	2.5	0.5 μM
10 μM Reverse Primer	2.5	0.5 μM
2 U/μL Q5 High-Fidelity DNA Polymerase	0.5	0.02 U/μL
Template DNA	volume ~ 100 ng	5 ng/μL
Nuclease-Free Water	to 50 μL	

Table 3.8. Thermocycling Conditions for Q5 High-Fidelity Polymerase Chain Reaction.

Step	Temperature (°C)	Time (s)	Number of Cycles
Initial Denaturation	98.0	30	1
Denaturation	98.0	10	30
Annealing	64.5	30	
Extension	72.0	30	
Final Extension	72.0	120	1
Hold	10.0		

3.7.7. DNA Sequencing of Potential *RBX1*$^{+/-}$ FT Clones

After confirming amplification of the targeted region of *RBX1* via gel electrophoresis, the PCR products (unpurified) were sent for DNA sequencing at McGill University and Génome Québec Innovation Centre (Montreal, Canada). All samples and primers (Table 3.6) were prepared and shipped after following the requirements specified by the facility. Bidirectional DNA sequencing (i.e. forward and reverse directions) was performed.

To determine the nature of the resulting CRISPR-mediated edits, an online software CRISP-ID (http://crispid.gbiomed.kuleuven.be) was employed. The chromatogram sequences were downloaded from the DNA Sequencing web portal and uploaded to the CRISP-ID website (http://crispid.gbiomed.kuleuven.be). This web-based application compares query sequences (e.g. sequenced PCR products of FT246 clones) and aligns them to a reference sequence (e.g. wild-type *RBX1* sequence), thus allowing for the detection of the exact insertions or deletions (indels) size and location of a CRISPR-Cas9 targeted region. Initial *RBX1*$^{+/-}$ clones were identified using this tool with further validation performed by subcloning each allele, and subsequent DNA sequencing.

3.7.8. Validation of *RBX1*-Edited Clones by Subcloning

To validate potential *RBX1*$^{+/-}$ clones identified from the first round of DNA sequencing, allele-specific subcloning was performed. Briefly, the DNA from each candidate *RBX1*$^{+/-}$ clone was PCR-amplified as above (Section 3.7.6.), purified using a QIAquick PCR Purification Kit (Qiagen) and the DNA concentration was determined. Finally, an In-Fusion HD Cloning Kit (Clontech) was employed to clone the purified PCR product according to manufacturer's protocol. Briefly, 50 ng of pUC19 linearized cloning vector was mixed with 4 μL of 5× In-Fusion HD Enzyme Premix and 50 ng of purified PCR product in a 1.5 mL microcentrifuge tube. Final volume was made up to 20 μL with Molecular Biology Grade water (HyClone). The In-Fusion cloning mix was incubated for 15 min at 50°C and transferred to ice. To transform bacteria, 2.5 μL of the In-Fusion cloning mix was added to 50 μL of Stellar Competent *Escherichia coli* (*E. Coli*) (Clontech) in a 1.5 mL microcentifuge tube. Tubes were incubated on ice for 30 min, followed by heat shock treatment in a water bath at 42°C for 60 sec, and finally incubation on ice for 2 min. Next, the tubes were topped up with pre-warmed (at 37°C) Super Optimal broth with Catabolite repression (SOC) medium (Takaro Bio) to a total volume of 500 μL. The tubes were incubated at 37°C for 1 h with gentle shaking. A control tube consisting of purified pUC19 (without PCR product) was included. Following incubation, the transformants were diluted (1:10 and 1:100 dilution ratios) in SOC media. For each dilution, 100 μL was plated on Luria-Bertani (LB) agar petri dishes with added carbenicillin (60 μg/mL) (Appendix A). Plates were incubated overnight in a 37°C in a bacterial incubator with moderate shaking. Following overnight incubation, colonies were picked and inoculated in 15 mL of LB broth containing carbenicillin (60 μg/mL) (Appendix A) and incubated overnight at 37°C with moderate shaking. A QIAprep Spin Miniprep kit (Qiagen) was employed according to the manufacturer protocol (Qiagen) to extract DNA from the amplified

plasmids. A Nano-Drop spectrophotometer (Thermo Scientific) was used to determine DNA concentration and purity. Colony PCR was performed to confirm the successful integration of a single PCR amplified fragment as detailed in Section 3.7.6. A total of six sub-clones for each putative *RBX1*$^{+/-}$ were sent for DNA sequencing and were analysed as detailed in Section 3.7.7 to validate the specific edits in the clones.

3.8. Cellular Phenotyping of *RBX1*$^{+/-}$ FT Clones

Following validation of the FT246 *RBX1*$^{+/-}$ clones by DNA sequencing, additional phenotyping was performed to determine growth rates using an xCELLigence Real-Time Cell Analyses (RTCA) Dual Plate (DP) instrument. In addition, cellular transformation was assessed using microsphere formation assays and standard colony formation assays in soft agar.

3.8.1. Real-Time Cellular Analyses (RTCA)

RTCA was performed in triplicate to assess the proliferation rates of FT246 *RBX1*$^{+/-}$ clones relative to control (NTgRNA) using an RTCA-DP (Acea Biosciences) apparatus, maintained in a 37°C incubator. The RTCA-DP uses microelectrodes at the bottom of each well to monitor changes in electrical impedance (called cell index) that is indicative of changes in cell numbers. Conceptually, increases in cell numbers is reflected by increases in electrical impedance and is reflected by increases in cell index. To perform the RTCA assay, 2000 cells/well were seeded into an E-plate (Acea Biosciences) and growth was monitored every 15 min for 7 days. All data were imported into Prism v6.0 (GraphPad) where growth curves were plotted for each Clone and compared with control. Graphs were imported into Photoshop CS6 where figure panels were assembled.

3.8.2. Colony Formation Assay in Soft Agar

The colony formation assay was performed by employing a double-layer approach which prevents cells from attaching and growing at the bottom of culture dishes. Briefly, a base layer of 0.6% agar (Appendix A) was prepared and poured into wells of 6-well plates. The agar was allowed to solidify prior to seeding cells. Next, cells were processed and counted as described in Sections 3.2.1 and 3.2.2. Cells were resuspended in appropriate volumes of pre-warmed 2× media (Appendix A) at 37°C, to obtain a final density of 50,000 cells per well. Next, an equal volume of 0.8% agar (Appendix A) was added to the cells to give a final agarose concentration of 0.4% and mixed carefully. The mixture was quickly plated into the wells of 6-well plates containing the base layer of 0.6% agar (Appendix A). To prevent the agar from solidifying in tubes or while handling in the pipettes, all reagents were maintained at minimum 37°C by keeping tubes in a hot water bath and adjusting the temperature with hot water whenever required. After seeding, the agar was allowed to solidify in the hood for ~30 min. Next, each well was supplemented with 2 mL of pre-warmed 1× medium to prevent desiccation. The plates were incubated at 37°C in a humidified incubator for six weeks and the medium was changed once a week. After six weeks, the medium was aspirated and the colonies were fixed with 4% paraformaldehyde (20 min). For visualization purposes, colonies were stained with 0.005% crystal violet (Sigma) (Appendix A) for 30 min, following which, wells were rinsed three times with Milli-Q water, replenished with ~1 mL of Milli-Q water to prevent desiccation and stored at 4°C. The following day, images were acquired using a Cytation 3 Cell Imaging Multi-Mode Reader (Bio-Tek) microscope equipped with a 4× objective. GEN5 software was used to automatically determine the number of colonies exceeding 100 μm in diameter. Finally, all data were imported to Prism v6.0 (GraphPad), where statistical

analyses (Section 3.9) were performed and graphs were generated. Graphs were imported into Photoshop CS6 which was used to assemble figure panels.

3.9. Statistical Analyses Performed in this Study

Statistical analyses performed in this thesis include Kolmogorov-Smirnov (KS) and Mann-Whitney tests. The statistical analyses were performed to identify significant differences between experimental values and controls. Analyses were carried out in Prism v6.0 (GraphPad). Two sample KS tests were utilised to assess whether differences in cumulative distribution frequencies (e.g. NAs, chromosome numbers) between values from experimental samples were statistically different from controls. For MNF analyses, Mann-Whitney tests were employed to test whether differences in MNF between experimental and control conditions were significant. For reference purposes, *p*-values of < 0.05 were deemed statistically significant. The numbers of biological (N) and technical (n) replicates are indicated for all data presented within this thesis. In cases where $N > 1$, results from one representative biological replicate are given.

CHAPTER 4: RESULTS

4.1. Aim 1: To Evaluate the Impact Diminished *RBX1* Expression has on Cyclin E1 Levels and CIN

In order to evaluate the effects of diminished *RBX1* expression on CIN, transient, siRNA-based silencing was employed to reduce *RBX1* expression in three karyotypically stable cell lines, HCT116, FT194 and FT246 (Table 3.1). As previously described in Chapter 1, HCT116 is a human colorectal carcinoma cell line with a modal number of 45 chromosomes, while FT194 and FT246 are human immortalized secretory epithelial fallopian tube cell lines each having a modal chromosome number of 46. After establishing *RBX1* silencing efficiency in each line, various CIN-associated phenotypes including changes in NA, MNF and chromosome numbers were quantitively assessed.

4.1.1. Evaluating *RBX1* Silencing Efficiency in HCT116, FT194 and FT246

Prior to determining the impact diminished *RBX1* expression has on CIN, the silencing efficiencies of four individual (si*RBX1*-1, -2, -3, -4) and pooled (si*RBX1*-Pool) siRNA duplexes were assessed by western blots. Semi-quantitative analyses were performed by normalizing the signal intensities of RBX1 bands to their corresponding loading controls (Cyclophilin B) and are presented relative to the negative control (Non-targeting). As illustrated in Figure 4.1A, *RBX1* silencing by both individual and pooled siRNA approaches was highly efficient, with expression levels being reduced to ~9-20% of control (Non-targeting) levels in HCT116 cells. The silencing experiments were expanded into FT194 and FT246 with similar, albeit slightly less efficient silencing; HCT116 (4-5% of control levels), FT194 (18-24%) and FT246 (9-16%). Accordingly, the two most efficient siRNAs (si*RBX1*-2 and si*RBX1*-4) along with the pooled siRNA were employed in subsequent experiments **(**Figure 4.1B).

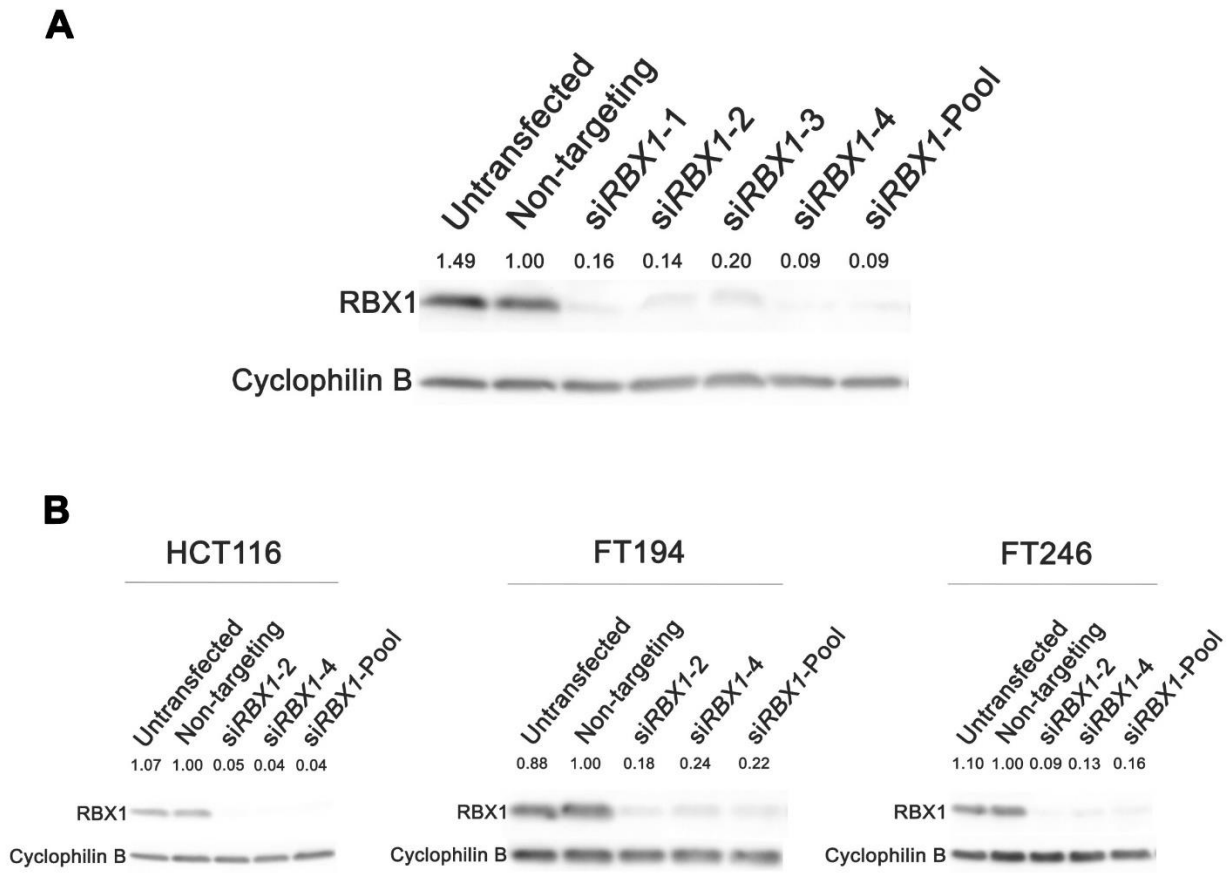

Figure 4.1. Evaluating *RBX1* silencing efficiency in HCT116, FT194 and FT246 cells.
(A) Western blot showing silencing efficiencies of 4 individual and the pooled siRNAs targeting *RBX1*, relative to the control (non-targeting siRNA) in HCT116 cells. Proteins were harvested 4 days post-transfection. Cyclophilin B serves as a loading control. Semi-quantitative analyses were performed, whereby RBX1 levels were normalized to the corresponding loading control and are presented relative to control (non-targeting). The two most efficient silencing duplexes (si*RBX1*-2 and si*RBX1*-4) along with si*RBX1*-Pool were selected for subsequent experiments. ***(B)*** Representative western blots showing the silencing efficiency of the two most effective individual and pooled siRNAs in HCT116 (N=3), FT194 (N=3) and FT246 (N=3), relative to control (non-targeting). Cyclophilin B serves as a loading control.

4.1.2. Reduced *RBX1* Expression underlies Increases in Cyclin E1 levels and NAs in HCT116 and FT246 cells

Genomic amplification of *CCNE1* induces CIN[95] and is an early driver of oncogenesis in several cancers, including HGSOC[94] (Section 1.3, Page 14). The protein levels of Cyclin E1 are tightly controlled by the SCF complex which includes RBX1 as a critical component imparting the catalytic activity of the complex. Recall that >80% of HGSOCs show heterozygous loss of *RBX1*, suggesting diminished *RBX1* expression may induce CIN, potentially via mis-regulation of Cyclin E1 levels. The effect of diminished *RBX1* expression on Cyclin E1 levels has never been investigated. Therefore, after establishing the optimal silencing conditions, I evaluated the impact diminished *RBX1* expression has on Cyclin E1 levels and CIN in the three cell lines employed within this study. Following *RBX1* silencing, Cyclin E1 levels were assessed by western blots and scQuantIM was employed to detect changes in phenotypes associated with CIN such as changes in NAs. As shown in Figure 4.2A, *RBX1* silencing in HCT116 corresponded with ~2-3-fold increases in Cyclin E1 levels. In addition, *RBX1* silencing also resulted in visually apparent increases in NAs (Figure 4.2B) and overall increases in the cumulative NA distribution frequencies as evidenced by rightward shifts relative to control (Figure 4.2C). Subsequent KS tests revealed that the increases in NA distributions were all statistically significant (p-value < 0.0001) relative to the controls. Within the FT194 cell populations, no increases in Cyclin E1 levels were observed following *RBX1* knock-down. However, increases in NAs were equally observed in *RBX1*-silenced FT194 cells relative to controls, as shown in Figure 4.3. The increases were deemed highly statistically significant by KS tests (p-value < 0.0001). Similar trends to HCT116 were observed following *RBX1* silencing in FT246 as illustrated in Figure 4.4. The increases in Cyclin E1 levels were not as pronounced as those observed in HCT116. Likewise, the cumulative NA

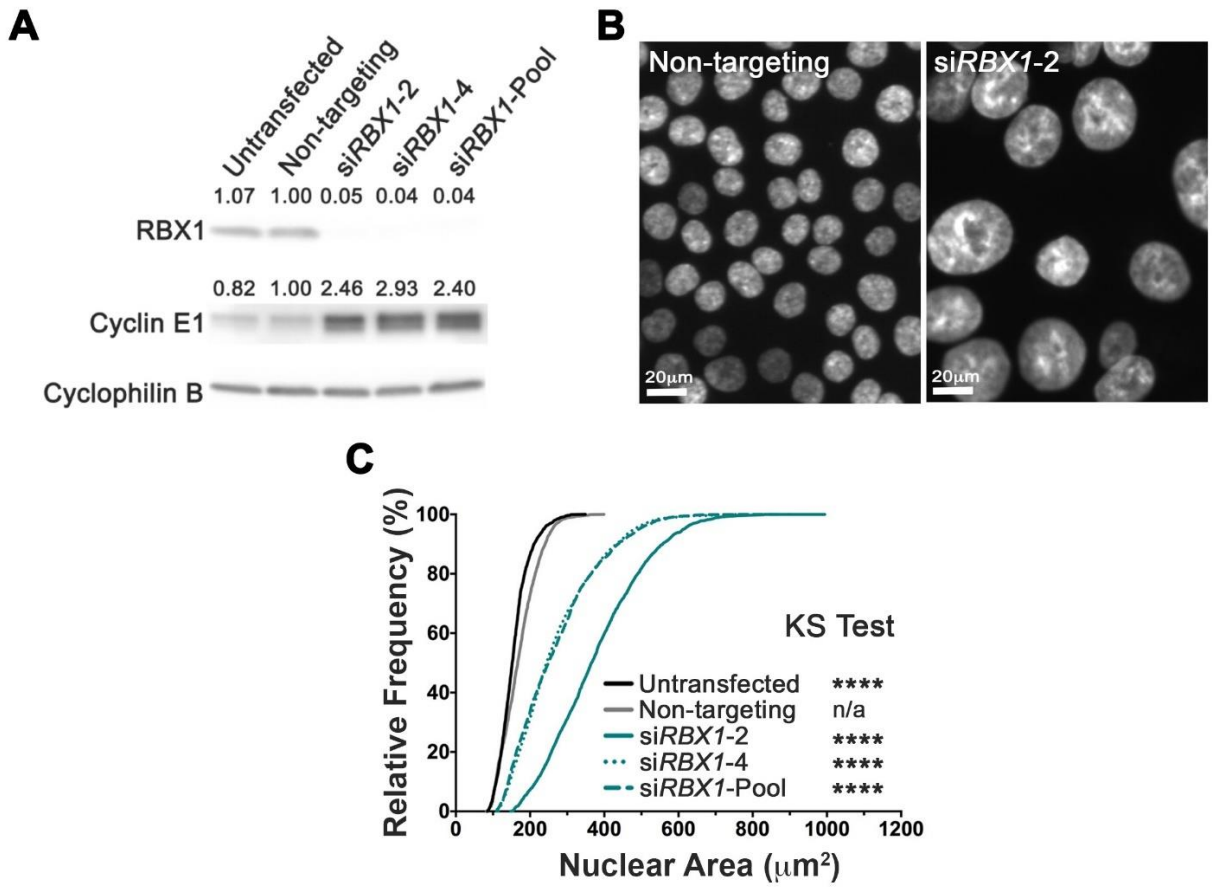

Figure 4.2. *RBX1* silencing induces increases in Cyclin E1 and NAs in HCT116 cells.
(A) Semi-quantitative western blot showing increases in Cyclin E1 protein levels following *RBX1* silencing relative to control (non-targeting); Cyclophilin B is the loading control. ***(B)*** Representative low-resolution micrographs of Hoechst-labelled nuclei presenting visual increases in NAs associated with *RBX1* silencing. Note the scale bars are identical in both images. ***(C)*** Cumulative NA frequency distributions reveal statistically significant increases (i.e. rightward shift) following *RBX1* silencing relative to control (N=3, >2000 nuclei per condition). KS-tests were employed for statistical comparisons of cumulative distribution frequencies, n/a, not applicable; ns, not significant; ****, *p*-value <0.0001.

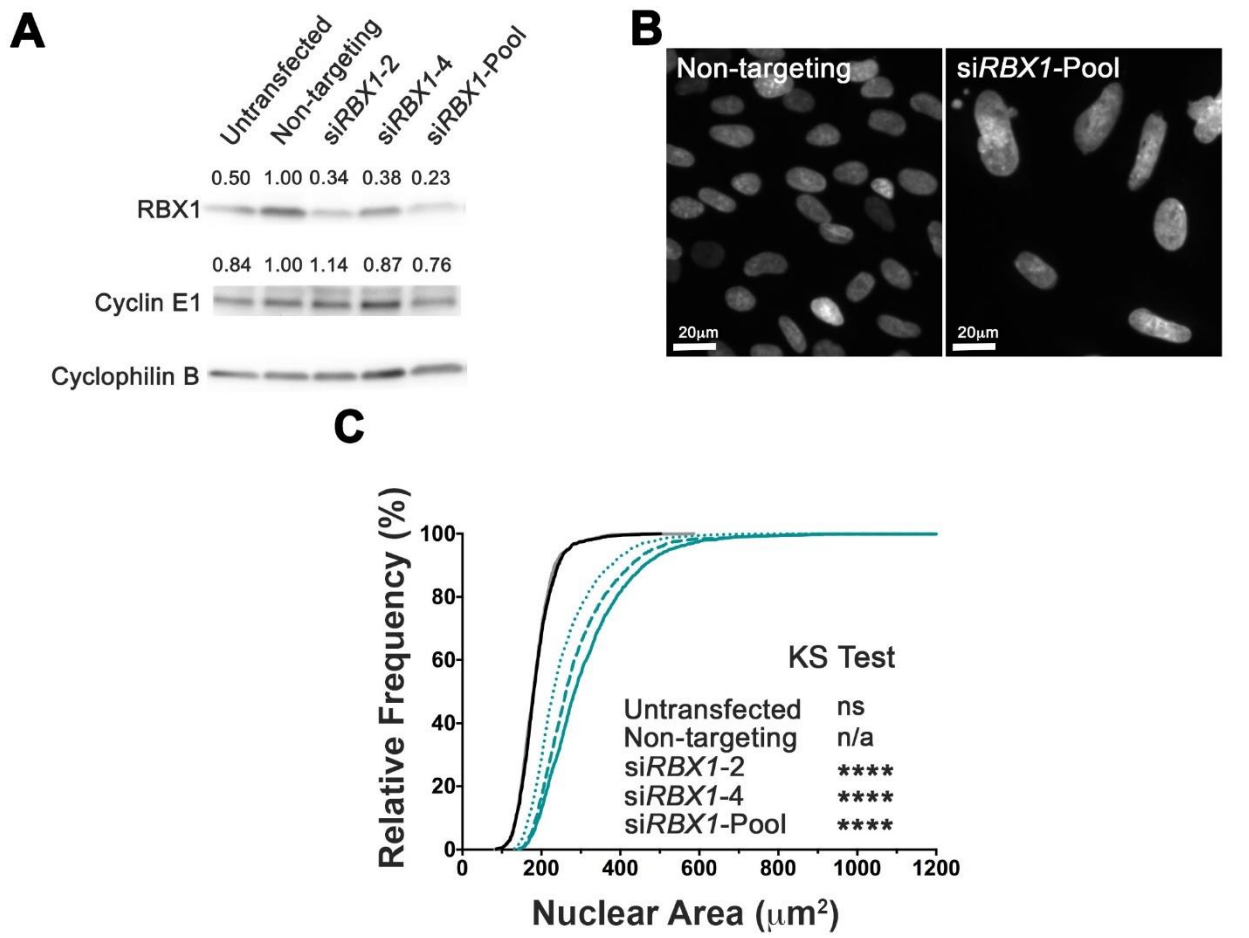

Figure 4.3. *RBX1* silencing induces increases in NAs in FT194 cells.
(A) Semi-quantitative western blot showing no change in Cyclin E1 levels following *RBX1* silencing relative to control; Cyclophilin B is the loading control. ***(B)*** Representative low-resolution micrographs of Hoechst-labelled nuclei presenting visual increases in NAs following *RBX1* silencing. Scale bars are identical. ***(C)*** Cumulative NA frequency distributions reveal statistically significant increases in NA following silencing relative to control (N=3, >1800 nuclei analysed per condition). KS-tests were employed for statistical comparisons of cumulative distribution frequencies, n/a, not applicable; ns, not significant; ****, *p*-value <0.0001.

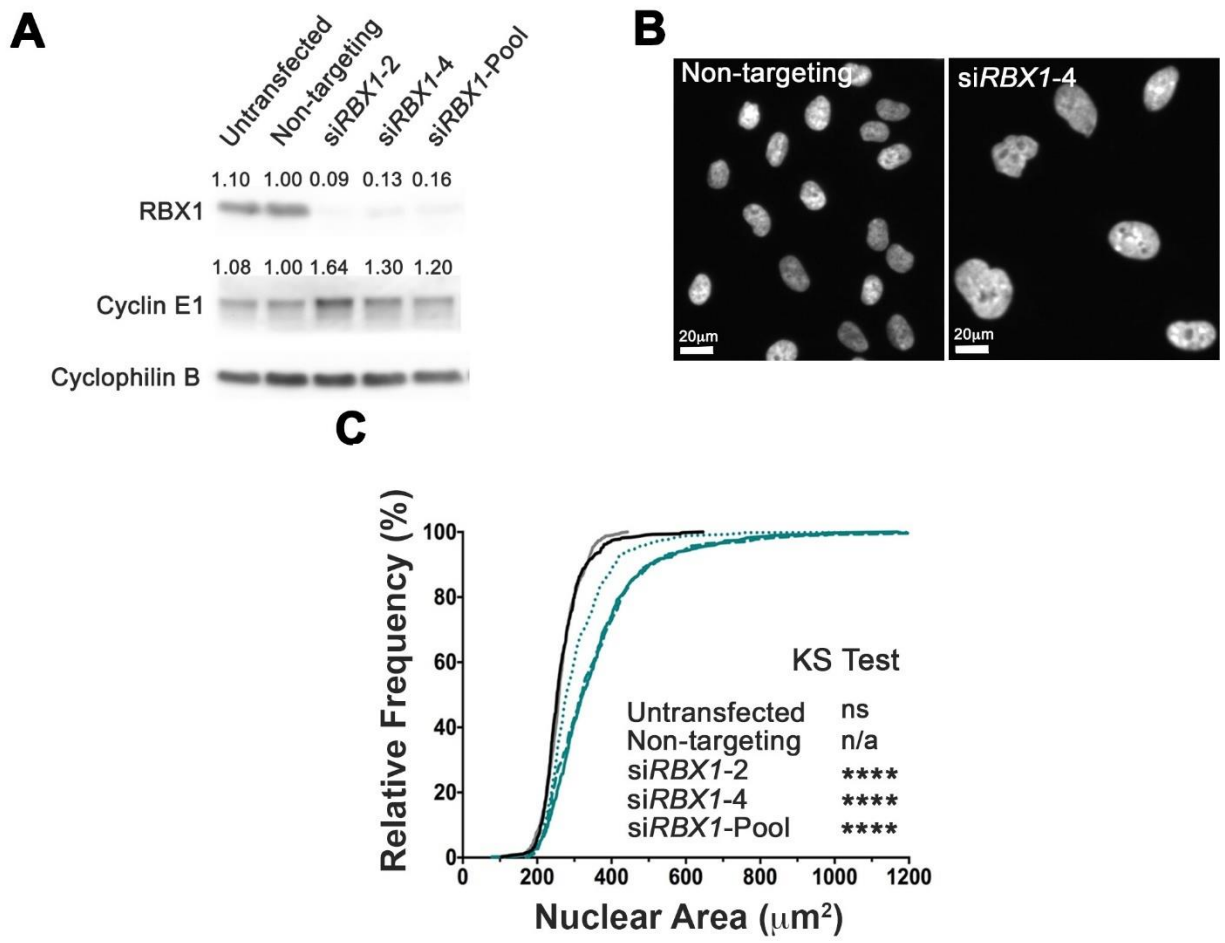

Figure 4.4. *RBX1* silencing induces increases in Cyclin E1 and NAs in FT246 cells.
(A) Semi-quantitative western blot showing increases in Cyclin E1 levels following silencing; Cyclophilin B is the loading control. ***(B)*** Representative low-resolution micrographs of Hoechst-labelled nuclei showing visual increases in NAs following silencing. Scale bars are identical. ***(C)*** Cumulative NA frequency distributions reveal statistically significant increases in NA following silencing (N=3, >500 nuclei analysed per condition). KS-tests were employed for statistical comparisons of cumulative distribution frequencies, n/a, not applicable; ns, not significant; ****, *p*-value <0.0001.

distribution frequency for all *RBX1*-silenced conditions were increased relative to controls. In addition, KS tests revealed that the increases in NAs in the *RBX1*-silenced conditions relative to the negative control were statistically significant (*p*-value < 0.0001). In general, these data show that *RBX1* silencing correlates with aberrant increases in Cyclin E1 levels, particularly in HCT116 and FT246 and reduced *RBX1* expression reproducibly results in overall increases in NAs within all the three cellular contexts.

4.1.3. Increases in MNF Correspond with Decreased *RBX1* Expression in HCT116, FT194 and FT246 Cells

Having established that *RBX1* silencing induces increases in NAs, I wanted to evaluate its impact on MNF, an established hallmark of CIN[129]. Recall that micronuclei are small extra-nuclear bodies containing whole and/or large chromosomal fragments, and thus serve as a surrogate marker for CIN.

To quantify changes in MNF following *RBX1* silencing, scQuantIM was employed as detailed within Materials and Methods (Section 3.5, Page 42). Briefly, micronuclei were enumerated from a minimum of 500 interphase nuclei/condition and the change in MNF relative to the control (set to 1) was determined (Figure 4.5). In HCT116, a statistically significant ~3- to 5-fold increase (Mann-Whitney test) in the number of micronuclei was observed within the *RBX1*-silenced populations, relative to the control. MNF was also assessed within FT194 and FT246 cells. Similar to HCT116 cells, *RBX1* silencing induced significant increases in MNF within both cell lines. Interestingly, the overall increases in MNF observed following *RBX1* silencing were smaller (~1.5 to ~2-fold increase) in FT194 than that observed within the HCT116 cells or FT246 cells (~3 to ~6-fold increase). In general, the increases in MNF in the FT cell lines were also deemed statistically significant by Mann-Whitney tests. Collectively, these data show that *RBX1*

silencing corresponds with increases in MNF in HCT116, FT194 and FT246 cells, thus indicating that diminished *RBX1* expression induces CIN within these three cellular contexts.

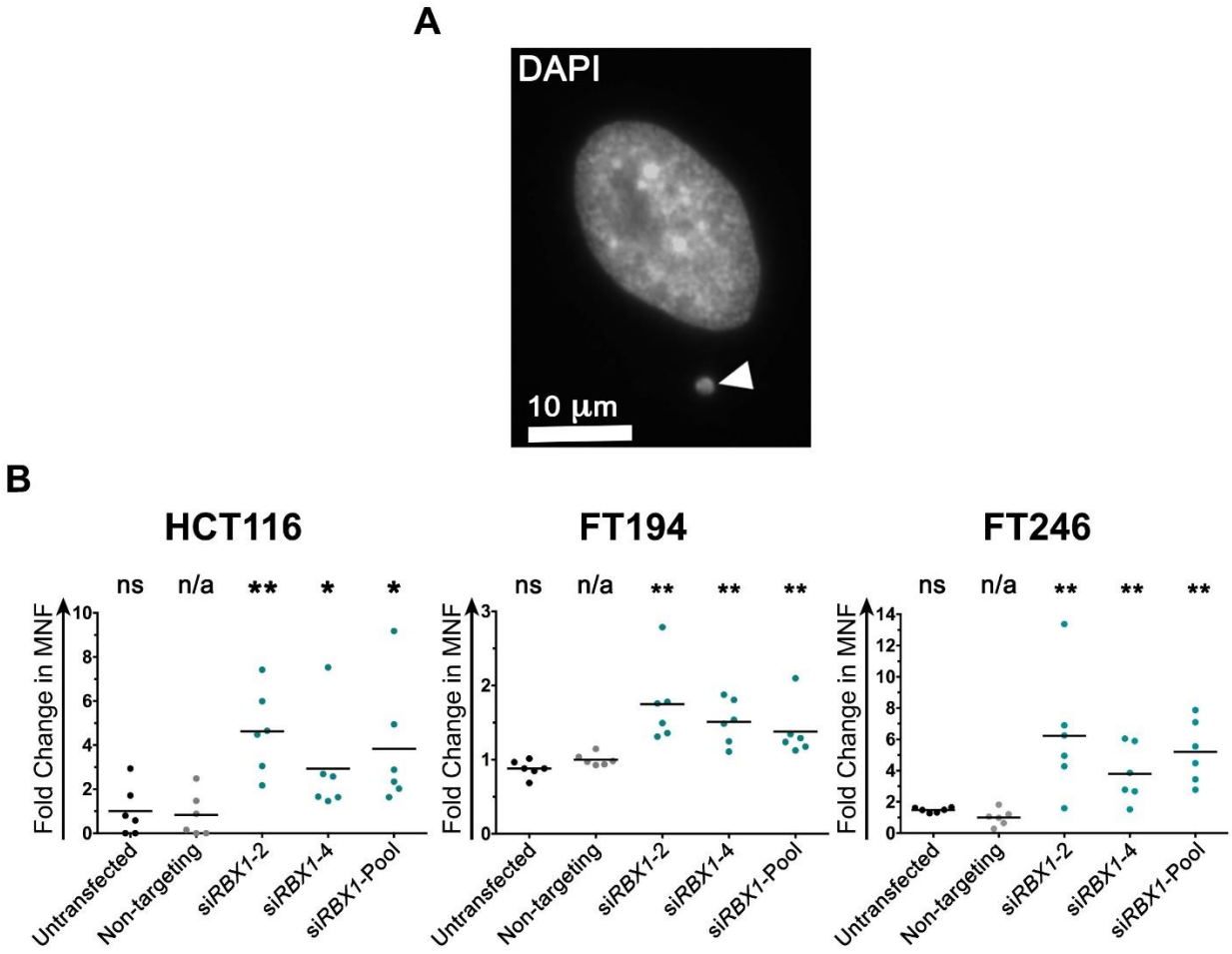

Figure 4.5. *RBX1* silencing induces increases in MNF in HCT116, FT194 and FT246 cells. ***(A)*** Representative high-resolution image (63x) of *RBX1*-silenced FT246 nucleus displaying a micronucleus (arrowhead). ***(B)*** Dot plots presenting the fold change in MNF relative to the mean of control in HCT116, FT194 and FT246. Black bar indicates the mean fold change in MNF of 6 replicate wells. (N=3, n=6 >600 nuclei/condition). Mann-Whitney test; n/a, not applicable; ns, not significant; *, *p*-value <0.05; **, *p*-value <0.01. Fold increase presented relative to non-targeting.

4.1.4. *RBX1* Silencing Drives Changes in Chromosome Numbers in HCT116, FT194 and FT246 Cells

After determining that *RBX1* silencing underlies increases in CIN-associated phenotypes such as NAs and MNF, we wished to determine whether the changes observed are associated with alterations in chromosome numbers. Accordingly, mitotic chromosome spreads were generated following *RBX1* silencing as detailed in Materials and Methods (Section 3.6, Page 43) and a minimum of 100 spreads/condition were manually assessed for changes in chromosome numbers. In HCT116, RBX*1* silencing resulted in changes in chromosome numbers (i.e. having deviations from the modal number of 45 chromosomes) as well as dramatic increases in decondensed/decompacted chromosomes as illustrated in Figure 4.6A. The decondensed phenotype was exclusively observed in the HCT116 cells at a striking frequency of > 50% of the *RBX1*-silenced mitotic spreads. Chromosome losses (<45 chromosomes) were the second most frequent aberration, observed in 16-27% of spreads in the *RBX1*-silenced cells, relative to control. Small- and large-scale gains were the least prevalent type of aberration in HCT116, observed in ~1-8% and ~1-2% of *RBX1*-silenced conditions, respectively. The differences in cumulative distribution frequency of chromosome numbers between *RBX1*-silenced cells and controls were deemed statistically significant (p-value < 0.0001) by KS tests (Table S7).

In FT194, following *RBX1* silencing, deviations from the modal chromosome number (46 chromosomes) were also observed as shown in Figure 4.7. Detailed analysis of the aberrant spreads in *RBX1*-silenced cells revealed that the most frequent aberration was the small-scale gain (47-59 chromosomes), observed at a frequency of ~32-35%, followed by large-scale gain of chromosomes (>59 chromosomes), accounting for ~ 6-22%

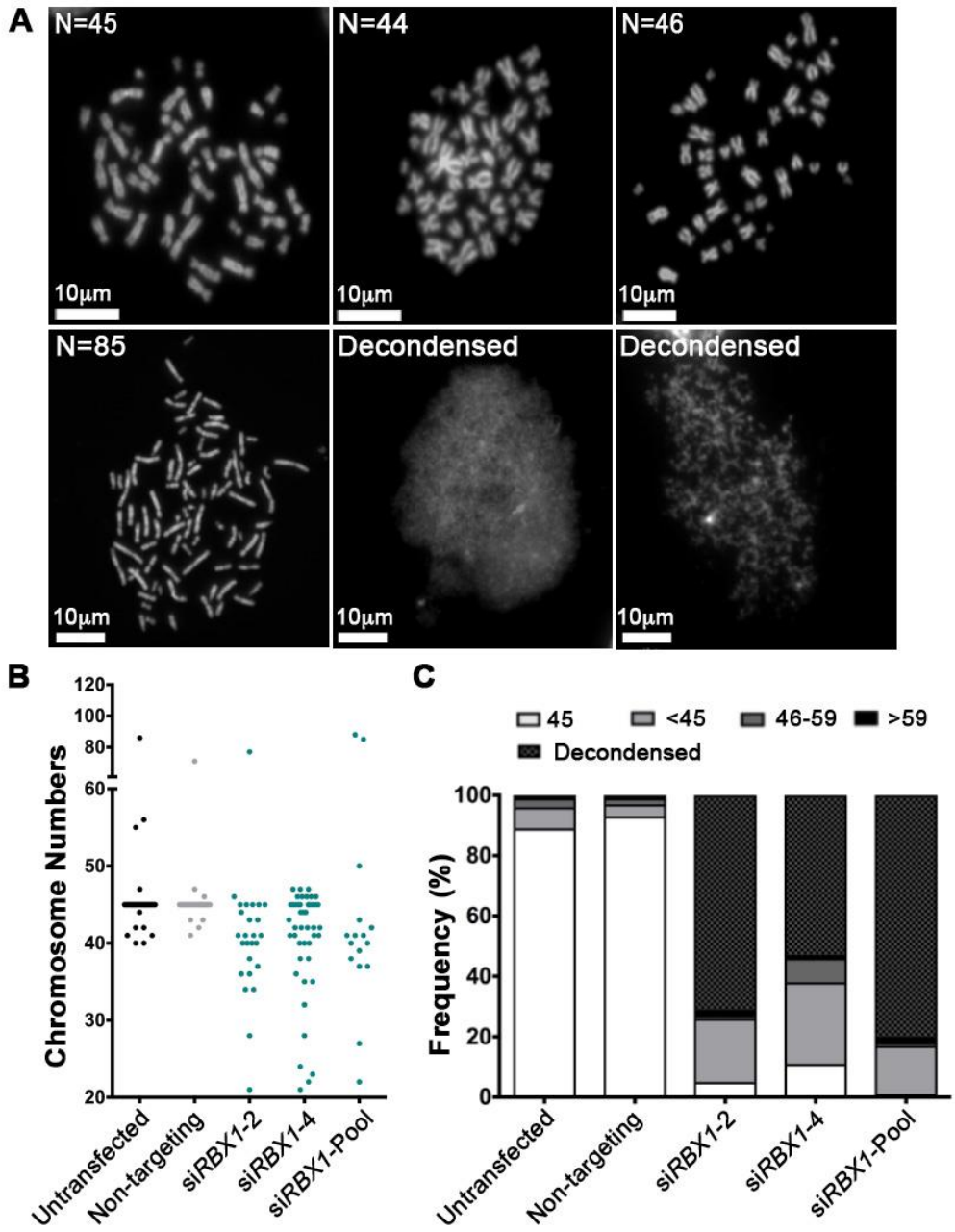

Figure 4.6. *RBX1* silencing induces changes in chromosome numbers and condensation defects in HCT116 cells.

(A) Representative high resolution 2D images (63x) of mitotic chromosome spreads from HCT116, 4 days post-silencing, displaying the modal number of 45 chromosomes (top left), chromosome losses (top middle), small-scale gains (top right), large-scale gains (bottom left) and condensation/compaction defects (bottom middle and right). ***(B)*** Dot plot displaying the number of chromosomes enumerated from *RBX1*-silenced conditions (N=1, >100 spreads/condition) and controls. ***(C)*** Bar graph depicting the distribution of mitotic spreads between five categories; normal (45 chromosomes); chromosome loss (<45); small-scale gain (46 to 59) and large-scale gain (>59).

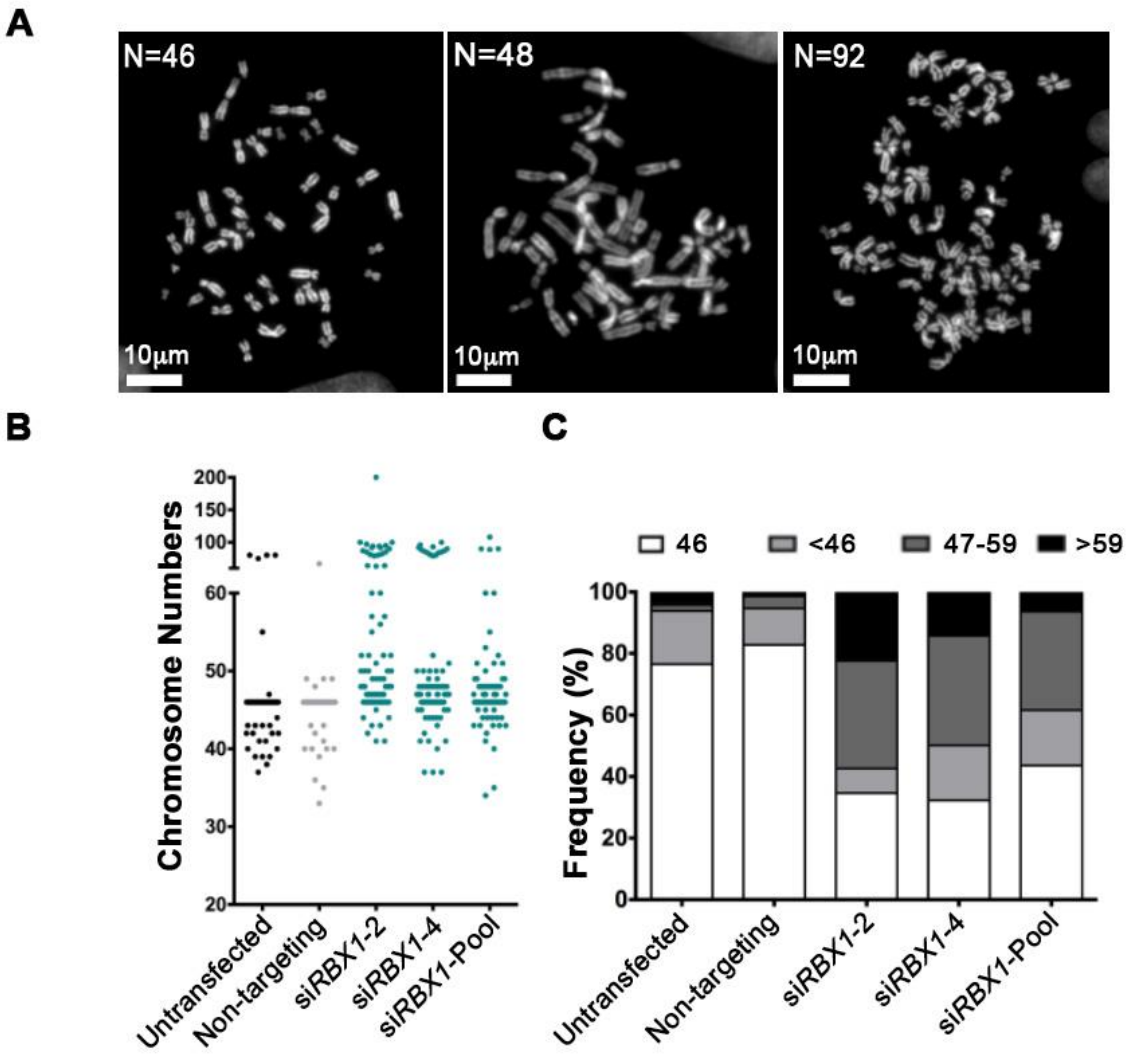

Figure 4.7. *RBX1* silencing induces changes in chromosome numbers in FT194 cells.
(A) Representative high resolution 2D images (63x) of mitotic chromosome spreads from FT194, 4 days post-silencing, displaying modal number of 46 chromosomes (left), chromosome losses (middle) and large-scale gains (right). ***(B)*** Dot plot displaying the number of chromosomes enumerated from each spread (N=2, >100 spreads/condition). ***(C)*** Bar graph depicting the distribution of mitotic spreads between four categories; normal (46 chromosomes); chromosome loss (<46); small-scale gain (47 to 59) and large-scale gain (>59).

of aberrant spreads and chromosome losses (<46 chromosomes), occurring in 8-18% of mitotic spreads. Cumulative distribution frequencies for chromosome numbers of all the *RBX1*-silenced conditions were significantly different (p-value < 0.0001) from the control, as revealed by KS tests (Table S8). Similarly, mitotic chromosome spread enumeration in FT246 (Figure 4.8) showed that *RBX1* silencing resulted in changes in chromosome numbers. However, chromosome losses were the most common aberration upon *RBX1*-silencing (observed at a frequency of ~28-65%), followed by small-scale gains (~8-21%) and large-scale gains of chromosomes (~2-6%). Differences in cumulative distribution frequencies of chromosome numbers between *RBX1*-silenced conditions and control were found to be statistically significant by KS tests (p-value < 0.0001 for si*RBX1*-2, p-value < 0.001 for si*RBX1*-4 and p-value < 0.05 for si*RBX1*-Pool.

Overall, the findings obtained from this aim of the thesis showed that silencing *RBX1* in HCT116, FT194 and FT246 induces significant increases in NAs (Section 4.1.2), MNF (Section 4.1.3) as well as aberrant chromosome numbers (Section 4.1.4). Thus, taken together, these data identify *RBX1* as a novel CIN gene, independent of cellular context.

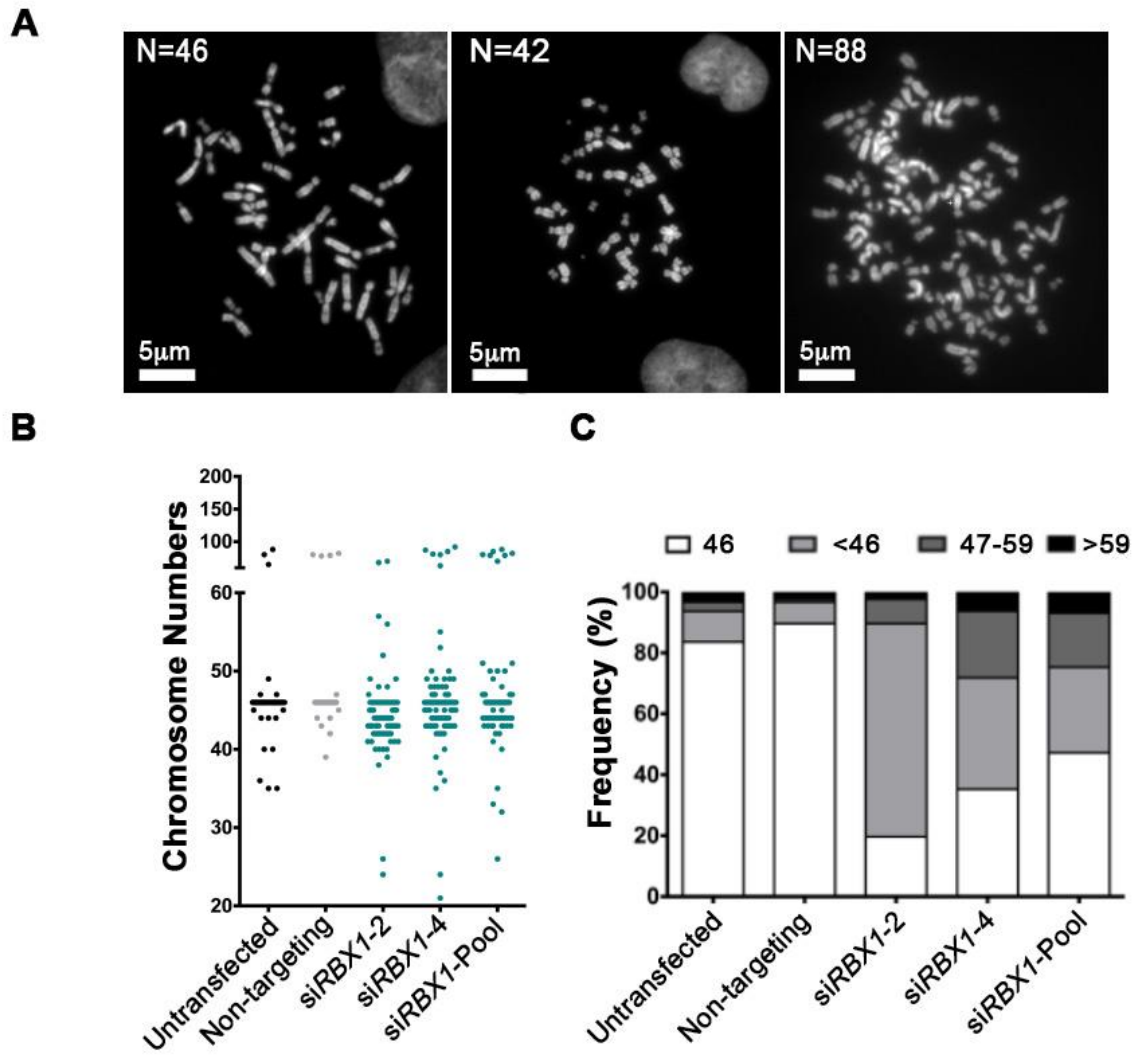

Figure 4.8. *RBX1* silencing induces changes in chromosome numbers in FT246 cells.
(A) Representative high resolution 2D images (63x) of mitotic chromosome spreads from FT246, 6 days post-silencing, displaying modal number of 46 chromosomes (left), chromosome losses (middle) and gains (right). ***(B)*** Dot plot displaying the number of chromosomes from each chromosome spread analysed (N=2, >100 spreads/condition). ***(C)*** Bar graph depicting the distribution of mitotic spreads between four categories; normal (46 chromosomes); chromosome loss (<46); small-scale gain (47 to 59) and large-scale gain (>59).

4.2. Aim 2: To Evaluate the Impact Heterozygous Loss of *RBX1* (*RBX1*$^{+/-}$) has on Cyclin E1 Levels, CIN and Cellular Transformation

After identifying *RBX1* as a novel CIN gene, I next sought to determine the impact heterozygous loss of *RBX1* has on Cyclin E1 levels and CIN. Recall that heterozygous loss of *RBX1* occurs in ~83% of HGSOC cases[83], which suggests that diminished *RBX1* expression may contribute to the early events underlying the pathogenesis of HGSOC. Besides, homozygous loss of *RBX1* is a very rare phenomenon, occurring in less than 1% of HGSOC patients. In addition, studies in model organisms have reported orthologues of *RBX1* as essential genes in mice, yeast and flies, where homozygous loss induces lethality[141,145-148]. Altogether, these insights feature heterozygous loss of *RBX1* as a clinically more relevant model to study. Thus, in order to determine the impact heterozygous loss of *RBX1* has on Cyclin E1 levels and CIN, a CRISPR-Cas9 gene editing system was employed to generate stable *RBX1*$^{+/-}$ FT246 clonal cell populations (Section 3.7, Page 44). Two *RBX1*$^{+/-}$ FT246 clones were generated and further employed in a time-course experiment to evaluate CIN-associated phenotypes at regular intervals. Phenotypes associated with cellular transformation, such as anchorage-independent growth was also assessed in the *RBX1*$^{+/-}$ FT246 clones

4.2.1. Generation of *RBX1*$^{+/-}$ FT246 Clones

Briefly, FT246 cells were transduced with lentiviral particles containing a guide RNA (gRNA) targeting *RBX1* (or non-targeting [NTgRNA] for negative controls). Transduced cells constitutively expressing the gRNA along with BFP were subjected to FACS. Cells were expanded and transiently transfected with a Cas9 expression plasmid that co-expresses GFP. Successfully transfected cells expressing both GFP (transient Cas9 expression) and BFP (constitutive gRNA expression) were subjected to FACS. Next, a limiting dilution of the bulk sorted cells was

performed to generate clonal populations of CRISPR-mediated *RBX1*-edited FT246 cells. Forty-five individual clones were expanded and screened for potential *RBX1* editing by western blots (Supplementary Figure 1). Clones exhibiting reduced RBX1 protein levels were selected for further expansion and subsequent DNA sequencing. Importantly, some of the clones with reduced *RBX1* expression did not survive and thus, could not be pursued. To perform DNA sequencing, DNA was extracted from candidate FT246 clones harboring potential *RBX1* edits. PCR was employed to amplify the genomic region surrounding the gRNA recognition site (i.e., exon 2 of *RBX1*). Amplification of the *RBX1* targeted region was confirmed via DNA gel electrophoresis (Supplementary Figure 2). The PCR products (unpurified) were subjected to bidirectional DNA sequencing (i.e. forward and reverse directions) at the McGill DNA sequencing facility. Initial clones were identified and DNA sequences were analysed through CRISP-ID (http://crispid.gbiomed.kuleuven.be), an online resource that aligns queried sequences (e.g. sequenced PCR products of FT246 clones) to a reference sequence (e.g. wild-type *RBX1* sequence), thus enabling the detection of the indel size and location of a CRISPR-Cas9 targeted region. Collectively, this process identified two $RBX1^{+/-}$ clones which were subjected to subsequent validation by subcloning.

4.2.2. DNA Sequence Validation of the $RBX1^{+/-}$ FT246 Clones

To firmly establish the type and extent of the $RBX1^{+/-}$ edits, DNA was extracted from each clone and subsequently cloned to isolate individual alleles, with multiple clones subjected to DNA sequencing. Finally, the two $RBX1^{+/-}$ FT246 clones were validated and renamed Clone 1 and Clone 2 to represent Clones SG E5 and DG B7, respectively. As depicted in Figure 4.9A, Clone 1 harbors a 4 bp deletion in a single allele at the expected CRISPR edit site, located upstream of the NGG (N= any nucleotide base) recognition sequence, also called the protospacer adjacent motif (PAM)

site. Clone 2 contains a 52 bp deletion in a single allele at the expected CRISPR edit site. The edits in both clones are out of frame and they result in a frameshift mutation with the introduction of a premature stop codon early within Exon 2 (out of 5 exons) (Figure 4.9B).Since the premature stop codon is introduced upstream of the final exon-exon junction (> 55 bp upstream), nonsense-mediated mRNA decay (NMD) is essentially activated, resulting in the degradation of the mRNA. Therefore, no protein is expected to be produced from the edited allele, resulting in the heterozygous loss of *RBX1*. In line with this prediction, as shown in Figure 4.9C, Clone 1 and 2 have RBX1 levels reduced to ~42% and 57%, respectively, relative to control. Interestingly, increased Cyclin E1 levels were also observed in Clone 2. Taken together, these data validate the two $RBX1^{+/-}$ FT246 clones generated. Therefore, they can be employed in experiments to recapitulate heterozygous loss of *RBX1* in HGSOC, whereby its potential impact on CIN and cellular transformation can be assessed.

Figure 4.9. Identification and validation of *RBX1*$^{+/-}$ FT246 clones.
(A) DNA sequencing confirms single allele edits of *RBX1* in Clone 1 (top) and Clone 2 (bottom). Deletions (depicted in dashes) are at the expected CRISPR edit site located upstream of the protospacer adjacent motif (PAM; NGG) recognition sequence (blue font). The single allele edit in Clone 1 is a 4 bp deletion, whereas the single allele edit in Clone 2 is a 52 bp deletion. Both of the (out of frame) edits introduce a frameshift mutation which likely results in heterozygous loss of *RBX1*. ***(B)*** Resulting RBX1 protein sequences after CRISPR-mediated edits. Modified amino acids are depicted in color. Premature stop codon triggers NMD, therefore truncated protein shown is not produced. ***(C)*** Western blot showing diminished RBX1 levels in Clone 1 and Clone 2 in FT246 relative to control (NTgRNA); Cyclophilin B serves as a loading control. Both clones exhibit increases in Cyclin E1 levels, although they are more pronounced in Clone 2 (1.96-fold) than Clone 1 (1.21-fold).

4.2.3. Morphological and Growth Kinetic Characterization of *RBX1*$^{+/-}$ FT246 Clones

Bright field microscopy was employed to compare the cellular morphologies of the *RBX1*$^{+/-}$ FT246 clones to wildtype FT246 and the experimental control, NTgRNA (Figure 4.10). In general, *RBX1*$^{+/-}$ FT246 cells were morphologically similar to the wildtype and control cells.

RTCA was performed to determine the proliferation rates of the *RBX1*$^{+/-}$ FT246 clones relative to control. Briefly, RTCA monitors changes in electrical impedance (called cell index) that are indicative of changes in cell numbers. Conceptually, increases in cell numbers are reflected by increases in electrical impedance which correspond to increases in cell index. The assay was performed in triplicate and the average of the 3 technical replicates were plotted as single growth curves for each clone as well as control cells (Figure 4.11A). Doubling times were calculated from the linear portion of the exponential growth phase (~52 h to ~118 h) (Figure 4.11B). Mean doubling was found to be ~23 h for the control and Clone 2, and ~32 h for Clone 1. Student's *t*-tests did not reveal any statistically significant difference between the *RBX1*$^{+/-}$ FT246 clones and control cells. Collectively, these data show that the *RBX1*$^{+/-}$ FT246 clones are morphologically similar to the control cells and possess similar growth kinetic properties.

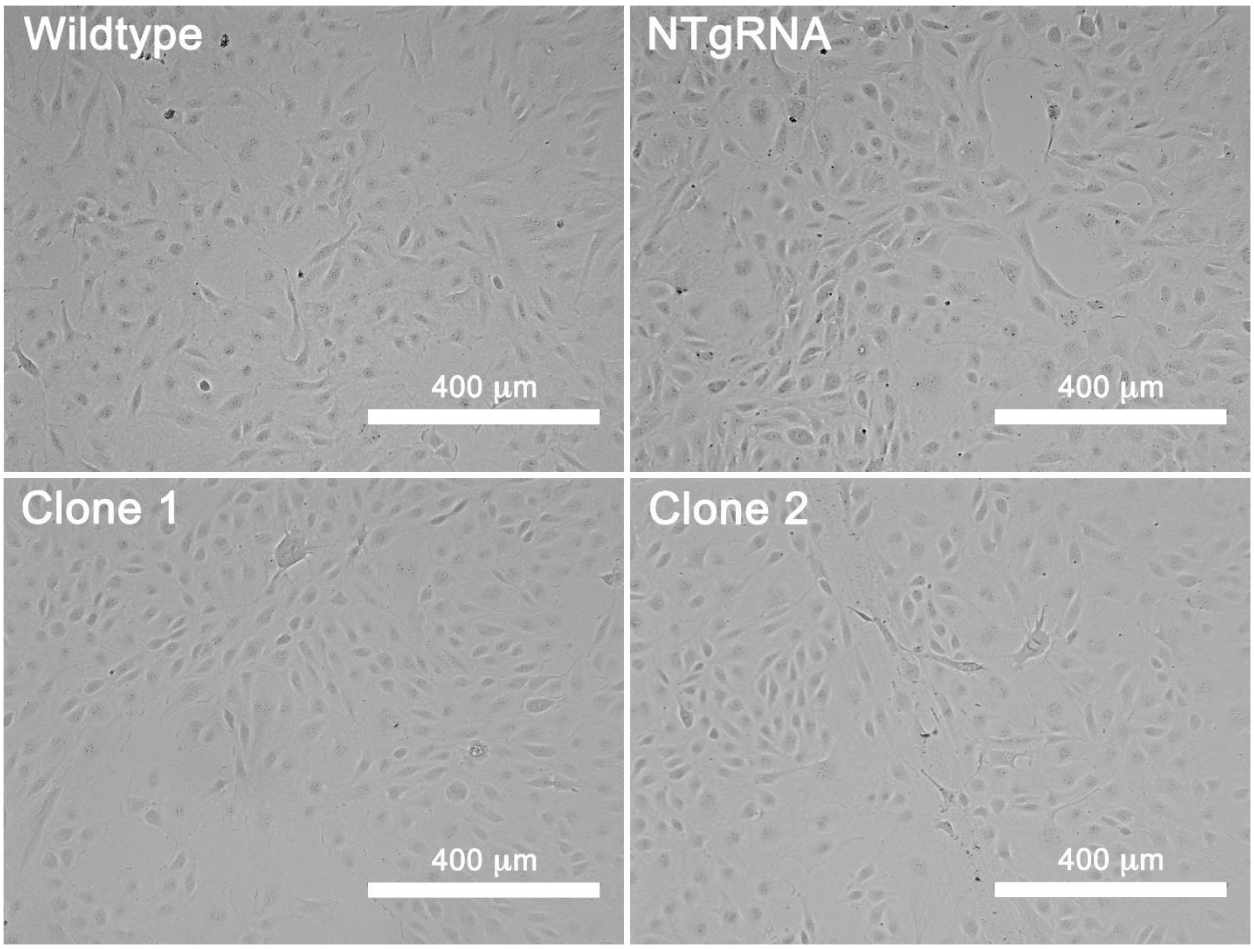

Figure 4.10. Cellular morphologies of Clone 1 and Clone 2 compared to wildtype and control cells.

Representative low-resolution (10×) bright field micrographs presenting cellular morphologies of wildtype FT246, control cell, Clone 1 and Clone 2. Clone 1 and 2 show similar cellular morphology as wildtype and control cells.

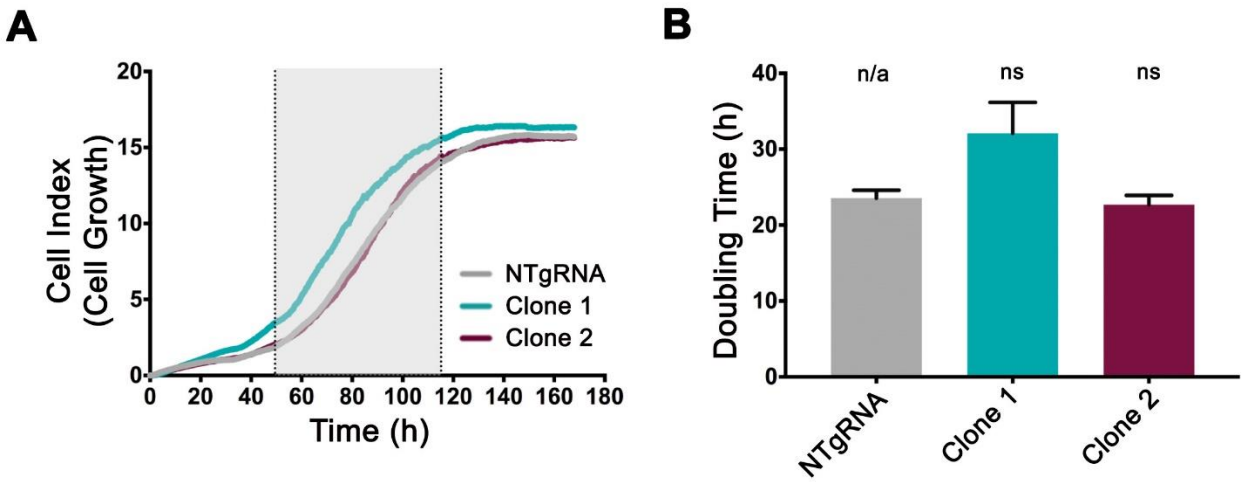

Figure 4.11. Growth kinetics of *RBX1*$^{+/-}$ FT246 clones are similar to control cells.
(A) Real-time growth curves of control (NTgRNA) and *RBX1*$^{+/-}$ FT246 clones. The average of three technical replicates are presented. Growth curves depict initial cell attachment (0h to ~40h) and linear portion of exponential growth phase (~52 h to ~118 h, region highlighted in grey). ***(B)*** Bar graphs presenting the mean population doubling time (± SD) for control, Clone 1 and Clone 2. Student t-tests revealed no statistically significant differences in mean population doubling times for Clone 1 or Clone 2 relative to control. n/a, not applicable; ns, not significant. N=2, n=3.

4.2.4. Temporal Dynamics of CIN in *RBX1*$^{+/-}$ FT246 Clones

To determine whether heterozygous loss of *RBX1* impacts CIN within the *RBX1*$^{+/-}$ clones, time-course experiments were performed on continually growing cell cultures in which aliquots were assessed every 4 passages (equivalent to ~2 weeks) for ~3 months. More specifically, CIN phenotypes including NAs, MNF and chromosome numbers were assessed at regular intervals to provide insight into the long-term impact and temporal progression of CIN within each clone.

In general, dynamic changes in NAs were observed in the *RBX1*$^{+/-}$ clones over the period of ~3 months, relative to control clones (NTgRNA). The *RBX1*$^{+/-}$ clones also showed increases in NA heterogeneity relative to control (Figure 4.12A). Interestingly, the two *RBX1*$^{+/-}$ clones evolved differently over time. As illustrated in Figure 4.12B, Clone 1 showed a trend towards smaller NAs (left-ward shift) from Passage 0 (P0) to P12. However, from P16 onwards, the NA cumulative distribution frequency of Clone 1 showed a trend towards increasing NAs (right-ward shift), relative to the control. On the other hand, Clone 2 showed more drastic changes in NAs relative to the control. For instance, at P0, Clone 2 had relatively larger NAs. At P4, Clone 2 showed a shift towards smaller NAs, relative to the control. However, from P8 onwards, Clone 2 maintained an overall increase in NA as depicted by the right-ward shift in its NA cumulative distribution frequency. At all timepoints, the cumulative NA distribution frequency for the *RBX1*$^{+/-}$ clones differed significantly from the control, as revealed by the KS tests (p-value < 0.0001) (Figure 4.12B; Table S10). The dynamic changes in NAs shown by the *RBX1*$^{+/-}$ clones strongly support that the clones exhibit CIN.

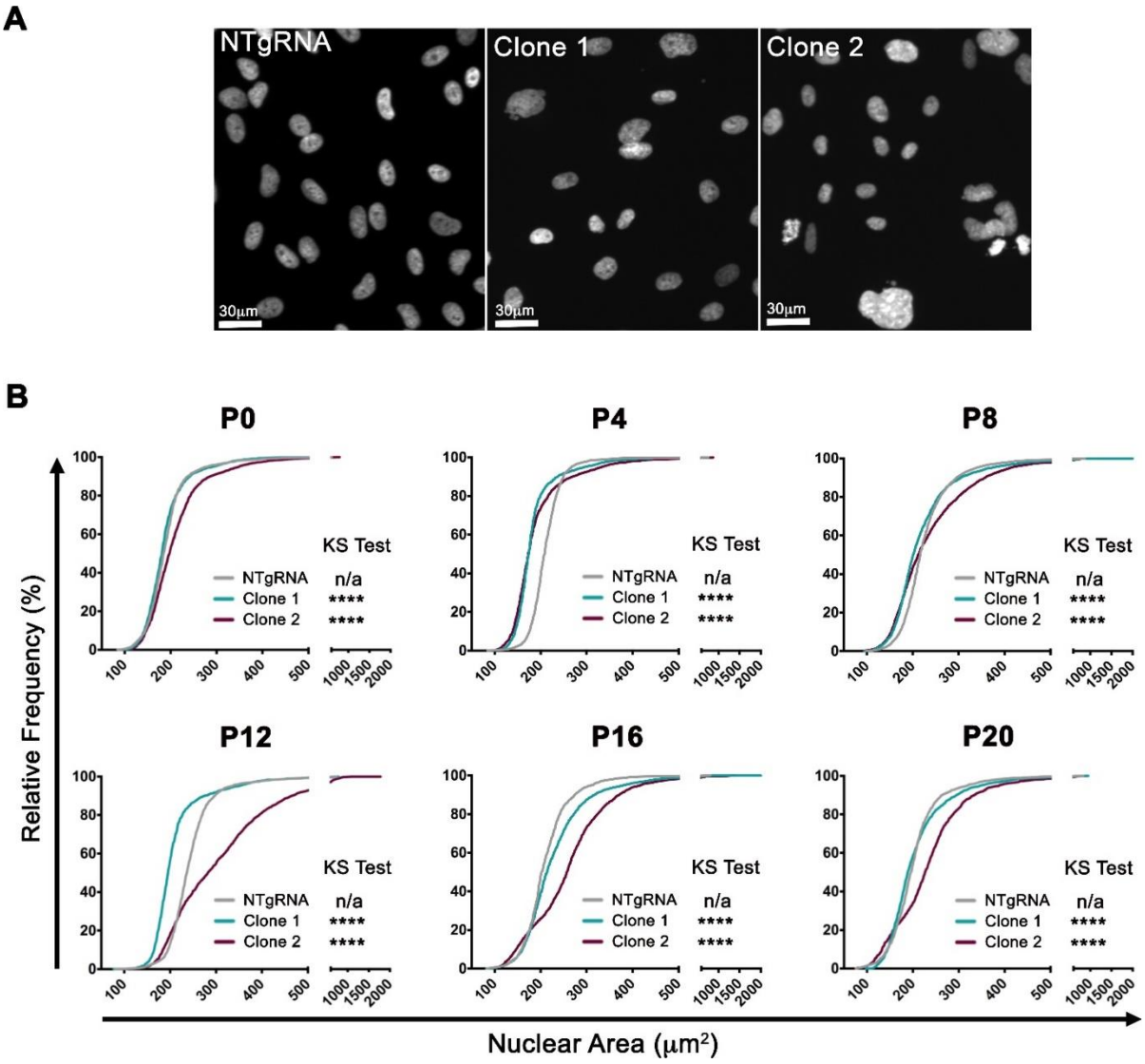

Figure 4.12. *RBX1*$^{+/-}$ FT246 clones exhibit dynamic changes in NAs relative to control.
(A) Representative low-resolution micrographs of Hoechst-labelled nuclei presenting visually apparent changes in nuclear sizes and increase in NA heterogeneity in *RBX1*$^{+/-}$ FT246 clones relative to control (NTgRNA). Scale bars are identical. ***(B)*** Cumulative NA frequency distributions reveal dynamic changes in NA in FT246 *RBX1*$^{+/-}$ clones at the six timepoints (Passage 0 [P0] to Passage 20 [P20]) relative to control (>2000 nuclei analysed/condition at each timepoint). KS-tests were employed for statistical comparisons; n/a, not applicable; ns, not significant; ****, *p*-value <0.0001.

Next, I sought to evaluate the impact heterozygous loss of *RBX1* has on MNF over time, relative to the control. As expected, both *RBX1*$^{+/-}$ clones had significantly higher fold increases in MNF at every timepoint, relative to the control (Figure 4.13). Interestingly, the two clones showed varying extents of MNF at the different timepoints. For example, Clone 2 consistently showed higher MNF than Clone 1 from P0 through P12. However, Clone 1 exhibited a striking increase in MNF as compared to Clone 2 from P16 onwards. Overall, at every timepoint the increases in MNF within the *RBX1*$^{+/-}$ clones relative to control were deemed statistically significant by the Mann-Whitney tests (Figure 4.13; Table S11). Indeed, the dynamics of MNF in the two *RBX1*$^{+/-}$ clones support that stable diminished *RBX1* induces CIN.

Collectively, the data obtained from the evaluation of the surrogate markers of CIN (NA and MNF) in the *RBX1*$^{+/-}$ clones at all time points strongly suggest that stable, long-term depletion of *RBX1* in the clones induce CIN. These findings also align with those obtained in the transient siRNA approach, where *RBX1*-silencing induced significant increases in the CIN-associated phenotypes. Recall that changes in NAs essentially reflect large-scale changes in chromosome content[128] whereas MNF is suggestive of small-scale changes in DNA content or structural CIN[129,130]. Thus, to complement and validate these findings, karyotypic analyses were performed to evaluate changes in chromosome numbers in *RBX1*-depleted clones at the identical timepoints as above. More specifically, mitotic chromosome spreads were generated and enumerated in the FT246 *RBX1*$^{+/-}$ clonal populations and control cells.

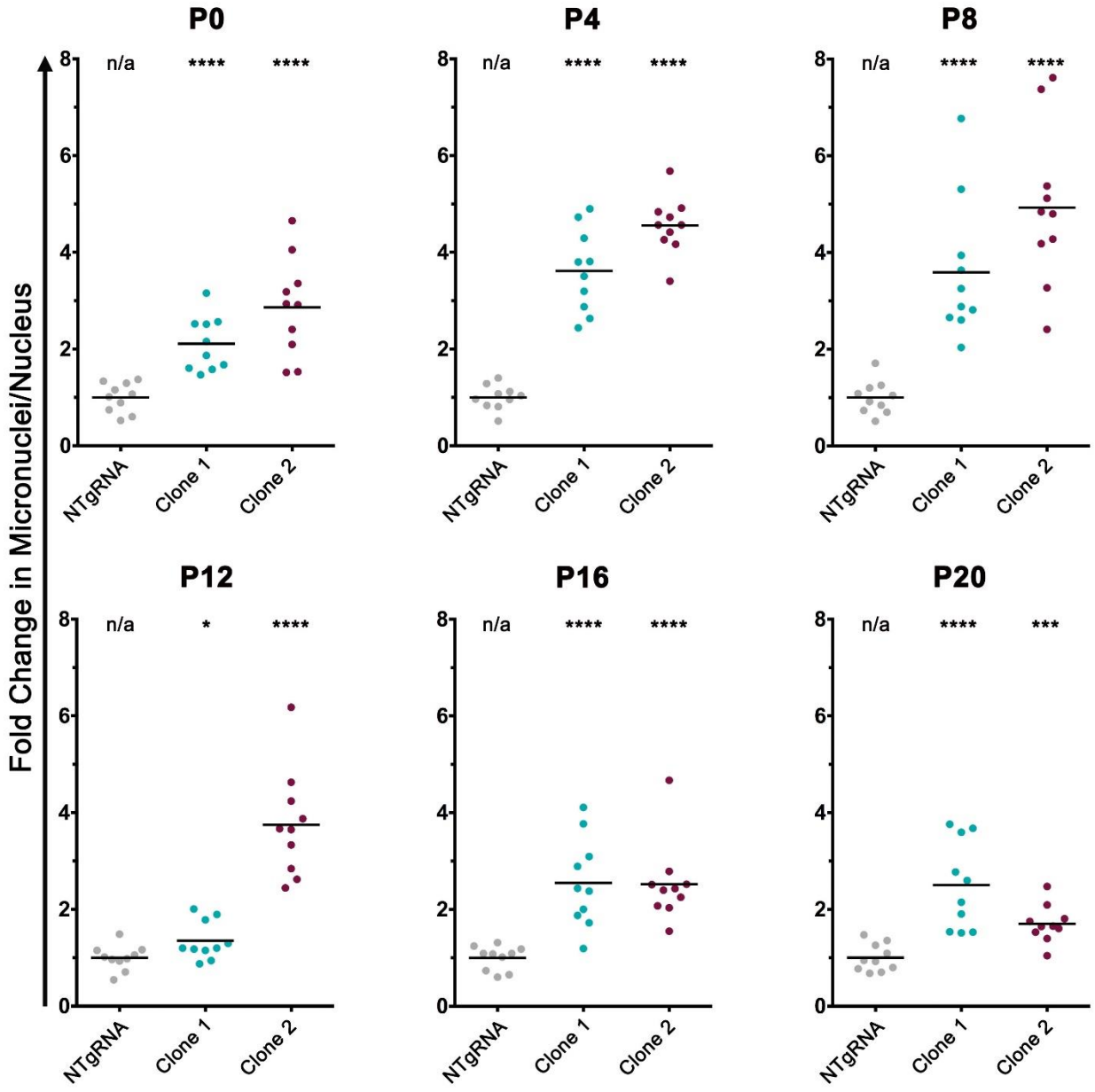

Figure 4.13. *RBX1*$^{+/-}$ FT246 clones exhibit dynamic changes in MNF relative to control. Dot plots presenting the fold change in MNF relative to the mean of control at six timepoints (P0 to P20). Black bar indicates the mean. (n=10, >600 nuclei/condition). Mann-Whitney test; n/a, not applicable; *, *p*-value <0.05; ***, *p*-value <0.001; ****, *p*-value <0.0001. Fold increases relative to control (set at 1).

In agreement with the CIN phenotypes observed above, the *RBX1*$^{+/-}$ clones showed dynamic changes in chromosome numbers over time. Prototypic examples of mitotic chromosome spreads of the control (46 chromosomes) and *RBX1*$^{+/-}$clones (loss, small-scale gain and large-scale gains) are depicted in Figure 4.14. Briefly, as illustrated in Figure 4.15, both clones exhibited increasing heterogeneity in chromosome numbers from P0 to P20, relative to the control. Both *RBX1*$^{+/-}$ clones show evidence of tetraploidization occurring, relative to the control, with Clone 2 displaying a more pronounced phenotype. Strikingly, at P20, Clone 2 consisted mostly of polyploid cell populations whereas Clone 1 emerged as a highly heterogenous population, with the cell population having high degree of variability in chromosome numbers. KS tests identified that the changes in chromosome numbers in the *RBX1*- depleted clones were statistically significant relative to the control, at all timepoints. (Table S12). The dynamic changes observed in NAs, MNF and chromosome numbers at all timepoints are in agreement and universally display the increasing cell-cell heterogeneity in the *RBX1*$^{+/-}$ clones relative to controls, thus validating *RBX1* as a novel CIN gene.

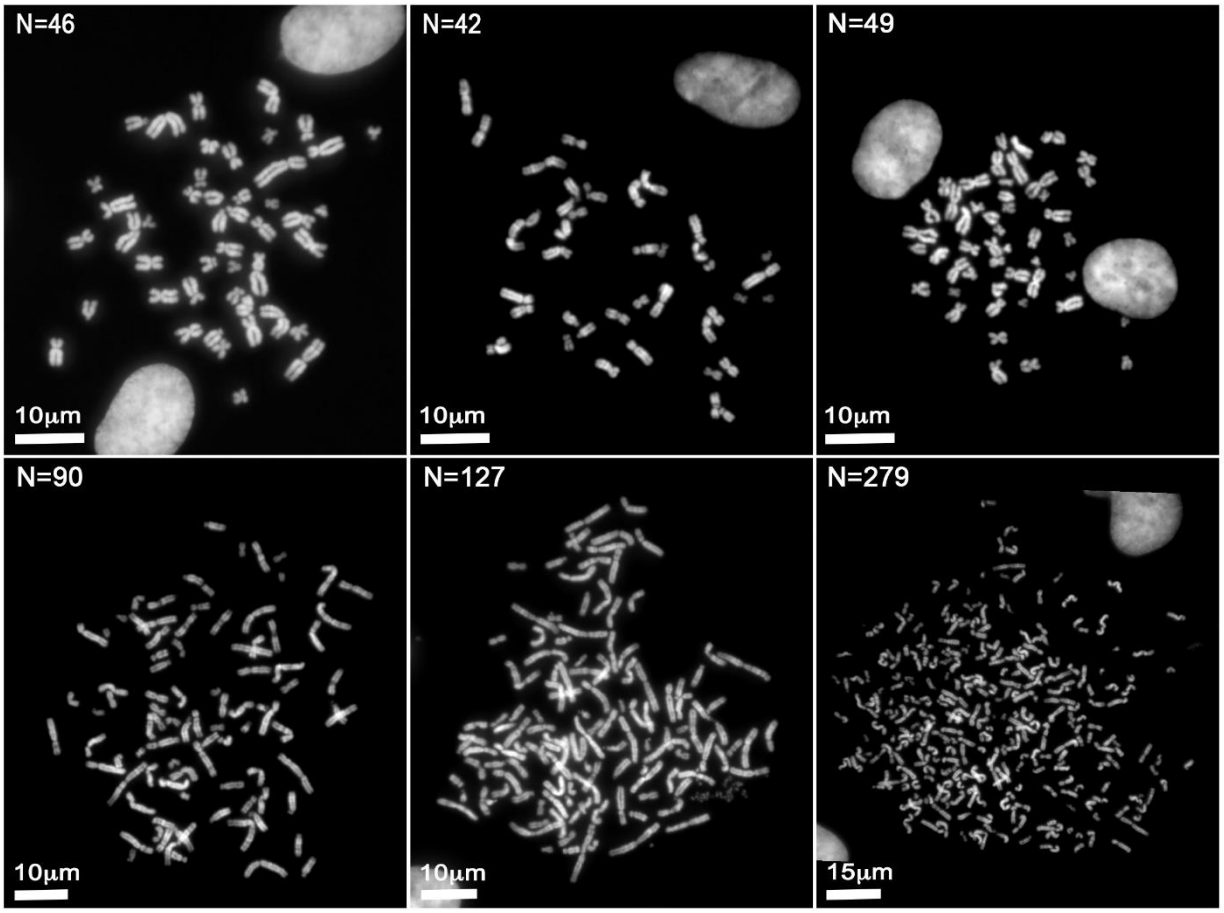

Figure 4.14. Numerical changes in chromosome observed in the *RBX1*$^{+/-}$ FT246 clones relative to control.

Representative high resolution 2D images (63x) of mitotic chromosome spreads from FT246 clonal control cells (NTgRNA), displaying modal number of 46 chromosomes (top, left) and FT246 *RBX1*$^{+/-}$ clones showing chromosome loss (top, middle), small-scale chromosome gain (top, right) and large-scale gains (bottom panel).

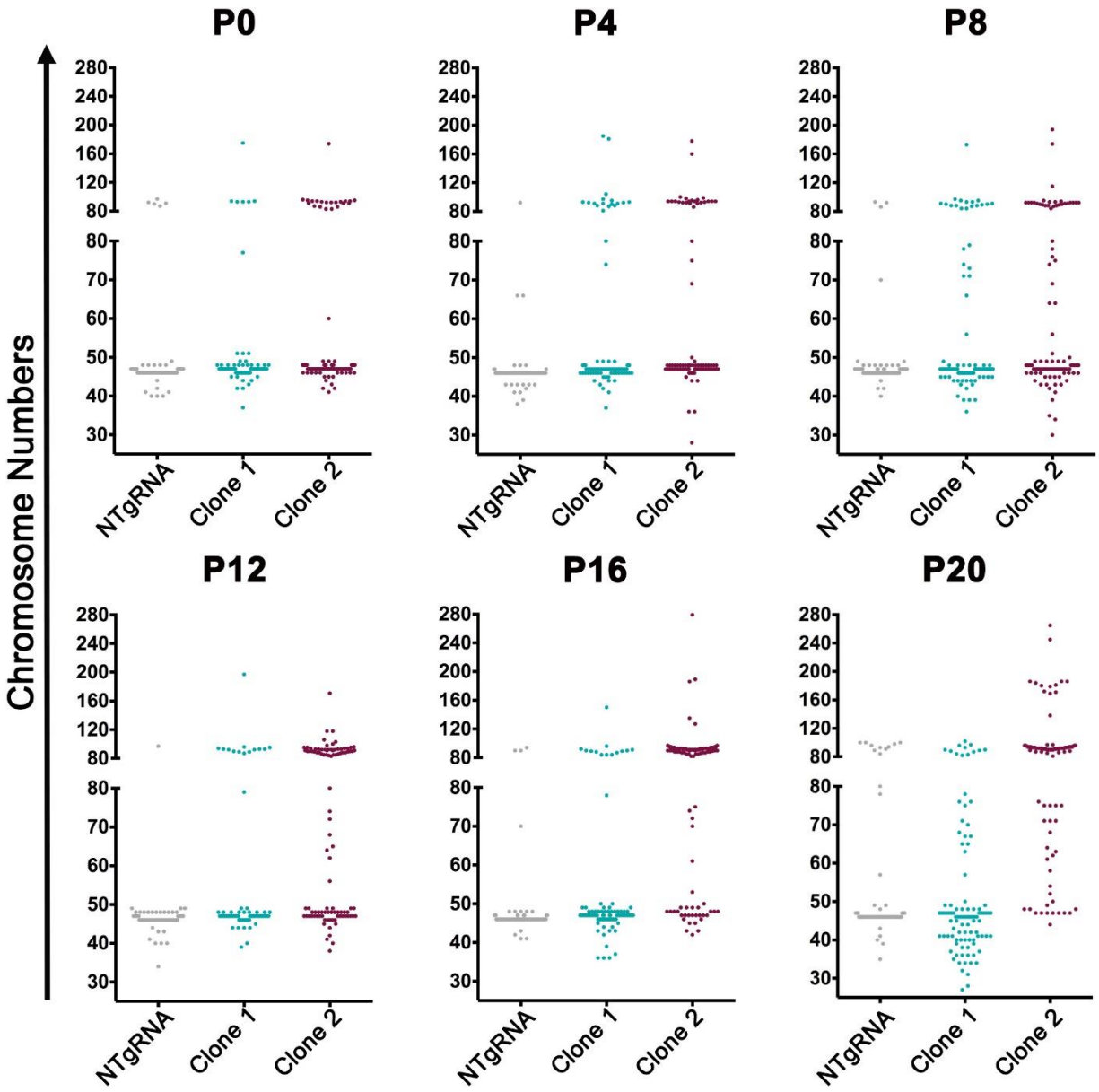

Figure 4.15. *RBX1*$^{+/-}$ FT246 clones show dynamic changes in chromosome numbers relative to control.

Dot plot displaying the number of chromosomes enumerated from each *RBX1*$^{+/-}$ FT246 clone relative to control, at six timepoints (P0-P20). Chromosomes were enumerated from a minimum of 100 mitotic chromosome spreads/condition.

4.2.5 Evaluating Cellular Transformation in *RBX1*$^{+/-}$ FT246

After identifying and validating *RBX1* as a CIN gene, we next wished to assess whether the CIN induced in the FT246 *RBX1*$^{+/-}$ clones can drive cellular transformation. Accordingly, cellular transformation was assessed by performing standard colony formation assays in soft agar to evaluate anchorage-independent cellular growth. The soft agar assay is the gold standard for assessing cellular transformation *in vitro* and growth in soft agar is strongly associated with tumorigenic potential. The colony formation assay was performed as detailed in Materials and Methods, (Section:3.8.2, Page 59). HCT116 and OVCAR3 (a HGSOC cell line) were employed as positive controls[178,179], while wildtype and control (NTgRNA) were included as negative controls. Colonies greater than 100 µm were automatically enumerated using the GEN5 software

As illustrated in Figure 4.16, the HCT116 cells formed numerous colonies (a mean of 112 colonies/well). The OVCAR3 cells failed to form noticeable colonies (a mean of 0.7 colonies/well), which was unexpected. The wildtype FT246 cells did not form colonies. A few colonies (a mean of 1.67 colonies/well) were observed in the control, NTgRNA. Interestingly, both Clone 1 and Clone 2 showed increased colony formation (a mean of 45.7 colonies/well and 10.7 colonies/well, respectively), relative to the control. Accordingly, Clone 1 and Clone 2 had a ~28- and ~6-fold increase in colony formation, respectively as shown in Figure 4.17A. In addition, colony sizes from each condition are presented in Figure 4.17 B. The mean colony sizes of the positive controls were the highest (152 µm for HCT116 and 144 µm for OVCAR3). Although Clone 2 had lower number of colonies formed than Clone 1, the sizes of the colonies scored were larger in Clone 2 than in Clone 1; mean colony size of Clone 2 was 136 µm whereas mean colony size of Clone 1 was 118 µm. Taken together, these findings suggest that single allele loss of *RBX1* results in an increase in anchorage-independent growth, indicating cellular transformation.

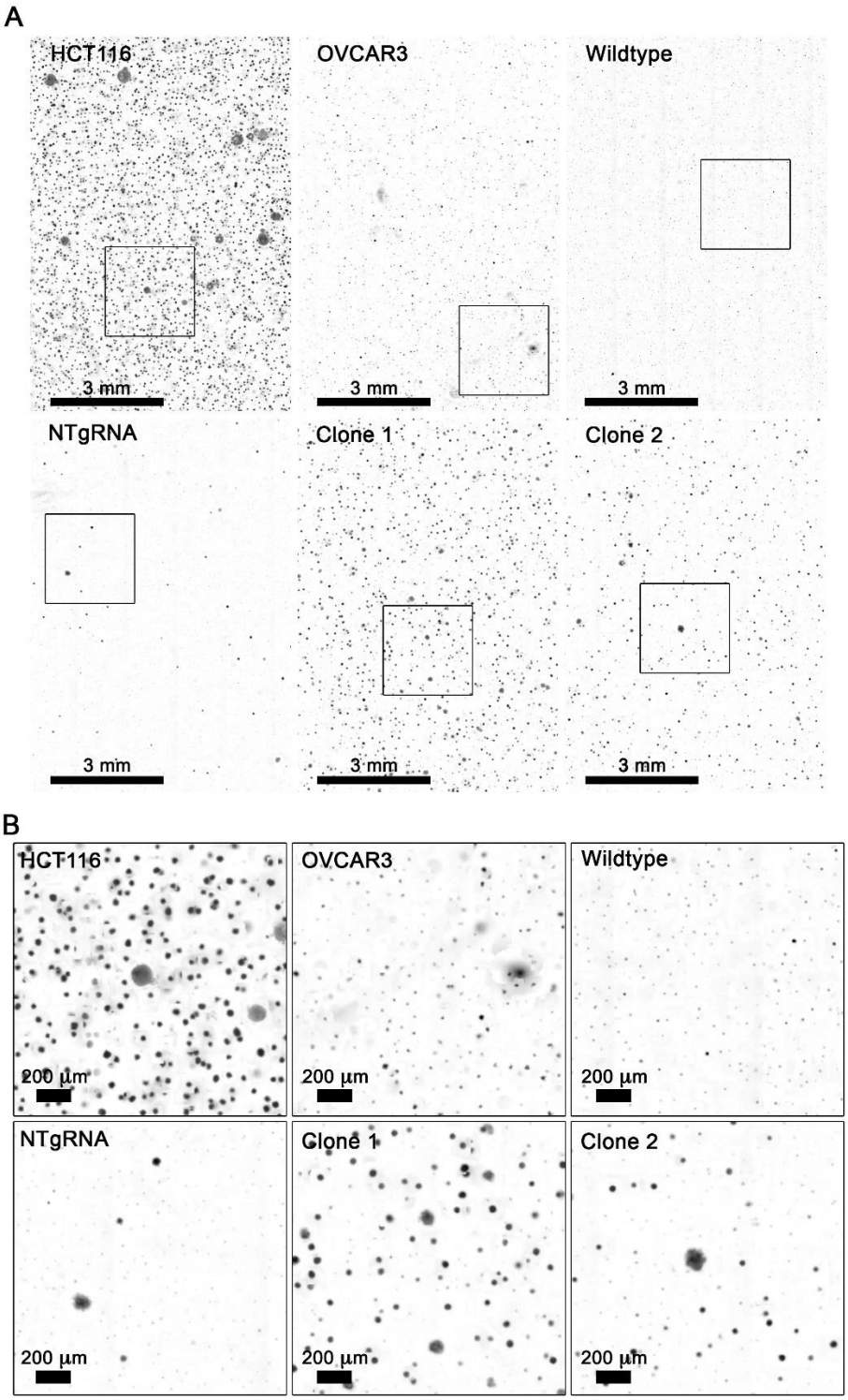

Figure 4.16. Representative images from colony formation assay in soft agar.
(A) Representative low-resolution (4×) bright field stitched images from one well of each condition. ***(B)*** Magnified boxed area in panel above, revealing individual colonies.

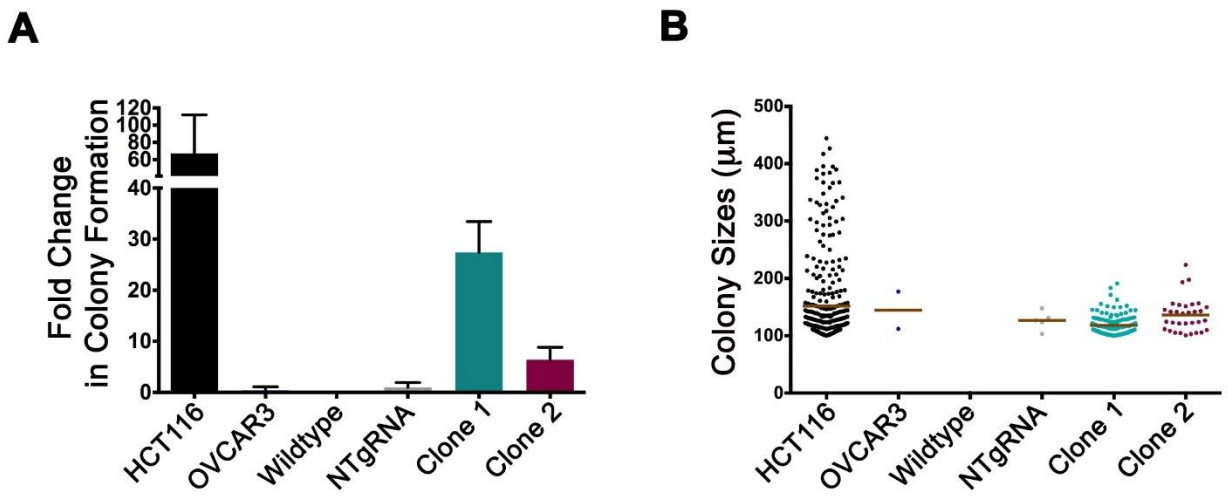

Figure 4.17. *RBX1*$^{+/-}$ FT246 clones have enhanced colony formation relative to negative control.

(A) Bar graphs present the fold change in colony formation (± SD), relative to control (NTgRNA, which is set to 1). OVCAR3 and HCT116 were employed as positive controls. ***(B)*** Dot plots presenting colony sizes quantified within each condition. Brown bar indicates mean. N=1, n=3 (wells/condition).

SUPPLEMENTARY FIGURES:

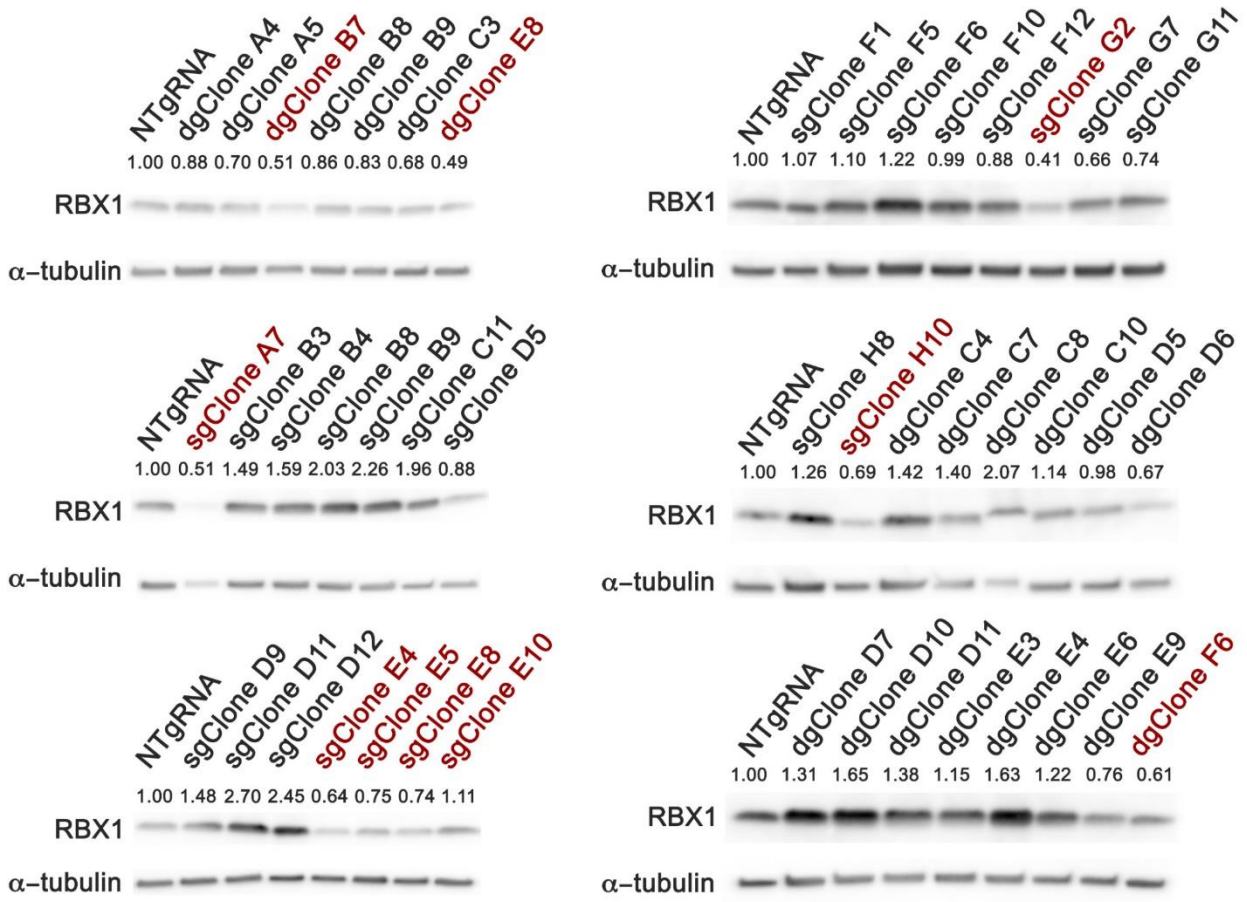

Supplementary Figure 1. Screening for *RBX1*$^{+/-}$ FT246 Clones.
(A) Semi-quantitative western blots showing RBX1 expression levels in 45 distinct FT246 clones isolated following CRISPR/Cas9 mediated targeting of *RBX1*; α-tubulin loading control. Red text indicates the clones with reduced RBX1 expression that were selected for further expansion and DNA sequencing.

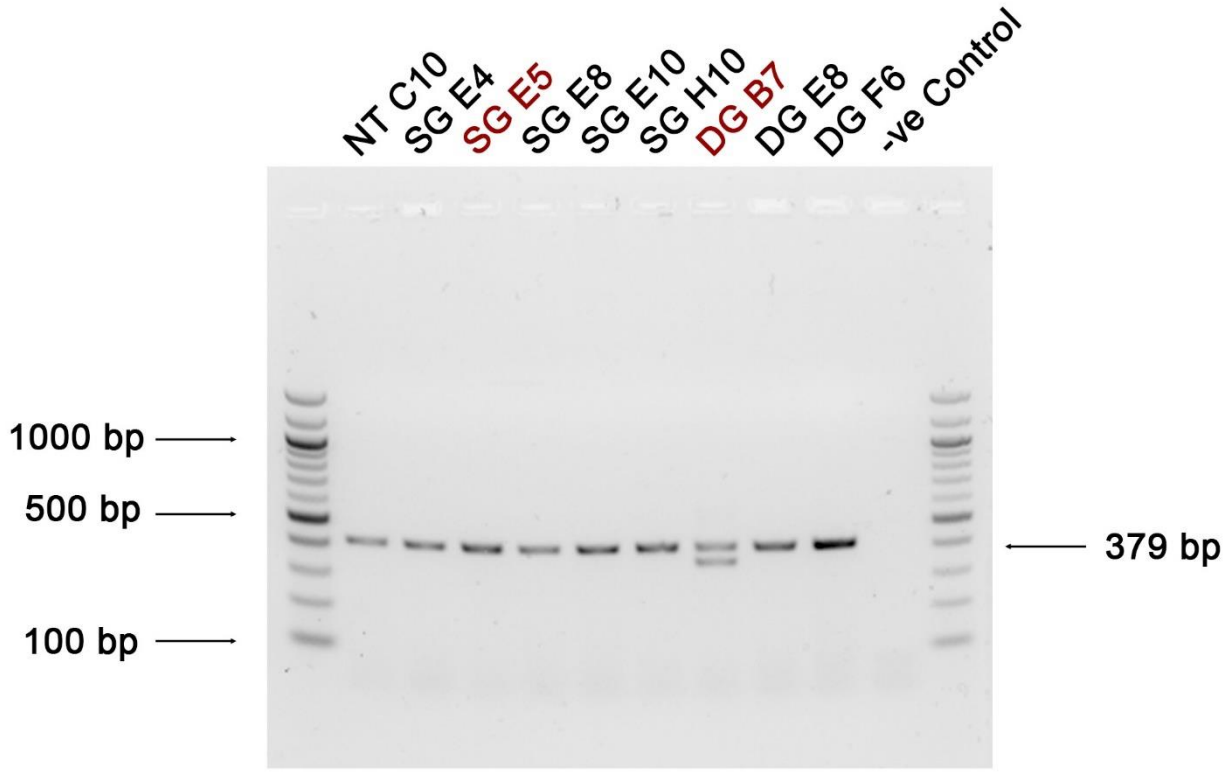

Supplementary Figure 2. PCR amplification of the CRISPR-targeted region of candidate *RBX1*$^{+/-}$ FT246 Clones.
Gel image showing the PCR products that were sent for DNA sequencing. The potentially edited genomic locus surrounding the gRNA recognition site (exon 2 of *RBX1*) was amplified. Red text indicates clones that were subsequently confirmed as harboring *RBX1* edits (*RBX1*$^{+/-}$) by DNA sequencing. Note the double band in Clone DG B7 identifies a putative large deletion and is suggestive of an *RBX1* edit.

CHAPTER 5: DISCUSSION

5.1. Summary and Conclusions

To evaluate *RBX1* as a candidate CIN gene, I applied two approaches, siRNA-based and CRISPR-Cas9, to diminish *RBX1* expression. Subsequently, I evaluated the impact reduced *RBX1* expression has on CIN. In addition, attempts to elucidate some of the potential mechanisms underlying CIN were made by assessing levels of Cyclin E1, a well-characterized SCF complex substrate and a known driver of CIN. In general, *RBX1* silencing induced aberrant increases in Cyclin E1 in HCT116 and FT246, although the increases were more pronounced in HCT116 than in FT246. FT194, however, showed no increase in Cyclin E1 levels upon diminished *RBX1* expression. While increased Cyclin E1 levels do provide mechanistic insight on CIN, the mechanisms underlying CIN cannot be exclusively attributed to increased Cyclin E1. For instance, recent work done by Dr. Thompson in the McManus lab showed that *SKP1* (which encodes the adaptor protein of the SCF complex) silencing resulted in increased Cyclin E1 levels and CIN-associated phenotypes. However, when she performed *SKP1* and *CCNE1* co-silencing, only a partial phenotypic rescue was observed, implying that additional mechanisms (e.g. other key proteins important in cell division such as DNA damage repair[115,116], centrosome duplication[98,110-112], in mitotic spindle assembly[43], sister chromatid cohesion[113], kinetochore-microtubule attachment[108,109], cytokinesis[114]) involving other substrates may contribute to the CIN phenotypes.

In general, *RBX1* silencing induced increases in NAs and MNF in all the three cell lines utilised within this study, i.e. HCT116, FT194 and FT246. Further experiments also showed that *RBX1* silencing drives changes in chromosome numbers, independent of the cell type, identifying *RBX1* as a novel CIN gene. However, differences in the strength of the CIN phenotypes were observed between the cell lines, with HCT116 consistently showing the most pronounced CIN

phenotypes, followed by FT246 and FT194. Differences in silencing efficiencies could potentially account for the differences observed in the strength of the CIN phenotypes. *RBX1* was most efficiently silenced in HCT116 as shown by the western blots in Figure 4.1B (Section 4.1.1., Page 61), resulting in only 4-5% of residual RBX1 protein. On the other hand, *RBX1* expression was diminished to 24% and 16% in FT194 and FT246, respectively, which could explain the less severe CIN-associated phenotypes observed in the FT lines. Alternatively, differential gene expression profiles of the three cell lines could be an underlying factor for the differences in the strength of the CIN phenotypes. For instance, HCT116 is a human colorectal carcinoma cell line harbouring a DNA mismatch repair defect stemming from a mutation in *MLH1*[180] which results in the accrual of background mutations especially within the microsatellite (repetitive DNA sequences consisting of 1-6 bp) region. Therefore, the presence of background mutations may synergise with *RBX1* silencing, thus exacerbating the CIN phenotypes in HCT116. This could also potentially explain the drastic increase in decondensed mitotic spreads observed exclusively in HCT116, majority of which were not enumerable (Section 4.1.4, Page 70). In contrast, the FT cell lines are non-cancerous, immortalized through human *TERT* (telomerase reverse transcriptase gene) integration and re-expression. In addition, FT cells are DNA mismatch repair proficient, which may moderate their CIN phenotypes. Also, others have shown that hTERT re-expression is associated with enhanced genome stability and DNA repair, although more specifically at telomeric regions[181], which may function to limit their CIN phenotypes in response to *RBX1* silencing.

Another anomaly encountered within the silencing approach results was the trend towards increasing NAs (indicative of potential large-scale gains of chromosomes), yet mitotic chromosome spreads analysis showing both chromosomal losses and gains. In some instances, particularly within the HCT116 and FT426 cells, the frequency of chromosome losses outweighed

that of chromosome gains. One possible explanation for this discrepancy is that the larger nuclei (likely polyploid) continue through subsequent rounds of DNA replication without undergoing mitosis, a process termed endoreduplication. In addition, previous studies have shown that artificially induced polyploidy can elicit a premature mitotic exit[182]. Thus, as the frequency and/or duration of mitosis may decrease within these cells, the probability of capturing them in metaphase spreads may be reduced. Overall, *RBX1* silencing induced statistically significant increases in NAs, MNF as well as changes in chromosome numbers in all the three cellular contexts employed within this study, which is consistent with *RBX1* being a novel CIN gene.

5.1.1. Heterozygous Loss of *RBX1* may be an Early Event Contributing to Oncogenesis in HGSOC

After establishing that transient *RBX1* silencing induces CIN, I next sought to determine the impact stable loss of *RBX1* had on CIN and cellular transformation. The primary focus of this aim was to gain critical insight on the early events leading to HGSOC pathogenesis. Importantly, heterozygous loss of *RBX1* occurs at a high frequency in HGSOC (~83%). Therefore, generating clonal populations of precursor cells with heterozygous loss of *RBX1* may provide insight into early disease etiology. Unfortunately, no homozygous knockout clones were generated in this study, suggesting that *RBX1* is as essential gene in human cells. Moreover, *RBX1* is evolutionarily conserved across species, which further supports its essentiality[144]. In addition, this possibility is consistent with studies done in several model organisms where homozygous deletion was found to be lethal[141,145-148]. Also, the fact that *RBX1* is widely expressed across normal human tissues[144] suggests that its function is indispensable for the proper cellular functioning and even a partial depletion (e.g. heterozygous loss) could potentially be pathogenic.

After generating and characterising (cellular morphology and growth kinetics) the *RBX1*$^{+/-}$ FT246 clones, the clones were employed in time-course experiments to investigate the long-term impact of heterozygous loss of *RBX1* on CIN. Importantly, all the CIN assays at each time-point were performed concomitantly, and dynamic CIN patterns were observed during the evolution of the *RBX1*$^{+/-}$ clones. In addition, cellular transformation was assessed by performing colony formation assay in soft agar. In general, the *RBX1*$^{+/-}$ FT246 clones showed similar cellular morphology and proliferation rates as the control cells, NTgRNA (Section 4.2.3, Page 85-86). However, results from the time-course CIN analyses reveal that both *RBX1*$^{+/-}$ FT246 clones, Clone 1 and Clone 2, display a highly dynamic CIN pattern, relative to the control. In general, Clone 2 showed more severe CIN phenotypes than Clone 1, regarding increases in NAs and NA heterogeneity at all timepoints (Section 4.2.4, Page 83). Clone 2 also showed higher fold increases in MNF than Clone 1, except for the last two time-points (P16 and P20), where Clone 1 displayed a higher fold increase in MNF than Clone 2 (Section 4.2.4, Page 85) which reflects small-scale changes in chromosome complements. This is further indicated in the increased frequency of chromosome losses observed at P16 and P20 in Clone 1 (Section 4.2.4, Page 88). In contrast, Clone 2 showed reduced MNF relative to Clone 1 (yet higher than control) but massive increases in chromosome numbers at P12 to P20. Interestingly, very few diploid cells were scored from Clone 2 at P20 (Section 4.2.4, Page 88) from a minimum of 100 mitotic chromosome spreads enumerated. These data suggest that Clones 1 and 2 evolved differently over the three months. This is not unexpected as CIN produces a highly heterogeneous phenotype, involving random gains and losses of chromosomes. Therefore, the extent of CIN phenotypes observed would greatly depend on the specific chromosomes being gained or lost. Ultimately, it is expected that the cells with the karyotypic changes that carry the best survival advantages will grow and give rise to the "fittest"

clones[183,184]. Thus, CIN drives cell-to-cell heterogeneity and over time, this can give rise to distinct subclones with specific survival benefits, creating highly heterogeneous cell populations which can be seen within both Clones 1 and 2. Moreover, the two *RBX1*$^{+/-}$ clones may evolve differently and have varying extent of CIN phenotypes if there is any functional compensation by the wild-type allele (for e.g. increased mRNA and/or protein stability). Another interesting observation was the occurrence of tetraploidization events in both clones (more noticeable in Clone 2) and the emergence of the largely polyploid populations in Clone 2 at the end of the time-course experiment.

Many early stage tumors have been reported to contain tetraploid cells[185-187]. In addition, polyploidization is considered an early step during evolution where the redundant set of chromosomes acts as a pool of genetic material allowing for clonal selection and evolution[184]. There is also growing evidence pointing to the potential of tetraploidization to induce CIN and drive cellular transformation in mammalian cells[188,189]. Results from the colony formation assay showed that Clones 1 and 2 had increased colony formation relative to the control (Section 4.2.5, Pages 90-91). However, Clone 1 showed a 28-fold increase in colony formation whereas Clone 2 only had a 6-fold increase, relative to control cells. This was unexpected as Clone 2 consistently showed exacerbated CIN phenotypes throughout the experiments. Thus, the reduced colony formation in Clone 2 may be attributed to increased cell death due to higher CIN levels. Surprisingly, the positive control, OVCAR3, did not form as many colonies. However, since the other positive control cells, HCT116, formed numerous, macroscopic colonies, there could be other unidentified biological factors confounding the results for OVCAR3. Overall, in order to conclude whether the *RBX1*$^{+/-}$ FT246 clones have been transformed, other additional phenotypes associated with cellular transformation, such as migration, invasion, self-renewal capacity need to

be assessed. Moreover, it is important to note that neoplastic transformation is a multistep, sequential event that takes place over a long duration. For instance, in HGSOC, a window of about 7 years has been estimated between the formation of a precursor lesion in the fimbriae of the fallopian tube and the onset of ovarian carcinoma[60]. Overall, our data show that *RBX1*$^{+/-}$ FT246 clones display dynamic patterns of CIN, high cell-to-cell heterogeneity as well as phenotype associated with cellular transformation. Recent studies have also revealed that CIN in prevalent in HGSOC patients' samples[93]. Since the findings from this study determine that precursor HGSOC cells exhibit CIN upon heterozygous loss of *RBX1*, copy number loss of *RBX1* may be an early event contributing to HGSOC pathogenesis.

5.2. Interpretation of Data in the Context of Current Literature

Data presented within this thesis suggest that one plausible mechanism contributing to CIN could be increased Cyclin E1 levels, resulting from the loss of *RBX1* expression (and impaired SCF complex function). Overexpression of Cyclin E1 as a consequence of genomic amplification has been found to induce CIN and contribute to the pathogenesis of many cancers, including HGSOC, breast cancer, liver cancer and non-small cell lung cancer[94,98-103]. It is important to note that the SCF complex mediates the polyubiquitination and degradation of a myriad of protein substrates that function in key cellular processes including cell cycle regulation, DNA replication, transcription, and development[134,137-141,190]. Thus, misregulation of many of these processes could result in the accumulation of substrates, many of which may directly or indirectly induce CIN and contribute to oncogenesis. Thus, loss of *RBX1* expression and diminished SCF function may represent early etiological events in the initiation and/or progression of cancer through the accumulation of oncogenic substrates like Cyclin E1.

It is noteworthy that RBX1 functions in other E3 ubiquitin ligases, beyond the SCF complex. Another mechanism that has been reported to contribute to aneuploidy and CIN in HGSOC is genomic amplification of Aurora A[191-193], an important kinase permitting entry into mitosis[194]. Interestingly, RBX1 also forms part of the CUL3-KLHL18 E3 ligase complex, which regulates the activity of Aurora A kinase, which is essential for mitotic fidelity[195]. Therefore, it remains possible that reduced *RBX1* expression may also adversely impact Aurora A kinase activity, and thus, contribute to CIN. In addition, *RBX1* also functions in mouse oocyte maturation in meiosis[196]. More specifically, Zhou *et al*[196]. showed the dynamic distribution and localization of RBX1, its direct association with chromosomes in meiosis and its reduced expression leading to accumulation of Early Mitotic Inhibitor 1 (EMI1), an inhibitor of the Anaphase Promoting

Complex/Cyclosome (APC). Further, reduced APC activity led to accumulation of securin (a protein which plays an essential role in spindle assembly checkpoint), and Cyclin B1, thereby impairing homologous chromosome separation and progression to anaphase.

In addition, RBX1 (as part of CUL4A-RBX1-COPS8 E3 ligase molecule) has been reported to catalyze the ubiquitination of Centromeric Protein A (CENPA)[197,198], a centromere specific histone H3 variant. Ubiquitination of CENPA is essential for its recruitment and localization at the centromeres. Since centromeres are the chromosomal loci that mediate chromosome segregation during mitosis their normal functioning is required to maintain genome stability and ensure proper chromosome segregation. Importantly, misexpression and/or mislocalisation of CENPA has also been shown to induce CIN and oncogenesis[199-202]. Taken together, the current literature on *RBX1* functions further highlights the polyvalent potential of *RBX1* in inducing CIN via alternative complexes and pathways. Therefore, by evaluating CIN and the intrinsic mechanisms involved in response to diminished *RBX1* expression, critical insights can be gained in the CIN-associated oncogenic pathways.

5.3. Future Directions

Although *RBX1* is frequently deleted in various cancers, with heterozygous losses occurring at higher frequencies, there is currently a paucity of information at the level of the protein. In theory, loss of an allele corresponds to reduced protein expression; however, they may not always translate to a loss of protein expression and/or function. To further confirm the loss of *RBX1* in cancers, it will be important to characterize RBX1 protein expression patterns in tumor microarrays by immunohistochemistry (IHC). This will also provide critical information about any diagnostic and/or prognostic value of *RBX1* in cancer. Once diminished expression of RBX1 at the protein level in patient samples is established, additional experiments could be designed to investigate the mechanisms that induce CIN and contribute to oncogenesis.

5.3.1 Elucidating the Underlying Mechanisms of CIN

As detailed in Section 5.2 above, diminished *RBX1* has the potential of inducing CIN via a multitude of pathways. To gain deeper insight into the mechanisms through which reduced *RBX1* expression may induce CIN, additional experiments need to be performed. For instance, co-silencing of *RBX1* and potential CIN-substrates (e.g. *CCNE1*, *AURKA*) could be carried out and the downstream impact on CIN-phenotypes (Section 1.4.1, Page 16) could be determined. If the co-silencing experiments result in a phenotypic rescue, it is a strong indication of a causal relationship between diminished *RBX1* expression and CIN, via the misregulation of the specific CIN-substrate silenced together. Additionally, other experiments could be performed to thoroughly investigate the mechanisms of CIN. For instance, immunofluorescent labelling of centrosomes could be performed upon silencing *RBX1*, to assess if supernumerary centrosomes occur. Recall that Cyclin E1 plays an important function in centrosome duplication. Thus, if CIN is induced via Cyclin E1 mechanism, we would expect to see an increase in supernumerary

centrosomes in *RBX1*-silenced cell populations. Alternatively, CENPA immunofluorescent labelling would also be critical to evaluate if reduced *RBX1* expression underlies CIN via a CENPA mechanism. Importantly, mislocalization and/or misexpression of CENPA in *RBX1*-depleted cells would provide strong evidence for the implication of *RBX1* in centromere biology and maintenance of chromosome stability.

5.3.2 Assessing the Tumorigenicity of *RBX1*$^{+/-}$ FT246 clones

Our data show that single allele loss of *RBX1* induces CIN which could be an early event in the pathogenesis of HGSOC. In addition, our findings support that heterozygous loss of *RBX1* promotes cellular transformation, which further strengthens the potential implications of *RBX1* in driving early pathogenic events underlying HGSOC. However, additional experiments are required to thoroughly examine the impact of copy number loss of *RBX1* on cellular transformation and oncogenesis. The cellular models generated and employed within this study provide an ideal starting point to study early disease development in HGSOC as they recapitulate the genetic aberrations of precursor HGSOC cells. However, improvements to existing models will enable a more accurate representation of the microenvironment of the precursor cells. For example, there have been several studies that have reported chronic inflammation as a driver of oncogenesis[34,203,204]. Therefore, experiments should be designed considering factors like chronic inflammation including reactive oxygen species (ROS) that have been hypothesised to play a major role in the earliest stages of neoplastic growth in HGSOC. This was first proposed by Fathalla *et al.*[48], through his "incessant menstruation" theory where he proposed the number of lifetime ovulations as a risk factor for ovarian cancer. Furthermore, a study by King et al[51]. showed that superovulation in mice led to increased DNA damage and release of inflammatory immune mediators. In addition, use of contraceptive pills, pregnancy and parity (i.e. the condition of having

given birth) have all been associated with a lower risk of developing ovarian cancer[205-207]. These factors reduce the overall number of ovulation cycles and hence limit the exposure of the cells to inflammatory mediators[208,209]. Furthermore, some epidemiological studies have reported a reduced risk of developing ovarian cancer with late onset of menarche and early menopause[210,211]. Based on these previous reports, chronic inflammation emerges as a crucial factor for driving cellular transformation. Thus, an important future aim of this study would ideally be to employ *RBX1*$^{+/-}$ FT246 clones and simultaneously investigate the impact of inflammation and diminished *RBX1* expression on cellular transformation in HGSOC precursor cells. One approach to mimic the genotoxic stress and induce ROS production within the cells would be by exposing the *RBX1*$^{+/-}$ clones to ionizing radiation and subsequently performing analogous experiments to evaluate cellular transformation as described earlier (Section 3.8, Page 59). Alternatively, to better model the periodic oxidative stress in the precursor cells, the cells could be treated at regular intervals with hydrogen peroxide, an approach commonly employed to elicit ROS production in cells[212]. In addition to evaluating anchorage-independent growth, other assays could be employed to evaluate other phenotypes associated with cellular transformation. These phenotypes include cell invasion and migration (through transwell cell invasion and migration assays[213]) and self-renewal capacity (by employing ultra-low attachment plates, to assess microsphere formation *in vitro*[214]).

If the above assays reveal positive results for cellular transformation, further studies could be employed to better mimic the biological conditions. More specifically, it would be appropriate to perform intraperitoneal injection of the *RBX1*$^{+/-}$ FT246 into immunocompromised female mice models and assess tumor formation and growth. Additionally, injection of clonal populations of NTgRNA cells in nude female mice would be performed for control purposes. If tumor formation takes place in *RBX1*$^{+/-}$ FT246 xenografts relative to controls, it would be highly supportive of

heterozygous loss of *RBX1* being an important driver of the early oncogenic events leading to HGSOC.

5.3.3. Exploiting Reduced *RBX1* Expression to Selectively Target Cancer Cells Using Synthetic Lethal (SL) Approach

RBX1 is deleted in many cancers, with heterozygous loss being the most frequent type of genetic aberration[83,161-165,168,215,216], particularly in HGSOC (~83%) and colorectal cancer (~25 %) (Section 1.5.2, Pages 24-25). Defects like deletions and loss of function mutations can be exploited by Synthetic Lethal (SL) approaches to selectively target cells harbouring those genetic aberrations. SL describes a rare and lethal combination of two gene deletions or mutations that are independently viable[217,218]. The SL approach has shown promise in treating women with *BRCA1/2* mutations in breast and ovarian cancers, through the use of Olaparib , which is a PARP inhibitor[219]. This results in excessive DNA damage leading to the selective death of cancer cells while the normal cells remain viable with proficient *BRCA1/2*. Therefore, it would be highly valuable to identify SL interactors for a gene like *RBX1* which is frequently deleted in cancer cells. For instance, employing the *RBX1*$^{+/-}$ FT246 clones in the screening for SL interactors would help in the identification of potential drug targets tailored for patients carrying heterozygous loss of *RBX1*. Potential SL interactors (or drug targets) often occur within the same pathways. Hence, screening could be done by silencing potential binding partners of RBX1 (e.g. CUL1 in the SCF complex) which work within the same pathways, in *RBX1*$^{+/-}$ FT246 cells. Once a SL interactor of *RBX1* is identified, small molecule inhibitors could be employed to downregulate the drug target and cause selective death of cancer cells carrying the heterozygous loss of *RBX1*. For further validation, the SL experiments can be migrated into animal models. If successful, the SL approach will benefit the large number of patients carrying heterozygous loss of *RBX1*. This highlights the enormous

potential that SL approaches hold in the targeted therapy of cancers. As SL specifically exploits the aberrant pathways driving oncogenesis, this would minimise side-effects generally associated with current chemotherapy and greatly improve quality of life and survival chances of cancer patients.

5.4. Significance

This study revealed the novel finding that diminished *RBX1* expression induces CIN in three cellular contexts. Further, experiments to model early disease development in HGSOC showed that heterozygous loss of *RBX1* drives CIN and promotes cellular transformation of precursor HGSOC cells. The CIN patterns observed were dynamic and evolved over time, with the emergence of highly heterogeneous cell populations within the *RBX1* heterozygotes. These findings strongly suggest that *RBX1* may contribute to the early pathogenic events of HGSOC and potentially, to disease progression as well. It is important to note that diminished *RBX1* is also associated with worse patient prognosis in HGSOC (Section 1.5.2, Page 26), which further highlights the significance of *RBX1* as a CIN gene with possible pathogenic implications in HGSOC. Besides, this study has generated valuable tools that will be useful in future research to elucidate relevant pathways and mechanisms impacted by diminished *RBX1* expression. Also, these cell lines generated could be employed in identifying novel drug targets that exploit deficiency in *RBX1*. Such therapeutic strategies could potentially benefit the large population of cancer patients affected by hypomorphic *RBX1* expression. Overall, this study establishes *RBX1* as a novel CIN gene, and provides preliminary insight into the early events that may contribute to the development and/or progression of HGSOC and potentially other cancers that are impacted by diminished *RBX1* as well.

CHAPTER 6: REFERENCES

1 Ferlay, J. *et al.* Cancer incidence and mortality worldwide: sources, methods and major patterns in GLOBOCAN 2012. *Int J Cancer* **136**, E359-386, doi:10.1002/ijc.29210 (2015).

2 *International Agency for Research on Cancer. Global Cancer Observatory: Cancer Today. gco.iarc https://gco.iarc.fr/today* (2018).

3 Bray, F. *et al.* Global cancer statistics 2018: GLOBOCAN estimates of incidence and mortality worldwide for 36 cancers in 185 countries. *CA: A Cancer Journal for Clinicians* **68**, 394-424, doi:10.3322/caac.21492 (2018).

4 *Canadian Cancer Statistics Advisory Committee. Canadian Cancer Statistics 2019. Toronto, ON: Canadian Cancer Society*, <https://www.cancer.ca:443/en/cancer-information/cancer-101/canadian-cancer-statistics-publication/?region=on> (2019).

5 Xie, L., Semenciw, R. & Mery, L. Cancer incidence in Canada: trends and projections (1983-2032). *Health promotion and chronic disease prevention in Canada : research, policy and practice* **35 Suppl 1**, 2-186 (2015).

6 Bruin, S. C. *et al.* Molecular alterations associated with liver metastases development in colorectal cancer patients. *British journal of cancer* **105**, 281-287, doi:10.1038/bjc.2011.184 (2011).

7 Walter, F. M. *et al.* Symptoms and patient factors associated with longer time to diagnosis for colorectal cancer: results from a prospective cohort study. *British journal of cancer* **115**, 533-541, doi:10.1038/bjc.2016.221 (2016).

8 Miyoshi, N. *et al.* Clinicopathological characteristics and prognosis of stage IV colorectal cancer. *Molecular and clinical oncology* **3**, 1093-1098, doi:10.3892/mco.2015.598 (2015).

9 Wingfield, S. A. & Heflin, M. T. Cancer Screening in Older Adults. *Clinics in geriatric medicine* **32**, 17-33, doi:10.1016/j.cger.2015.08.009 (2016).

10 Obuch, J. C. & Ahnen, D. J. Colorectal Cancer: Genetics is Changing Everything. *Gastroenterology clinics of North America* **45**, 459-476, doi:10.1016/j.gtc.2016.04.005 (2016).

11 Gonzalez, E. C., Roetzheim, R. G., Ferrante, J. M. & Campbell, R. Predictors of proximal vs. distal colorectal cancers. *Diseases of the colon and rectum* **44**, 251-258 (2001).

12 Nishihara, R. *et al.* Biomarker correlation network in colorectal carcinoma by tumor anatomic location. *BMC Bioinformatics* **18** (2017).

13 Bufill, J. A. Colorectal cancer: evidence for distinct genetic categories based on proximal or distal tumor location. *Annals of internal medicine* **113**, 779-788, doi:10.7326/0003-4819-113-10-779 (1990).

14 Staarmann, J., Kotb, W. F. & Petersen, I. DNA ploidy and morphology of colon tumors in the adenoma-carcinoma sequence. *Folia histochemica et cytobiologica* **53**, 11-18, doi:10.5603/FHC.a2015.0001 (2015).

15 Vogelstein, B. *et al.* Genetic alterations during colorectal-tumor development. *The New England journal of medicine* **319**, 525-532, doi:10.1056/nejm198809013190901 (1988).

16 Schreuders, E. H. *et al.* Colorectal cancer screening: a global overview of existing programmes. *Gut* **64**, 1637-1649, doi:10.1136/gutjnl-2014-309086 (2015).

17 Song, Y. X. *et al.* Can the tumor deposits be counted as metastatic lymph nodes in the UICC TNM staging system for colorectal cancer? *PloS one* **7**, e34087, doi:10.1371/journal.pone.0034087 (2012).

18 Kolligs, F. T. Diagnostics and Epidemiology of Colorectal Cancer. *Visceral Medicine* **32**, 158-164 (2016).

19 Watanabe, T. *et al.* Japanese Society for Cancer of the Colon and Rectum (JSCCR) Guidelines 2014 for treatment of colorectal cancer. *International Journal of Clinical Oncology* **20**, 207-239 (2015).

20 Ahmed, S., Johnson, K., Ahmed, O. & Iqbal, N. Advances in the management of colorectal cancer: from biology to treatment. *International journal of colorectal disease* **29**, 1031-1042, doi:10.1007/s00384-014-1928-5 (2014).

21 Cremolini, C. *et al.* First-line chemotherapy for mCRC-a review and evidence-based algorithm. *Nat Rev Clin Oncol* **12**, 607-619, doi:10.1038/nrclinonc.2015.129 (2015).

22 Mini, E., Trave, F., Rustum, Y. M. & Bertino, J. R. Enhancement of the antitumor effects of 5-fluorouracil by folinic acid. *Pharmacol Ther* **47**, 1-19, doi:10.1016/0163-7258(90)90042-z (1990).

23 Longley, D. B., Harkin, D. P. & Johnston, P. G. 5-fluorouracil: mechanisms of action and clinical strategies. *Nature reviews. Cancer* **3**, 330-338, doi:10.1038/nrc1074 (2003).

24 Faivre, S., Chan, D., Salinas, R., Woynarowska, B. & Woynarowski, J. M. DNA strand breaks and apoptosis induced by oxaliplatin in cancer cells. *Biochemical pharmacology* **66**, 225-237, doi:10.1016/s0006-2952(03)00260-0 (2003).

25 Gilbert, D. C., Chalmers, A. J. & El-Khamisy, S. F. Topoisomerase I inhibition in colorectal cancer: biomarkers and therapeutic targets. *Br J Cancer* **106**, 18-24, doi:10.1038/bjc.2011.498 (2012).

26 Zheng, Y., Zhou, J. & Tong, Y. Gene signatures of drug resistance predict patient survival in colorectal cancer. *The Pharmacogenomics Journal* **15**, 135-143 (2015).

27 Hammond, W. A., Swaika, A. & Mody, K. Pharmacologic resistance in colorectal cancer: a review. *Therapeutic advances in medical oncology* **8**, 57-84 (2016).

28 Longley, D. B. & Johnston, P. G. Molecular mechanisms of drug resistance. *The Journal of pathology* **205**, 275-292, doi:10.1002/path.1706 (2005).

29 Al-Sukhni, W., Aronson, M. & Gallinger, S. Hereditary colorectal cancer syndromes: familial adenomatous polyposis and lynch syndrome. *The Surgical clinics of North America* **88**, 819-844, vii, doi:10.1016/j.suc.2008.04.012 (2008).

30 Lengauer, C., Kinzler, K. W. & Vogelstein, B. Genetic instability in colorectal cancers. *Nature* **386**, 623-627, doi:10.1038/386623a0 (1997).

31 Sieber, O. M., Heinimann, K. & Tomlinson, I. P. Genomic instability--the engine of tumorigenesis? *Nature reviews. Cancer* **3**, 701-708, doi:10.1038/nrc1170 (2003).

32 Negrini, S., Gorgoulis, V. G. & Halazonetis, T. D. Genomic instability--an evolving hallmark of cancer. *Nature reviews. Molecular cell biology* **11**, 220-228, doi:10.1038/nrm2858 (2010).

33 Ciriello, G. *et al.* Emerging landscape of oncogenic signatures across human cancers. *Nature genetics* **45**, 1127-1133, doi:10.1038/ng.2762 (2013).

34 Hanahan, D. & Weinberg, R. A. Hallmarks of cancer: the next generation. *Cell* **144**, 646-674, doi:10.1016/j.cell.2011.02.013 (2011).

35 Bae, J. M., Kim, J. H. & Kang, G. H. Epigenetic alterations in colorectal cancer: the CpG island methylator phenotype. *Histology and histopathology* **28**, 585-595, doi:10.14670/hh-28.585 (2013).

36 Issa, J. P. CpG island methylator phenotype in cancer. *Nature reviews. Cancer* **4**, 988-993, doi:10.1038/nrc1507 (2004).

37 Gatalica, Z., Vranic, S., Xiu, J., Swensen, J. & Reddy, S. High microsatellite instability (MSI-H) colorectal carcinoma: a brief review of predictive biomarkers in the era of personalized medicine. *Familial cancer* **15**, 405-412, doi:10.1007/s10689-016-9884-6 (2016).

38 Boyer, J. C. *et al.* Microsatellite instability, mismatch repair deficiency, and genetic defects in human cancer cell lines. *Cancer Res* **55**, 6063-6070 (1995).

39 Barber, T. D. *et al.* Chromatid cohesion defects may underlie chromosome instability in human colorectal cancers. *Proc Natl Acad Sci U S A* **105**, 3443-3448, doi:10.1073/pnas.0712384105 (2008).

40 Lengauer C, K. K., Volgestein B. Genetic instabilities in human cancers. *Nature* **396:643** (1998).

41 Loeb, L. A. Mutator phenotype may be required for multistage carcinogenesis. *Cancer Res* **51**, 3075-3079 (1991).

42 Duesberg, P. *et al.* How aneuploidy may cause cancer and genetic instability. *Anticancer Res* **19**, 4887-4906 (1999).

43 Weaver, B., Cleveland DW. Does aneuploidy cause cancer? *Curr Opin Cell Biol* **18:658** (2006).

44 Vaughan, S. *et al.* Rethinking ovarian cancer: recommendations for improving outcomes. *Nature reviews. Cancer* **11**, 719-725, doi:10.1038/nrc3144 (2011).

45 Foley, O. W., Rauh-Hain, J. A. & del Carmen, M. G. Recurrent epithelial ovarian cancer: an update on treatment. *Oncology (Williston Park, N.Y.)* **27**, 288-294, 298 (2013).

46 Katabuchi, H. & Okamura, H. Cell biology of human ovarian surface epithelial cells and ovarian carcinogenesis. *Medical electron microscopy : official journal of the Clinical Electron Microscopy Society of Japan* **36**, 74-86 (2003).

47 Auersperg, N., Wong, A. S., Choi, K. C., Kang, S. K. & Leung, P. C. Ovarian surface epithelium: biology, endocrinology, and pathology. *Endocrine reviews* **22**, 255-288, doi:10.1210/edrv.22.2.0422 (2001).

48 Fathalla, M. F. Incessant ovulation--a factor in ovarian neoplasia? *Lancet (London, England)* **2**, 163, doi:10.1016/s0140-6736(71)92335-x (1971).

49 Ness, R. B. & Cottreau, C. Possible role of ovarian epithelial inflammation in ovarian cancer. *J Natl Cancer Inst* **91**, 1459-1467, doi:10.1093/jnci/91.17.1459 (1999).

50 Robinson, S. C. & Coussens, L. M. Soluble mediators of inflammation during tumor development. *Advances in cancer research* **93**, 159-187, doi:10.1016/s0065-230x(05)93005-4 (2005).

51 King, S. M. *et al.* The impact of ovulation on fallopian tube epithelial cells: evaluating three hypotheses connecting ovulation and serous ovarian cancer. *Endocrine-related cancer* **18**, 627-642, doi:10.1530/erc-11-0107 (2011).

52 Fredrickson, T. N. Ovarian tumors of the hen. *Environmental health perspectives* **73**, 35-51, doi:10.1289/ehp.877335 (1987).

53 Barakat, R. R. *et al.* Absence of premalignant histologic, molecular, or cell biologic alterations in prophylactic oophorectomy specimens from BRCA1 heterozygotes. *Cancer* **89**, 383-390, doi:10.1002/1097-0142(20000715)89:2<383::aid-cncr25>3.0.co;2-t (2000).

54 Casey, M. J. *et al.* Histology of prophylactically removed ovaries from BRCA1 and BRCA2 mutation carriers compared with noncarriers in hereditary breast ovarian cancer syndrome kindreds. *Gynecol Oncol* **78**, 278-287, doi:10.1006/gyno.2000.5861 (2000).

55 Dubeau, L. The cell of origin of ovarian epithelial tumors and the ovarian surface epithelium dogma: does the emperor have no clothes? *Gynecol Oncol* **72**, 437-442, doi:10.1006/gyno.1998.5275 (1999).

56 Przybycin, C. G., Kurman, R. J., Ronnett, B. M., Shih, I.-M. & Vang, R. Are All Pelvic (Nonuterine) Serous Carcinomas of Tubal Origin? *The American journal of surgical pathology* **34**, 1407-1416, doi:10.1097/PAS.0b013e3181ef7b16 (2010).

57 Kurman, R. J. & Shih Ie, M. Molecular pathogenesis and extraovarian origin of epithelial ovarian cancer--shifting the paradigm. *Hum Pathol* **42**, 918-931, doi:10.1016/j.humpath.2011.03.003 (2011).

58 Berek, J. S., Crum, C. & Friedlander, M. Cancer of the ovary, fallopian tube, and peritoneum. *International journal of gynaecology and obstetrics: the official organ of the International Federation of Gynaecology and Obstetrics* **119 Suppl 2**, S118-129, doi:10.1016/s0020-7292(12)60025-3 (2012).

59 Kindelberger, D. W. *et al.* Intraepithelial carcinoma of the fimbria and pelvic serous carcinoma: Evidence for a causal relationship. *The American journal of surgical pathology* **31**, 161-169, doi:10.1097/01.pas.0000213335.40358.47 (2007).

60 Labidi-Galy, S. I. *et al.* High grade serous ovarian carcinomas originate in the fallopian tube. *Nature communications* **8**, 1093, doi:10.1038/s41467-017-00962-1 (2017).

61 Matulonis, U. A. *et al.* Ovarian cancer. *Nature reviews. Disease primers* **2**, 16061, doi:10.1038/nrdp.2016.61 (2016).

62 Narod, S. Can advanced-stage ovarian cancer be cured? *Nat Rev Clin Oncol* **13**, 255-261, doi:10.1038/nrclinonc.2015.224 (2016).

63 Young, R. C. *et al.* Adjuvant therapy in stage I and stage II epithelial ovarian cancer. Results of two prospective randomized trials. *The New England journal of medicine* **322**, 1021-1027, doi:10.1056/nejm199004123221501 (1990).

64 Bell, J. *et al.* Randomized phase III trial of three versus six cycles of adjuvant carboplatin and paclitaxel in early stage epithelial ovarian carcinoma: a Gynecologic Oncology Group study. *Gynecol Oncol* **102**, 432-439, doi:10.1016/j.ygyno.2006.06.013 (2006).

65 Trimbos, J. B. *et al.* Impact of adjuvant chemotherapy and surgical staging in early-stage ovarian carcinoma: European Organisation for Research and Treatment of Cancer-Adjuvant ChemoTherapy in Ovarian Neoplasm trial. *J Natl Cancer Inst* **95**, 113-125 (2003).

66 Goff, B. A. *et al.* Development of an ovarian cancer symptom index: possibilities for earlier detection. *Cancer* **109**, 221-227, doi:10.1002/cncr.22371 (2007).

67 Gilbert, L. *et al.* Assessment of symptomatic women for early diagnosis of ovarian cancer: results from the prospective DOvE pilot project. *The Lancet. Oncology* **13**, 285-291, doi:10.1016/s1470-2045(11)70333-3 (2012).

68 Kurman, R. J., Carcangiu, M. L., Herrington, S. & Young, R. H. *WHO classification of tumours of female reproductive organs*. (IARC, 2014).

69 Mutch, D. G. & Prat, J. 2014 FIGO staging for ovarian, fallopian tube and peritoneal cancer. *Gynecol Oncol* **133**, 401-404, doi:10.1016/j.ygyno.2014.04.013 (2014).

70 Bast, R. C., Jr., Hennessy, B. & Mills, G. B. The biology of ovarian cancer: new opportunities for translation. *Nature reviews. Cancer* **9**, 415-428, doi:10.1038/nrc2644 (2009).

71 Chan, J. K. *et al.* Influence of the gynecologic oncologist on the survival of ovarian cancer patients. *Obstetrics and gynecology* **109**, 1342-1350, doi:10.1097/01.aog.0000265207.27755.28 (2007).

72 Mayer, A. R. *et al.* Ovarian cancer staging: does it require a gynecologic oncologist? *Gynecol Oncol* **47**, 223-227, doi:10.1016/0090-8258(92)90110-5 (1992).

73 Lengyel, E. Ovarian cancer development and metastasis. *Am J Pathol* **177**, 1053-1064, doi:10.2353/ajpath.2010.100105 (2010).

74 Horowitz, N. S. *et al.* Does aggressive surgery improve outcomes? Interaction between preoperative disease burden and complex surgery in patients with advanced-stage ovarian cancer: an analysis of GOG 182. *J Clin Oncol* **33**, 937-943, doi:10.1200/jco.2014.56.3106 (2015).

75 Chang, S. J., Bristow, R. E. & Ryu, H. S. Impact of complete cytoreduction leaving no gross residual disease associated with radical cytoreductive surgical procedures on survival in advanced ovarian cancer. *Annals of surgical oncology* **19**, 4059-4067, doi:10.1245/s10434-012-2446-8 (2012).

76 Chang, S. J., Hodeib, M., Chang, J. & Bristow, R. E. Survival impact of complete cytoreduction to no gross residual disease for advanced-stage ovarian cancer: a meta-analysis. *Gynecol Oncol* **130**, 493-498, doi:10.1016/j.ygyno.2013.05.040 (2013).

77 Sherman-Baust, C. A., Becker, K. G., Wood Iii, W. H., Zhang, Y. & Morin, P. J. Gene expression and pathway analysis of ovarian cancer cells selected for resistance to cisplatin, paclitaxel, or doxorubicin. *Journal of ovarian research* **4**, 21, doi:10.1186/1757-2215-4-21 (2011).

78 Sliesoraitis, S. & Chikhale, P. J. Carboplatin hypersensitivity. *International Journal of Gynecologic Cancer* **15**, 13-18, doi:10.1136/ijgc-00009577-200501000-00003 (2005).

79 Fan, W. Possible mechanisms of paclitaxel-induced apoptosis. *Biochemical pharmacology* **57**, 1215-1221, doi:10.1016/s0006-2952(99)00006-4 (1999).

80 Perren, T. J. *et al.* A phase 3 trial of bevacizumab in ovarian cancer. *The New England journal of medicine* **365**, 2484-2496, doi:10.1056/NEJMoa1103799 (2011).

81 Burger, R. A. *et al.* Incorporation of bevacizumab in the primary treatment of ovarian cancer. *The New England journal of medicine* **365**, 2473-2483, doi:10.1056/NEJMoa1104390 (2011).

82 Tewari, K. S. *et al.* Final Overall Survival of a Randomized Trial of Bevacizumab for Primary Treatment of Ovarian Cancer. *Journal of Clinical Oncology* **37**, 2317-2328, doi:10.1200/jco.19.01009 (2019).

83 Integrated genomic analyses of ovarian carcinoma. *Nature* **474**, 609-615, doi:10.1038/nature10166 (2011).

84 Testa, U., Petrucci, E., Pasquini, L., Castelli, G. & Pelosi, E. Ovarian Cancers: Genetic Abnormalities, Tumor Heterogeneity and Progression, Clonal Evolution and Cancer Stem Cells. *Medicines (Basel, Switzerland)* **5**, doi:10.3390/medicines5010016 (2018).

85 Zhang, Y., Cao, L., Nguyen, D. & Lu, H. TP53 mutations in epithelial ovarian cancer. *Translational cancer research* **5**, 650-663, doi:10.21037/tcr.2016.08.40 (2016).

86 Turner, N. C. & Reis-Filho, J. S. Basal-like breast cancer and the BRCA1 phenotype. *Oncogene* **25**, 5846-5853, doi:10.1038/sj.onc.1209876 (2006).

87 Ahmed, A. A. *et al.* Driver mutations in TP53 are ubiquitous in high grade serous carcinoma of the ovary. *The Journal of pathology* **221**, 49-56, doi:10.1002/path.2696 (2010).

88 Medeiros, F. *et al.* The tubal fimbria is a preferred site for early adenocarcinoma in women with familial ovarian cancer syndrome. *The American journal of surgical pathology* **30**, 230-236, doi:10.1097/01.pas.0000180854.28831.77 (2006).

89 Risch, H. A. *et al.* Population BRCA1 and BRCA2 mutation frequencies and cancer penetrances: a kin-cohort study in Ontario, Canada. *J Natl Cancer Inst* **98**, 1694-1706, doi:10.1093/jnci/djj465 (2006).

90 Struewing, J. P. *et al.* The risk of cancer associated with specific mutations of BRCA1 and BRCA2 among Ashkenazi Jews. *The New England journal of medicine* **336**, 1401-1408, doi:10.1056/nejm199705153362001 (1997).

91 Chetrit, A. *et al.* Effect of BRCA1/2 mutations on long-term survival of patients with invasive ovarian cancer: the national Israeli study of ovarian cancer. *J Clin Oncol* **26**, 20-25, doi:10.1200/jco.2007.11.6905 (2008).

92 Chen, F. *et al.* Serous tubal intraepithelial carcinomas associated with high-grade serous ovarian carcinomas: a systematic review. *BJOG: An International Journal of Obstetrics & Gynaecology* **124**, 872-878 (2017).

93 Penner-Goeke, S. *et al.* The temporal dynamics of chromosome instability in ovarian cancer cell lines and primary patient samples. *PLoS Genet* **13**, e1006707, doi:10.1371/journal.pgen.1006707 (2017).

94 Karst, A. M. *et al.* Cyclin E1 deregulation occurs early in secretory cell transformation to promote formation of fallopian tube-derived high-grade serous ovarian cancers. *Cancer research* **74**, 1141-1152, doi:10.1158/0008-5472.can-13-2247 (2014).

95 Charles H. Spruck, K.-A. W. S. I. R. Deregulated cyclin E induces chromosome instability. *Nature* (1999).

96 Dulic, V., Lees, E. & Reed, S. I. Association of human cyclin E with a periodic G1-S phase protein kinase. *Science* **257**, 1958-1961 (1992).

97 Siu, K. T., Rosner, M. R. & Minella, A. C. An integrated view of cyclin E function and regulation. *Cell Cycle* **11**, 57-64, doi:10.4161/cc.11.1.18775 (2012).

98 Nakayama, K. *et al.* Targeted disruption of Skp2 results in accumulation of cyclin E and p27(Kip1), polyploidy and centrosome overduplication. *The EMBO journal* **19**, 2069-2081, doi:10.1093/emboj/19.9.2069 (2000).

99 Kuhn, E. *et al.* CCNE1 amplification and centrosome number abnormality in serous tubal intraepithelial carcinoma: further evidence supporting its role as a precursor of ovarian high-grade serous carcinoma. *Modern pathology : an official journal of the United States and Canadian Academy of Pathology, Inc* **29**, 1254-1261, doi:10.1038/modpathol.2016.101 (2016).

100 Ekholm-Reed, S. *et al.* Deregulation of cyclin E in human cells interferes with prereplication complex assembly. *The Journal of cell biology* **165**, 789-800, doi:10.1083/jcb.200404092 (2004).

101 Shaye, A. *et al.* Cyclin E deregulation is an early event in the development of breast cancer. *Breast cancer research and treatment* **115**, 651-659, doi:10.1007/s10549-008-0266-0 (2009).

102 Dosaka-Akita, H. *et al.* A risk-stratification model of non-small cell lung cancers using cyclin E, Ki-67, and ras p21: different roles of G1 cyclins in cell proliferation and prognosis. *Cancer Res* **61**, 2500-2504 (2001).

103 Etemadmoghadam, D. *et al.* Integrated genome-wide DNA copy number and expression analysis identifies distinct mechanisms of primary chemoresistance in ovarian carcinomas. *Clin Cancer Res* **15**, 1417-1427, doi:10.1158/1078-0432.ccr-08-1564 (2009).

104 Nakayama, N. *et al.* Gene amplification CCNE1 is related to poor survival and potential therapeutic target in ovarian cancer. *Cancer* **116**, 2621-2634, doi:10.1002/cncr.24987 (2010).

105 Nakayama, K. *et al.* CCNE1 amplification is associated with aggressive potential in endometrioid endometrial carcinomas. *International journal of oncology* **48**, 506-516, doi:10.3892/ijo.2015.3268 (2016).

106 Burrell, R. A. *et al.* Replication stress links structural and numerical cancer chromosomal instability. *Nature* **494**, 492-496, doi:10.1038/nature11935 (2013).

107 Lepage, C. C., Morden, C. R., Palmer, M. C. L., Nachtigal, M. W. & McManus, K. J. Detecting Chromosome Instability in Cancer: Approaches to Resolve Cell-to-Cell Heterogeneity. *Cancers* **11**, doi:10.3390/cancers11020226 (2019).

108 Thompson, S. L., Bakhoum, S. F. & Compton, D. A. Mechanisms of chromosomal instability. *Curr Biol* **20**, R285-295, doi:10.1016/j.cub.2010.01.034 (2010).

109 Bakhoum, S. F. & Compton, D. A. Chromosomal instability and cancer: a complex relationship with therapeutic potential. *J Clin Invest* **122**, 1138-1143, doi:10.1172/jci59954 (2012).

110 D'Angiolella, V. *et al.* SCF(Cyclin F) controls centrosome homeostasis and mitotic fidelity through CP110 degradation. *Nature* **466**, 138-142, doi:10.1038/nature09140 (2010).

111 Gstaiger, M., Marti, A. & Krek, W. Association of human SCF(SKP2) subunit p19(SKP1) with interphase centrosomes and mitotic spindle poles. *Exp Cell Res* **247**, 554-562, doi:10.1006/excr.1999.4386 (1999).

112 Hussain, M. *et al.* Skp1: Implications in cancer and SCF-oriented anti-cancer drug discovery. *Pharmacological research* **111**, 34-42, doi:10.1016/j.phrs.2016.05.027 (2016).

113 Sajesh, B. V., Lichtensztejn, Z. & McManus, K. J. Sister chromatid cohesion defects are associated with chromosome instability in Hodgkin lymphoma cells. *BMC cancer* **13**, 391, doi:10.1186/1471-2407-13-391 (2013).

114 Rosario, C. O. *et al.* Plk4 is required for cytokinesis and maintenance of chromosomal stability. *Proc Natl Acad Sci U S A* **107**, 6888-6893, doi:10.1073/pnas.0910941107 (2010).

115 Kondo, T. *et al.* Rapid degradation of Cdt1 upon UV-induced DNA damage is mediated by SCFSkp2 complex. *The Journal of biological chemistry* **279**, 27315-27319, doi:10.1074/jbc.M314023200 (2004).

116 Busino, L. *et al.* Degradation of Cdc25A by beta-TrCP during S phase and in response to DNA damage. *Nature* **426**, 87-91, doi:10.1038/nature02082 (2003).

117 Kaufmann, W. K. *et al.* Mechanisms of chromosomal instability in melanoma. *Environmental and molecular mutagenesis* **55**, 457-471, doi:10.1002/em.21859 (2014).

118 Geigl, J. B., Obenauf, A. C., Schwarzbraun, T. & Speicher, M. R. Defining 'chromosomal instability'. *Trends Genet* **24**, 64-69, doi:10.1016/j.tig.2007.11.006 (2008).

119 Caldon, C. E. *et al.* Cyclin E2 induces genomic instability by mechanisms distinct from cyclin E1. *Cell Cycle* **12**, 606-617, doi:10.4161/cc.23512 (2013).

120 Orr, B. & Compton, D. A. A double-edged sword: how oncogenes and tumor suppressor genes can contribute to chromosomal instability. *Front Oncol* **3**, 164, doi:10.3389/fonc.2013.00164 (2013).

121 Burrell, R. A. & Swanton, C. Tumour heterogeneity and the evolution of polyclonal drug resistance. *Molecular oncology* **8**, 1095-1111, doi:10.1016/j.molonc.2014.06.005 (2014).

122 Al Habyan, S., Kalos, C., Szymborski, J. & McCaffrey, L. Multicellular detachment generates metastatic spheroids during intra-abdominal dissemination in epithelial ovarian cancer. *Oncogene* **37**, 5127-5135, doi:10.1038/s41388-018-0317-x (2018).

123 Hart, I. R. New evidence for tumour embolism as a mode of metastasis. *The Journal of pathology* **219**, 275-276, doi:10.1002/path.2616 (2009).

124 Schwarz, R. F. *et al.* Spatial and temporal heterogeneity in high-grade serous ovarian cancer: a phylogenetic analysis. *PLoS medicine* **12**, e1001789 (2015).

125 Lee, A. J. *et al.* Chromosomal instability confers intrinsic multidrug resistance. *Cancer Res* **71**, 1858-1870, doi:10.1158/0008-5472.can-10-3604 (2011).

126 McClelland, S. E., Burrell, R. A. & Swanton, C. Chromosomal instability: a composite phenotype that influences sensitivity to chemotherapy. *Cell Cycle* **8**, 3262-3266, doi:10.4161/cc.8.20.9690 (2009).

127 Heilig, C. E. *et al.* Chromosomal instability correlates with poor outcome in patients with myelodysplastic syndromes irrespectively of the cytogenetic risk group. *Journal of cellular and molecular medicine* **14**, 895-902, doi:10.1111/j.1582-4934.2009.00905.x (2010).

128 Thompson, L. L. & McManus, K. J. A novel multiplexed, image-based approach to detect phenotypes that underlie chromosome instability in human cells. *PLoS One* **10**, e0123200, doi:10.1371/journal.pone.0123200 (2015).

129 Bhatia, A. & Kumar, Y. Cancer cell micronucleus: an update on clinical and diagnostic applications. *APMIS : acta pathologica, microbiologica, et immunologica Scandinavica* **121**, 569-581, doi:10.1111/apm.12033 (2013).

130 Fenech, M. Cytokinesis-block micronucleus cytome assay. *Nature protocols* **2**, 1084-1104, doi:10.1038/nprot.2007.77 (2007).

131 Thomas, H. J. Genetic instability in colorectal cancer. *Gut* **43**, 450-451, doi:10.1136/gut.43.4.450 (1998).

132 Soucy, T. A. *et al.* An inhibitor of NEDD8-activating enzyme as a new approach to treat cancer. *Nature* **458**, 732-736, doi:10.1038/nature07884 (2009).

133 Jin, J. *et al.* Systematic analysis and nomenclature of mammalian F-box proteins. *Genes & development* **18**, 2573-2580 (2004).

134 Skaar, J. R., D'Angiolella, V., Pagan, J. K. & Pagano, M. SnapShot: F Box Proteins II. *Cell* **137**, 1358, 1358.e1351, doi:10.1016/j.cell.2009.05.040 (2009).

135 Chandra Dantu, S., Nathubhai Kachariya, N. & Kumar, A. Molecular dynamics simulations elucidate the mode of protein recognition by Skp1 and the F-box domain in the SCF complex. *Proteins* **84**, 159-171, doi:10.1002/prot.24963 (2016).

136 Wu, K. *et al.* The SCFHOS/β-TRCP-ROC1 E3 ubiquitin ligase utilizes two distinct domains within CUL1 for substrate targeting and ubiquitin ligation. *Molecular and cellular biology* **20**, 1382-1393 (2000).

137 Nakayama, K. I. & Nakayama, K. Regulation of the cell cycle by SCF-type ubiquitin ligases. *Semin Cell Dev Biol* **16**, 323-333, doi:10.1016/j.semcdb.2005.02.010 (2005).

138 Nakayama, K. I. & Nakayama, K. Ubiquitin ligases: cell-cycle control and cancer. *Nature reviews. Cancer* **6**, 369-381, doi:10.1038/nrc1881 (2006).

139 Petroski, M. D. & Deshaies, R. J. Function and regulation of cullin-RING ubiquitin ligases. *Nature reviews. Molecular cell biology* **6**, 9-20, doi:10.1038/nrm1547 (2005).

140 Deshaies, R. J. & Joazeiro, C. A. RING domain E3 ubiquitin ligases. *Annu Rev Biochem* **78**, 399-434, doi:10.1146/annurev.biochem.78.101807.093809 (2009).

141 Jia, L. & Sun, Y. RBX1/ROC1-SCF E3 ubiquitin ligase is required for mouse embryogenesis and cancer cell survival. *Cell division* **4**, 16, doi:10.1186/1747-1028-4-16 (2009).

142 Cunha-Ferreira, I. *et al.* Regulation of autophosphorylation controls PLK4 self-destruction and centriole number. *Current biology : CB* **23**, 2245-2254, doi:10.1016/j.cub.2013.09.037 (2013).

143 Walter, D. *et al.* SCF(Cyclin F)-dependent degradation of CDC6 suppresses DNA re-replication. *Nature communications* **7**, 10530, doi:10.1038/ncomms10530 (2016).

144 Sun, Y., Tan, M., Duan, H. & Swaroop, M. SAG/ROC/Rbx/Hrt, a zinc RING finger gene family: molecular cloning, biochemical properties, and biological functions. *Antioxidants & redox signaling* **3**, 635-650, doi:10.1089/15230860152542989 (2001).

145 Tan, M., Davis, S. W., Saunders, T. L., Zhu, Y. & Sun, Y. RBX1/ROC1 disruption results in early embryonic lethality due to proliferation failure, partially rescued by simultaneous loss of p27. *Proc Natl Acad Sci U S A* **106**, 6203-6208, doi:10.1073/pnas.0812425106 (2009).

146 Ohta, T., Michel, J. J., Schottelius, A. J. & Xiong, Y. ROC1, a homolog of APC11, represents a family of cullin partners with an associated ubiquitin ligase activity. *Molecular cell* **3**, 535-541 (1999).

147 Sasagawa, Y., Urano, T., Kohara, Y., Takahashi, H. & Higashitani, A. Caenorhabditis elegans RBX1 is essential for meiosis, mitotic chromosomal condensation and segregation, and cytokinesis. *Genes to cells : devoted to molecular & cellular mechanisms* **8**, 857-872 (2003).

148 Seol, J. H. *et al.* Cdc53/cullin and the essential Hrt1 RING-H2 subunit of SCF define a ubiquitin ligase module that activates the E2 enzyme Cdc34. *Genes Dev* **13**, 1614-1626, doi:10.1101/gad.13.12.1614 (1999).

149 Duan, H. *et al.* SAG, a novel zinc RING finger protein that protects cells from apoptosis induced by redox agents. *Mol Cell Biol* **19**, 3145-3155, doi:10.1128/mcb.19.4.3145 (1999).

150 Gu, Q., Tan, M. & Sun, Y. SAG/ROC2/Rbx2 is a novel activator protein-1 target that promotes c-Jun degradation and inhibits 12-O-tetradecanoylphorbol-13-acetate–induced neoplastic transformation. *Cancer research* **67**, 3616-3625 (2007).

151 Ohta, T., Michel, J. J. & Xiong, Y. Association with cullin partners protects ROC proteins from proteasome-dependent degradation. *Oncogene* **18**, 6758-6766, doi:10.1038/sj.onc.1203115 (1999).

152 Yang, E. S. & Park, J. W. Regulation of nitric oxide-induced apoptosis by sensitive to apoptosis gene protein. *Free Radic Res* **40**, 279-284, doi:10.1080/10715760500511500 (2006).

153 Lee, S. J. *et al.* Regulation of heat shock-induced apoptosis by sensitive to apoptosis gene protein. *Free Radic Biol Med* **45**, 167-176, doi:10.1016/j.freeradbiomed.2008.03.026 (2008).

154 Tan, M. *et al.* SAG/ROC2/RBX2 is a HIF-1 target gene that promotes HIF-1 alpha ubiquitination and degradation. *Oncogene* **27**, 1404-1411, doi:10.1038/sj.onc.1210780 (2008).

155 Kamura, T. *et al.* VHL-box and SOCS-box domains determine binding specificity for Cul2-Rbx1 and Cul5-Rbx2 modules of ubiquitin ligases. *Genes Dev* **18**, 3055-3065, doi:10.1101/gad.1252404 (2004).

156 Chen, A. *et al.* The conserved RING-H2 finger of ROC1 is required for ubiquitin ligation. *The Journal of biological chemistry* **275**, 15432-15439, doi:10.1074/jbc.M907300199 (2000).

157 Furukawa, M., Ohta, T. & Xiong, Y. Activation of UBC5 ubiquitin-conjugating enzyme by the RING finger of ROC1 and assembly of active ubiquitin ligases by all cullins. *Journal of Biological Chemistry* **277**, 15758-15765 (2002).

158 Furukawa, M., Zhang, Y., McCarville, J., Ohta, T. & Xiong, Y. The CUL1 C-Terminal Sequence and ROC1 Are Required for Efficient Nuclear Accumulation, NEDD8 Modification, and Ubiquitin Ligase Activity of CUL1. *Molecular and Cellular Biology* **20**, 8185-8197, doi:10.1128/mcb.20.21.8185-8197.2000 (2000).

159 Kamura, T., Conrad, M. N., Yan, Q., Conaway, R. C. & Conaway, J. W. The Rbx1 subunit of SCF and VHL E3 ubiquitin ligase activates Rub1 modification of cullins Cdc53 and Cul2. *Genes & development* **13**, 2928-2933, doi:10.1101/gad.13.22.2928 (1999).

160 Lin, X., Finkelstein, S. D. & Silverman, J. F. Loss of Heterozygosity (LOH) at 17p13 and 22q13 are Shared by Breast and Thyroid Carcinomas for Metastasis. *Applied Immunohistochemistry & Molecular Morphology* **27**, e16-e19, doi:10.1097/pai.0000000000000630 (2019).

161 Comprehensive molecular characterization of human colon and rectal cancer. *Nature* **487**, 330-337, doi:10.1038/nature11252 (2012).

162 Comprehensive molecular profiling of lung adenocarcinoma. *Nature* **511**, 543-550, doi:10.1038/nature13385 (2014).

163 Comprehensive molecular portraits of human breast tumours. *Nature* **490**, 61-70, doi:10.1038/nature11412 (2012).

164 The Molecular Taxonomy of Primary Prostate Cancer. *Cell* **163**, 1011-1025, doi:10.1016/j.cell.2015.10.025 (2015).

165 Gao, J. *et al.* Integrative analysis of complex cancer genomics and clinical profiles using the cBioPortal. *Science signaling* **6**, pl1, doi:10.1126/scisignal.2004088 (2013).

166 Hoadley, K. A. *et al.* Cell-of-Origin Patterns Dominate the Molecular Classification of 10,000 Tumors from 33 Types of Cancer. *Cell* **173**, 291-304.e296, doi:10.1016/j.cell.2018.03.022 (2018).

167 AmericanCancer. *American Cancer Society | Cancer Facts & Statistics*, <http://cancerstatisticscenter.cancer.org/> (2019).

168 Integrated genomic characterization of oesophageal carcinoma. *Nature* **541**, 169-175, doi:10.1038/nature20805 (2017).

169 Chapman, J. R., Taylor, Martin R. G. & Boulton, Simon J. Playing the End Game: DNA Double-Strand Break Repair Pathway Choice. *Molecular cell* **47**, 497-510, doi:10.1016/j.molcel.2012.07.029 (2012).

170 Orthwein, A. *et al.* A mechanism for the suppression of homologous recombination in G1 cells. *Nature* **528**, 422 (2015).

171 Sy, S. M., Huen, M. S. & Chen, J. PALB2 is an integral component of the BRCA complex required for homologous recombination repair. *Proc Natl Acad Sci U S A* **106**, 7155-7160, doi:10.1073/pnas.0811159106 (2009).

172 Zhang, F. *et al.* PALB2 links BRCA1 and BRCA2 in the DNA-damage response. *Current biology : CB* **19**, 524-529, doi:10.1016/j.cub.2009.02.018 (2009).

173 Zhang, F., Bick, G., Park, J. Y. & Andreassen, P. R. MDC1 and RNF8 function in a pathway that directs BRCA1-dependent localization of PALB2 required for homologous recombination. *J Cell Sci* **125**, 6049-6057, doi:10.1242/jcs.111872 (2012).

174 Scrima, A. *et al.* Detecting UV-lesions in the genome: The modular CRL4 ubiquitin ligase does it best! *FEBS letters* **585**, 2818-2825, doi:10.1016/j.febslet.2011.04.064 (2011).

175 Li, J. M. & Jin, J. CRL Ubiquitin Ligases and DNA Damage Response. *Front Oncol* **2**, 29, doi:10.3389/fonc.2012.00029 (2012).

176 Sajesh, B. V., Bailey, M., Lichtensztejn, Z., Hieter, P. & McManus, K. J. Synthetic lethal targeting of superoxide dismutase 1 selectively kills RAD54B-deficient colorectal cancer cells. *Genetics* **195**, 757-767, doi:10.1534/genetics.113.156836 (2013).

177 *Accessory: Gen5 Spot Counting Module*, <https://www.biotek.com/products/accessories/gen5-spot-counting-module/> (2019).

178 Mullany, L. K. *et al.* Specific TP53 Mutants Overrepresented in Ovarian Cancer Impact CNV, TP53 Activity, Responses to Nutlin-3a, and Cell Survival. *Neoplasia (New York, N.Y.)* **17**, 789-803, doi:10.1016/j.neo.2015.10.003 (2015).

179 Bowen, N. J. *et al.* Emerging roles for PAX8 in ovarian cancer and endosalpingeal development. *Gynecol Oncol* **104**, 331-337, doi:10.1016/j.ygyno.2006.08.052 (2007).

180 Ahmed, D. *et al.* Epigenetic and genetic features of 24 colon cancer cell lines. *Oncogenesis* **2**, e71-e71, doi:10.1038/oncsis.2013.35 (2013).

181 Sharma, G. G. *et al.* hTERT associates with human telomeres and enhances genomic stability and DNA repair. *Oncogene* **22**, 131-146, doi:10.1038/sj.onc.1206063 (2003).

182 Hall, L. L., Th'ng, J. P., Guo, X. W., Teplitz, R. L. & Bradbury, E. M. A brief staurosporine treatment of mitotic cells triggers premature exit from mitosis and polyploid cell formation. *Cancer Res* **56**, 3551-3559 (1996).

183 Nicholson, J. M. & Cimini, D. Cancer karyotypes: survival of the fittest. *Frontiers in oncology* **3**, 148-148, doi:10.3389/fonc.2013.00148 (2013).

184 Nowell, P. C. The clonal evolution of tumor cell populations. *Science* **194**, 23, doi:10.1126/science.959840 (1976).

185 Olaharski, A. J. *et al.* Tetraploidy and chromosomal instability are early events during cervical carcinogenesis. *Carcinogenesis* **27**, 337-343, doi:10.1093/carcin/bgi218 (2006).

186 Galipeau, P. C. *et al.* 17p (p53) allelic losses, 4N (G2/tetraploid) populations, and progression to aneuploidy in Barrett's esophagus. *Proc Natl Acad Sci U S A* **93**, 7081-7084, doi:10.1073/pnas.93.14.7081 (1996).

187 Barrett, M. T. *et al.* Molecular phenotype of spontaneously arising 4N (G2-tetraploid) intermediates of neoplastic progression in Barrett's esophagus. *Cancer Res* **63**, 4211-4217 (2003).

188 Fujiwara, T. *et al.* Cytokinesis failure generating tetraploids promotes tumorigenesis in p53-null cells. *Nature* **437**, 1043-1047, doi:10.1038/nature04217 (2005).

189 Cowell, J. K. & Wigley, C. B. Changes in DNA content during in vitro transformation of mouse salivary gland epithelium. *J Natl Cancer Inst* **64**, 1443-1449, doi:10.1093/jnci/64.6.1443 (1980).

190 Guardavaccaro, D. & Pagano, M. Oncogenic aberrations of cullin-dependent ubiquitin ligases. *Oncogene* **23**, 2037-2049, doi:10.1038/sj.onc.1207413 (2004).

191 Lassus, H., Staff, S., Leminen, A., Isola, J. & Butzow, R. Aurora-A overexpression and aneuploidy predict poor outcome in serous ovarian carcinoma. *Gynecologic Oncology* **120**, 11-17, doi:https://doi.org/10.1016/j.ygyno.2010.09.003 (2011).

192 Lassmann, S. *et al.* Predictive value of Aurora-A/STK15 expression for late stage epithelial ovarian cancer patients treated by adjuvant chemotherapy. *Clin Cancer Res* **13**, 4083-4091, doi:10.1158/1078-0432.ccr-06-2775 (2007).

193 Do, T. V. *et al.* Aurora kinase A mediates epithelial ovarian cancer cell migration and adhesion. *Oncogene* **33**, 539-549, doi:10.1038/onc.2012.632 (2014).

194 Marumoto, T., Zhang, D. & Saya, H. Aurora-A — A guardian of poles. *Nature Reviews Cancer* **5**, 42-50, doi:10.1038/nrc1526 (2005).

195 Moghe, S. *et al.* The CUL3-KLHL18 ligase regulates mitotic entry and ubiquitylates Aurora-A. *Biol Open* **1**, 82-91, doi:10.1242/bio.2011018 (2012).

196 Zhou, L. *et al.* The role of RING box protein 1 in mouse oocyte meiotic maturation. *PLoS One* **8**, e68964, doi:10.1371/journal.pone.0068964 (2013).

197 Niikura, Y. *et al.* CENP-A K124 Ubiquitylation Is Required for CENP-A Deposition at the Centromere. *Developmental cell* **32**, 589-603, doi:10.1016/j.devcel.2015.01.024 (2015).

198 Niikura, Y., Kitagawa, R. & Kitagawa, K. CENP-A Ubiquitylation Contributes to Maintaining the Chromosomal Location of the Centromere. *Molecules (Basel, Switzerland)* **24**, doi:10.3390/molecules24030402 (2019).

199 Amato, A., Schillaci, T., Lentini, L. & Di Leonardo, A. CENPA overexpression promotes genome instability in pRb-depleted human cells. *Molecular cancer* **8**, 119, doi:10.1186/1476-4598-8-119 (2009).

200 Tomonaga, T. *et al.* Overexpression and mistargeting of centromere protein-A in human primary colorectal cancer. *Cancer Res* **63**, 3511-3516 (2003).

201 Gu, X. M. *et al.* Expression and prognostic relevance of centromere protein A in primary osteosarcoma. *Pathology, research and practice* **210**, 228-233, doi:10.1016/j.prp.2013.12.007 (2014).

202 Wu, Q. *et al.* Expression and prognostic significance of centromere protein A in human lung adenocarcinoma. *Lung cancer (Amsterdam, Netherlands)* **77**, 407-414, doi:10.1016/j.lungcan.2012.04.007 (2012).

203 Coussens, L. M. & Werb, Z. Inflammation and cancer. *Nature* **420**, 860-867, doi:10.1038/nature01322 (2002).

204 Hansen, M. T. *et al.* A link between inflammation and metastasis: serum amyloid A1 and A3 induce metastasis, and are targets of metastasis-inducing S100A4. *Oncogene* **34**, 424-435, doi:10.1038/onc.2013.568 (2015).

205 Lisio, M. A., Fu, L., Goyeneche, A., Gao, Z. H. & Telleria, C. High-Grade Serous Ovarian Cancer: Basic Sciences, Clinical and Therapeutic Standpoints. *International journal of molecular sciences* **20**, doi:10.3390/ijms20040952 (2019).

206 Stewart, L. M. *et al.* Risk of high-grade serous ovarian cancer associated with pelvic inflammatory disease, parity and breast cancer. *Cancer Epidemiol* **55**, 110-116, doi:10.1016/j.canep.2018.05.011 (2018).

207 Webb, P. M. & Jordan, S. J. Epidemiology of epithelial ovarian cancer. *Best practice & research. Clinical obstetrics & gynaecology* **41**, 3-14, doi:10.1016/j.bpobgyn.2016.08.006 (2017).

208 Espey, L. L. Ovulation as an inflammatory reaction--a hypothesis. *Biology of reproduction* **22**, 73-106, doi:10.1095/biolreprod22.1.73 (1980).

209 Fortner, R. T. *et al.* Reproductive and hormone-related risk factors for epithelial ovarian cancer by histologic pathways, invasiveness and histologic subtypes: Results from the EPIC cohort. *International journal of cancer* **137**, 1196-1208, doi:10.1002/ijc.29471 (2015).

210 Chiaffarino, F. *et al.* Reproductive and hormonal factors and ovarian cancer. *Ann Oncol* **12**, 337-341, doi:10.1023/a:1011128408146 (2001).

211 Gong, T. T., Wu, Q. J., Vogtmann, E., Lin, B. & Wang, Y. L. Age at menarche and risk of ovarian cancer: a meta-analysis of epidemiological studies. *International journal of cancer* **132**, 2894-2900, doi:10.1002/ijc.27952 (2013).

212 Liu, Y. *et al.* Role of miR-182 in response to oxidative stress in the cell fate of human fallopian tube epithelial cells. *Oncotarget* **6**, 38983-38998, doi:10.18632/oncotarget.5493 (2015).

213 Justus, C. R., Leffler, N., Ruiz-Echevarria, M. & Yang, L. V. In vitro Cell Migration and Invasion Assays. *Journal of Visualized Experiments : JoVE* (2014).

214 Ponti, D. *et al.* Isolation and in vitro propagation of tumorigenic breast cancer cells with stem/progenitor cell properties. *Cancer research* **65**, 5506-5511, doi:10.1158/0008-5472.can-05-0626 (2005).

215 *Canadian Cancer Statistics publication - Canadian Cancer Society*, <http://www.cancer.ca/en/cancer-information/cancer-101/canadian-cancer-statistics-publication/?region=on> (2017).

216 *Learn About Cancer | Cancer Resources | American Cancer Society*, <https://www.cancer.org/cancer.html> (2017).

217 Sajesh, B. V., Guppy, B. J. & McManus, K. J. Synthetic genetic targeting of genome instability in cancer. *Cancers* **5**, 739-761, doi:10.3390/cancers5030739 (2013).

218 Kaelin, W. G., Jr. The concept of synthetic lethality in the context of anticancer therapy. *Nature reviews. Cancer* **5**, 689-698, doi:10.1038/nrc1691 (2005).

219 Kim, G. *et al.* FDA Approval Summary: Olaparib Monotherapy in Patients with Deleterious Germline BRCA-Mutated Advanced Ovarian Cancer Treated with Three or More Lines of Chemotherapy. *Clinical cancer research : an official journal of the American Association for Cancer Research* **21**, 4257-4261, doi:10.1158/1078-0432.ccr-15-0887 (2015).

APPENDIX A: SOLUTIONS

CELL CULTURE

McCoy's 5A Complete Media (10% FBS)

Name	Amount
McCoy's 5A Media (Hyclone)	450.0 mL
FBS (Sigma-Aldrich)	50.0 mL
Total Volume	500.0 mL

1× RPMI-1640 Complete Media (10% FBS + 0.01 mg/mL Insulin)

Name	Amount
RPMI-1640 Media (HyClone)	449.5 mL
FBS (Sigma-Aldrich)	50.0 mL
Insulin (Sigma; 10 mg/mL)	500 μL
Total Volume	500.0 mL

1× DMEM/F12 Media

Name	Amount
DMEM/F12 Powder (Gibco)	12.0 g
$NaHCO_3$	2.4 g
Milli-Q Water	up to 1.0 L
Total Volume	1.0 L

- Titrate to pH 7.0
- Pass through 0.2 μm filter to sterilize
- Store in pre-sterilized bottles at 4°C

Ultroser G Serum Substitute

Name	Amount
Ultroser G Powder (Pall Corp.)	1 vial
UltraPure Distilled Water (Gibco)	20.0 mL
Total Volume	20.0 mL

- Let stand 20 min at RT to dissolve powder; mix by pipetting
- Store at -20°C in 10 mL aliquots

1× DMEM/F12 Complete Media (2% Ultroser G)

Name	Amount
1× DMEM/F12 Cell Culture Media	490.0 mL
USG	10.0 mL
Total Volume	500.0 mL

Cupric Sulfate Pentahydrate

Name	Amount
Cupric Sulfate Pentahydrate	26.0 g
Milli-Q Water	up to 1.0 L
Total Volume	1.0 L

10× Phosphate-Buffered Saline (PBS; Stock Solution)

Name	Amount
NaCl	80.0 g
KCl	2.0 g
Na_2HPO_4	14.4 g
KH_2PO_4	2.4 g
Milli-Q Water	up to 1.0 L
Total Volume	1.0 L

- Titrate to pH 7.4

1× PBS

Name	Amount
10× PBS (Stock Solution)	100.0 mL
Milli-Q Water	900.0 mL
Total Volume	1.0 L

GENE SILENCING

1× siRNA Buffer

Name	Amount
5× siRNA Buffer (Dharmacon)	100.0 μL
RNAse Free Water	400.0 μL
Total Volume	500.0 μL

WESTERN BLOT

Modified Radioimmunoprecipitation Assay (RIPA) Buffer

Name	Amount
50 mM Tris – pH 8.0	5.0 mL
150 mM NaCl	7.5 mL
SDS (0.1% [w/v])	500.0 μL
Sodium Deoxycholate (0.5% [w/v])	0.5 g
NP40 (1% [w/v])	1.0 mL
Milli-Q Water	up to 100 mL
Total Volume	100.0 mL

- Store at 4°C, protected from light

25× Protease Inhibitor

Name	Amount
Protease Inhibitor cOmplete EDTA-free (Roche)	1 tablet
Milli-Q Water	2.0 mL
Total Volume	2.0 mL

- Vortex until dissolved, store at -20°C in 50 μL aliquots

Protein Extraction Buffer

Name	Amount
Modified RIPA Buffer	960.0 μL
25× Protease Inhibitor	40.0 μL
Total Volume	1.0 mL

4× Tris-HCl/SDS, pH 6.8 (0.5M Tris-HCl Containing 0.4% SDS)

Name	Amount
Tris	6.05 g
SDS	2.0 g
Milli-Q Water	up to 100 mL
Total Volume	100.0 mL

- Titrate to pH 6.8 with 1N HCl
- Mix, store at 4°C

6× SDS Sample Loading Buffer

Name	Amount
4× Tris-HCl/SDS	6.5 mL
Glycerol	3.0 mL
SDS	1.0 g
β-mercaptoethanol	600.0 μL
Bromophenol Blue	1.2 mg
Total Volume	~10.0 mL

- Mix, store 0.5 mL aliquots at -20°C; warm to RT before use

10× Running Buffer

Name	Amount
Tris Base	30.0 g
Glycine	144.0 g
SDS	10.0 g
Milli-Q Water	up to 1.0 L
Total Volume	1.0 L

1× Running Buffer

Name	Amount
10× Running Buffer	100.0 mL
Milli-Q Water	900.0 mL
Total Volume	1.0 L

1× Transfer Buffer

Name	Amount
10× Running Buffer	50.0 mL
Methanol	100.0 mL
Milli-Q Water	350.0 mL
Total Volume	500.0 mL

Copper Phthalocyanine 3,4',4'',4'''-tetrasulfonic acid Tetrasodium Salt (CPTS)

Name	Amount
CPTS	50.0 mg
HCl	1.0 mL
Milli-Q Water	up to 1.0 L
Total Volume	1.0 L

10× Tris Buffered Saline (TBS)

Name	Amount
NaCl	80.0 g
KCl	2.0 g
1 M Tris – pH 7.5	250.0 mL
Milli-Q Water	up to 1.0 L
Total Volume	1.0 L

1× TBS-Tween20 (TBST)

Name	Amount
10× TBS	100.0 mL
Tween-20	1.0 mL
Milli-Q Water	up to 1.0 L
Total Volume	1.0 L

5% Non-fat Milk Blocking Solution (w/v)

Name	Amount
Non-fat Milk Powder (Carnation)	5.0 g
TBST	up to 100.0 mL
Total Volume	100.0 mL

FLUORESCENT LABELLING

4% Paraformaldehyde Fixative (w/v)

Name	Amount
Paraformaldehyde (VWR Canlab)	0.4 g
1× PBS	10.0 mL
Total Volume	10.0 mL

- Bring to a slight boil to dissolve paraformaldehyde; cool to RT before use

Hoechst 33342 (1 mg/mL Stock Solution)

Name	Amount
Hoechst 33342 (Thermo Scientific)	10.0 mg
1× PBS	up to 10.0 mL
Total Volume	10.0 mL

- Protect from light and store at -20°C

Hoechst 33342 (300 ng/mL Working Dilution)

Name	Amount
Hoechst 33342 Stock Solution	7.0 μL
1× PBS	up to 25.0 mL
Total Volume	25.0 mL

4',6-Diamidino-2-phenylindole (DAPI; 50 μg/mL Stock Solution)

Name	Amount
DAPI (Sigma-Aldrich; 5 mg/mL)	10.0 μL
1× PBS	990.0 μL
Total Volume	1.0 mL

- Store at 4°C protected from light

DAPI Mounting Media

Name	Amount
DAPI (50 μg/mL Stock Solution)	10.0 μL
Vectashield Mounting Media (Vector Laboratories)	990.0 μL
Total Volume	1.0 mL

- Store at 4°C protected from light

MITOTIC CHROMOSOME SPREADS

Colcemid (100 ng/mL Working Dilution)

Name	Amount
KaryoMAX Colcemid (Gibco; 10 μg/mL)	10.0 μL
Complete Cell Culture Media	990.0 μL
Total Volume	1.0 mL

KCl (1 M Stock Solution)

Name	Amount
KCl	7.5 g
Milli-Q Water	up to 100.0 mL
Total Volume	100.0 mL

KCl (75 mM Working Dilution)

Name	Amount
KCl (1 M Stock Solution)	7.5 mL
Milli-Q Water	92.5 mL
Total Volume	100.0 mL

3:1 Methanol:Acetic Acid (Fixative)

Name	Amount
Methanol	12.0 mL
Acetic Acid	4.0 mL
Total Volume	16.0 mL

CRISPR/CAS9 APPROACH

Carbenicillin (50 mg/mL)

Name	Amount
Carbenicillin (VWR Canlab)	0.5 g
Milli-Q Water	10.0 mL
Total Volume	10.0 mL

- Store at -20°C

Luria-Bertani (LB) Agar Plates + 60 μg/mL Carbenicillin

Name	Amount
Tryptone	5.0 g
Yeast Extract	2.5 g
NaCl	5.0 g
LB Agar	7.5 g
Milli-Q Water	up to 500 mL
Carbenicillin (50 mg/mL)	600 μL
Total Amount	~500 mL or 25 plates

- Combine the first 5 ingredients and pour into bottle(s) for autoclaving
- Autoclave to dissolve agar and sterilize
- While still warm (~40°C), add carbenicillin and mix
- Pour into 10 cm plates (~20 mL/plate); allow agar to cool and solidify
- Store at 4°C

Kanamycin (50 mg/mL)

Name	Amount
Kanamycin Sulfate (Fisher Scientific)	0.5 g
Milli-Q Water	10.0 mL
Total Volume	10.0 mL

- Store at -20°C

LB Agar Plates + 50 μg/mL Kanamycin

Name	Amount
Tryptone	5.0 g
Yeast Extract	2.5 g
NaCl	5.0 g
LB Agar	7.5 g
Milli-Q Water	up to 500 mL
Kanamycin (50 mg/mL)	500 μL
Total Amount	~500 mL or 25 plates

- Combine top 5 ingredients and pour into bottle(s) for autoclaving
- Autoclave to dissolve agar and sterilize
- While still warm (~40°C), add kanamycin and mix
- Pour into 10 cm plates (~20 mL/plate); allow agar to cool and solidify
- Store at 4°C

LB Broth + 60 μg/mL Carbenicillin

Name	Amount
Tryptone	5.0 g
Yeast Extract	2.5 g
NaCl	5.0 g
LB	7.5 g
Milli-Q Water	up to 500 mL
Carbenicillin (50 mg/mL)	600 μL
Total Amount	~500 mL

- Combine the first 5 ingredients
- Autoclave to sterilize
- Allow to cool and add carbenicillin

LB Broth + 50 μg/mL Kanamycin

Name	Amount
Tryptone	5.0 g
Yeast Extract	2.5 g
NaCl	5.0 g
LB	7.5 g
Milli-Q Water	up to 500 mL
Kanamycin (50 mg/mL)	500 μL
Total Amount	~500 mL

- Combine the first 5 ingredients
- Autoclave to sterilize
- Allow to cool and add kanamycin

DMEM High Glucose Media + 10% Tetracycline-Free FBS

Name	Amount
DMEM High Glucose Media (HyClone)	450.0 mL
Tetracycline-Free FBS (Clontech)	50.0 mL
Total Volume	500.0 mL

Sort Buffer

Name	Amount
UltroSer G	200 μL
EDTA (50 mM)	400 μL
1× PBS	up to 10.0 mL
Total Volume	10.0 mL

Propidium Iodide (1 mg/mL Stock Solution)

Name	Amount
Propidium Iodide (Sigma)	1.0 mg
Milli-Q Water	1.0 mL
Total Volume	1.0 mL

- Protect from light and store at -20°C

Sort Buffer + 1 ug/mL Propidium Iodide

Name	Amount
Propidium Iodide (1 mg/mL Stock Solution)	10 μL
UltroSer G	200 μL
EDTA (50 mM)	400 μL
1× PBS	up to 10.0 mL
Total Volume	10.0 mL

RNase A (1 mg/mL)

Name	Amount
RNase A (Sigma)	1.0 mg
Milli-Q Water	1.0 mL
Total Volume	1.0 mL

- Store at -20°C

50× Tris-Acetate-EDTA (TAE) Buffer

Name	Amount
Tris	242.0 g
Acetic Acid	57.1 mL
Disodium EDTA	18.61 g
Milli-Q Water	up to 1.0 L
Total Volume	1.0 L

1× TAE Buffer

Name	Amount
50× TAE Buffer	20.0 mL
Milli-Q Water	980.0 mL
Total Volume	1.0 L

SOFT AGAR COLONY FORMATION ASSAYS

2× DMEM/F12 Media

Name	Amount
DMEM/F12 Powder (Gibco)	12.0 g
Sodium bicarbonate	2.4 g
Milli-Q Water	up to 500.0 mL
Total Volume	500.0 mL

- Titrate to pH 7.4
- Pass through 0.2 μm filter to sterilize
- Store at 4°C

2× DMEM/F12 Complete Media + 4% USG

Name	Amount
2× DMEM/F12 Media	480.0 mL
USG	20.0 mL
Total Volume	500.0 mL

2× McCoy's 5A Media

Name	Amount
McCoy's 5A Powder (Sigma-Aldrich)	11.9 g
Sodium Bicarbonate	2.2 g
Milli-Q Water	up to 500.0 mL
Total Volume	500.0 mL

- Adjust pH to 7.4
- Pass through 0.22 μm filter to sterilize

2× McCoy's 5A Complete Media + 20% FBS

Name	Amount
2× McCoy's 5A Media	40.0 mL
FBS	10.0 mL
Total Volume	50.0 mL

2× RPMI-1640 Media

Name	Amount
RPMI-1640 Powder (Gibco)	10.4 g
Sodium Bicarbonate	2.0 g
Milli-Q Water	up to 500.0 mL
Total Volume	500.0 mL

- Adjust pH to 7.4
- Pass through 0.22 μm filter to sterilize

2× RPMI-1640 Complete Media + 20% FBS + 0.02 mg/mL Insulin

Name	Amount
2× RPMI-1640 Media	39.9 mL
FBS	10.0 mL
Insulin (Sigma; 10 mg/mL)	100 μL
Total Volume	50.0 mL

1.2% Agarose (w/v)

Name	Amount
Agarose (Invitrogen)	1.2 g
Milli-Q Water	100.0 mL
Total Volume	100.0 mL

- Autoclave to dissolve agarose and sterilize
- Warm in microwave prior to use

0.8 % Agarose (w/v)

Name	Amount
Agarose (Invitrogen)	0.8 g
Milli-Q Water	100.0 mL
Total Volume	100.0 mL

- Autoclave to dissolve agarose and sterilize
- Warm in microwave prior to use

0.1% Crystal Violet (w/v) (Stock Solution)

Name	Amount
Crystal Violet (Sigma-Aldrich)	0.1 g
Methanol	10.0 mL
Milli-Q Water	90.0 mL
Total Volume	100.0 mL

- Pass through filter to sterilize

0.005% Crystal Violet (w/v) (Working Dilution)

Name	Amount
0.1% Crystal Violet (Stock Solution)	2.5 mL
Milli-Q Water	47.5 mL
Total Volume	50.0 mL

APPENDIX B: SUPPLEMENTARY TABLES

Table S1. KS Tests Reveal Significant Changes in NA Distributions Following *RBX1* Silencing in HCT116 Cells.

Condition	n[A]	*p*-value[B]	Significance[C]	D-statistic[D]
Untransfected	2,420	< 0.0001	****	0.1826
Non-targeting	2,420	-	-	-
si*RBX1*-2	2,420	< 0.0001	****	0.7549
si*RBX1*-4	2,420	< 0.0001	****	0.4312
si*RBX1*-Pool	2,420	< 0.0001	****	0.4321

[A]Number of nuclei analysed.
[B]*p*-values calculated from two-sample KS tests for the listed condition relative to non-targeting control.
[C]Significance level (****, *p*-value < 0.0001).
[D]D-statistic (maximum deviation between the two distribution curves).

Table S2. KS Tests Reveal Significant Changes in NA Distributions Following *RBX1* Silencing in FT194 Cells.

Condition	n[A]	*p*-value[B]	Significance[C]	D-statistic[D]
Untransfected	1,849	0.0628	ns	0.0433
Non-targeting	1,849	-	-	-
si*RBX1*-2	1,849	< 0.0001	****	0.6274
si*RBX1*-4	1,849	< 0.0001	****	0.4159
si*RBX1*-Pool	1,849	< 0.0001	****	0.5646

[A]Number of nuclei analysed.
[B]*p*-values calculated from two-sample KS tests for the listed condition relative to non-targeting control.
[C]Significance level (ns, not significant; ****, *p*-value < 0.0001).
[D]D-statistic (maximum deviation between the two distribution curves).

Table S3. KS Tests Reveal Significant Changes in NA Distributions Following *RBX1* Silencing in FT246 Cells.

Condition	n[A]	*p*-value[B]	Significance[C]	D-statistic[D]
Untransfected	547	0.0713	ns	0.0433
Non-targeting	547	-	-	-
si*RBX1*-2	547	< 0.0001	****	0.3967
si*RBX1*-4	547	< 0.0001	****	0.2176
si*RBX1*-Pool	547	< 0.0001	****	0.3821

[A]Number of nuclei analysed.
[B]*p*-values calculated from two-sample KS tests for the listed condition relative to non-targeting control.
[C]Significance level (ns, not significant; ****, *p*-value < 0.0001).
[D]D-statistic (maximum deviation between the two distribution curves).

Table S4. Mann-Whitney Tests Reveal Significant Increases in MNF Following *RBX1* Silencing in HCT116 Cells.

Condition	n[A]	*p*-value[B]	Significance[C]
Untransfected	6	0.9221	ns
Non-targeting	6	-	-
si*RBX1*-2	6	0.0043	**
si*RBX1*-4	6	0.0260	*
si*RBX1*-Pool	6	0.0152	*

[A]Number of wells analysed.
[B]*p*-values calculated from two-sample Mann-Whitney tests for the listed condition relative to non-targeting control at the corresponding timepoint.
[C]Significance level (ns, not significant; *, p-value < 0.05; **, p-value < 0.01).

Table S5. Mann-Whitney Tests Reveal Significant Increases in MNF Following *RBX1* Silencing in FT194 Cells.

Condition	n[A]	*p*-value[B]	Significance[C]
Untransfected	6	0.0649	ns
Non-targeting	6	-	-
si*RBX1*-2	6	0.0022	**
si*RBX1*-4	6	0.0043	**
si*RBX1*-Pool	6	0.0043	**

[A]Number of wells analysed.
[B]*p*-values calculated from two-sample Mann-Whitney tests for the listed condition relative to non-targeting control at the corresponding timepoint.
[C]Significance level (ns, not significant; *, p-value < 0.05; **, p-value < 0.01).

Table S6. Mann-Whitney Tests Reveal Significant Increases in MNF Following *RBX1* Silencing in FT246 Cells.

Condition	n[A]	*p*-value[B]	Significance[C]
Untransfected	6	0.0649	ns
Non-targeting	6	-	-
si*RBX1*-2	6	0.0043	**
si*RBX1*-4	6	0.0043	**
si*RBX1*-Pool	6	0.0022	**

[A]Number of wells analysed.
[B]*p*-values calculated from two-sample Mann-Whitney tests for the listed condition relative to non-targeting control at the corresponding timepoint.
[C]Significance level (ns, not significant; **, *p*-value < 0.01).

Table S7. KS Tests Reveal Significant Changes in Chromosome Number Distributions Following *RBX1* Silencing in HCT116 Cells.

Condition	n[A]	*p*-value[B]	Significance[C]	D-statistic[D]
Untransfected	100	>0.9999	ns	0.0400
Non-targeting	100	-	-	-
si*RBX1*-2	100	< 0.0001	****	0.7100
si*RBX1*-4	100	< 0.0001	****	0.5470
si*RBX1*-Pool	100	< 0.0001	****	0.8021

[A]Number of mitotic spreads analysed.
[B]*p*-values calculated from two-sample KS tests for the listed condition vs. non-targeting control.
[C]Significance level (ns, not significant; ****, *p*-value < 0.0001).
[D]D-statistic (maximum deviation between the two distribution curves).

Table S8. KS Tests Reveal Significant Changes in Chromosome Number Distributions Following *RBX1* Silencing in FT194 Cells.

Condition	n[A]	*p*-value[B]	Significance[C]	D-statistic[D]
Untransfected	100	0.9972	ns	0.0560
Non-targeting	100	-	-	-
si*RBX1*-2	100	< 0.0001	****	0.5149
si*RBX1*-4	100	< 0.0001	****	0.4455
si*RBX1*-Pool	100	< 0.0001	****	0.3305

[A]Number of mitotic spreads analysed.
[B]*p*-values calculated from two-sample KS tests for the listed condition vs. non-targeting control.
[C]Significance level (ns, not significant; ****, *p*-value < 0.0001).
[D]D-statistic (maximum deviation between the two distribution curves).

Table S9. KS Tests Reveal Significant Changes in Chromosome Number Distributions Following *RBX1* Silencing in FT246 Cells.

Condition	n[A]	*p*-value[B]	Significance[C]	D-statistic[D]
Untransfected	100	>0.9999	ns	0.0402
Non-targeting	100	-	-	-
si*RBX1*-2	100	< 0.0001	****	0.6314
si*RBX1*-4	100	0.0020	***	0.2977
si*RBX1*-Pool	100	0.0185	*	0.2117

[A]Number of mitotic spreads analysed.
[B]*p*-values calculated from two-sample KS tests for the listed condition vs. non-targeting control.
[C]Significance level (ns, not significant; *, *p*-value < 0.05; ***, *p*-value < 0.001; ****, *p*-value < 0.0001).
[D]D-statistic (maximum deviation between the two distribution curves).

Table S10. Statistical Assessment of NA Distributions within *RBX1*$^{+/-}$ FT246 Cells.

Passage Number	Condition	n[A]	*p*-value[B]	Significance[C]	D-statistic[D]
P0	NTgRNA	2435	-	-	-
	Clone 1	2435	< 0.0001	****	0.0730
	Clone 2	2435	< 0.0001	****	0.1842
P4	NTgRNA	2435	-	-	-
	Clone 1	2435	< 0.0001	****	0.5117
	Clone 2	2435	< 0.0001	****	0.4604
P8	NTgRNA	2435	-	-	-
	Clone 1	2435	< 0.0001	****	0.1824
	Clone 2	2435	< 0.0001	****	0.1443
P12	NTgRNA	2435	-	-	-
	Clone 1	2435	< 0.0001	****	0.4735
	Clone 2	2435	< 0.0001	****	0.3652
P16	NTgRNA	2435	-	-	-
	Clone 1	2435	< 0.0001	****	0.1369
	Clone 2	2435	< 0.0001	****	0.3911
P20	NTgRNA	2435	-	-	-
	Clone 1	2435	< 0.0001	****	0.0775
	Clone 2	2435	< 0.0001	****	0.2819

[A]Number of nuclei analysed.
[B]*p*-values calculated from two-sample KS tests for the listed condition relative to non-targeting control at the corresponding timepoint.
[C]Significance level (****, *p*-value < 0.0001).

Table S11. Statistical Assessment of MNF within *RBX1*$^{+/-}$ FT246 Cells.

Passage Number	Condition	n[A]	*p*-value[B]	Significance[C]
	NTgRNA	10	-	-
P0	Clone 1	10	< 0.0001	****
	Clone 2	10	< 0.0001	****
	NTgRNA	10	-	-
P4	Clone 1	10	< 0.0001	****
	Clone 2	10	< 0.0001	****
	NTgRNA	10	-	-
P8	Clone 1	10	< 0.0001	****
	Clone 2	10	< 0.0001	****
	NTgRNA	10	-	-
P12	Clone 1	10	0.0302	*
	Clone 2	10	< 0.0001	****
	NTgRNA	10	-	-
P16	Clone 1	10	< 0.0001	****
	Clone 2	10	< 0.0001	****
	NTgRNA	10	-	-
P20	Clone 1	10	< 0.0001	****
	Clone 2	10	0.0002	***

[A]Number of wells analysed.
[B]*p*-values calculated from two-sample Mann-Whitney tests for the listed condition relative to non-targeting control at the corresponding timepoint.
[C]Significance level (*, *p*-value < 0.05; ***, *p*-value < 0.001; ****, *p*-value < 0.0001).

Table S12. Statistical Assessment of Chromosome Number Distributions within *RBX1*$^{+/-}$ FT246 Cells.

Passage Number	Condition	n[A]	*p*-value[B]	Significance[C]	D-statistic[D]
	NTgRNA	100	-	-	-
P0	Clone 1	100	< 0.0001	****	0.3909
	Clone 2	100	< 0.0001	****	0.5278
	NTgRNA	100	-	-	-
P4	Clone 1	100	< 0.0001	****	0.6649
	Clone 2	100	< 0.0001	****	0.8010
	NTgRNA	100	-	-	-
P8	Clone 1	100	0.0038	**	0.2461
	Clone 2	100	< 0.0001	****	0.4026
	NTgRNA	100	-	-	-
P12	Clone 1	100	< 0.0001	****	0.4531
	Clone 2	100	< 0.0001	****	0.5743
	NTgRNA	100	-	-	-
P16	Clone 1	100	< 0.0001	****	0.5130
	Clone 2	100	< 0.0001	****	0.7724
	NTgRNA	100	-	-	-
P20	Clone 1	100	< 0.0001	****	0.3795
	Clone 2	100	< 0.0001	****	0.7592

ANumber of mitotic spreads analysed.

[B]*p*-values calculated from two-sample KS tests for the listed condition relative to non-targeting control at the corresponding timepoint.

[C]Significance level (**, *p*-value < 0.01; ****, *p*-value < 0.0001).

[D]D-statistic (maximum deviation between the two distribution curves).